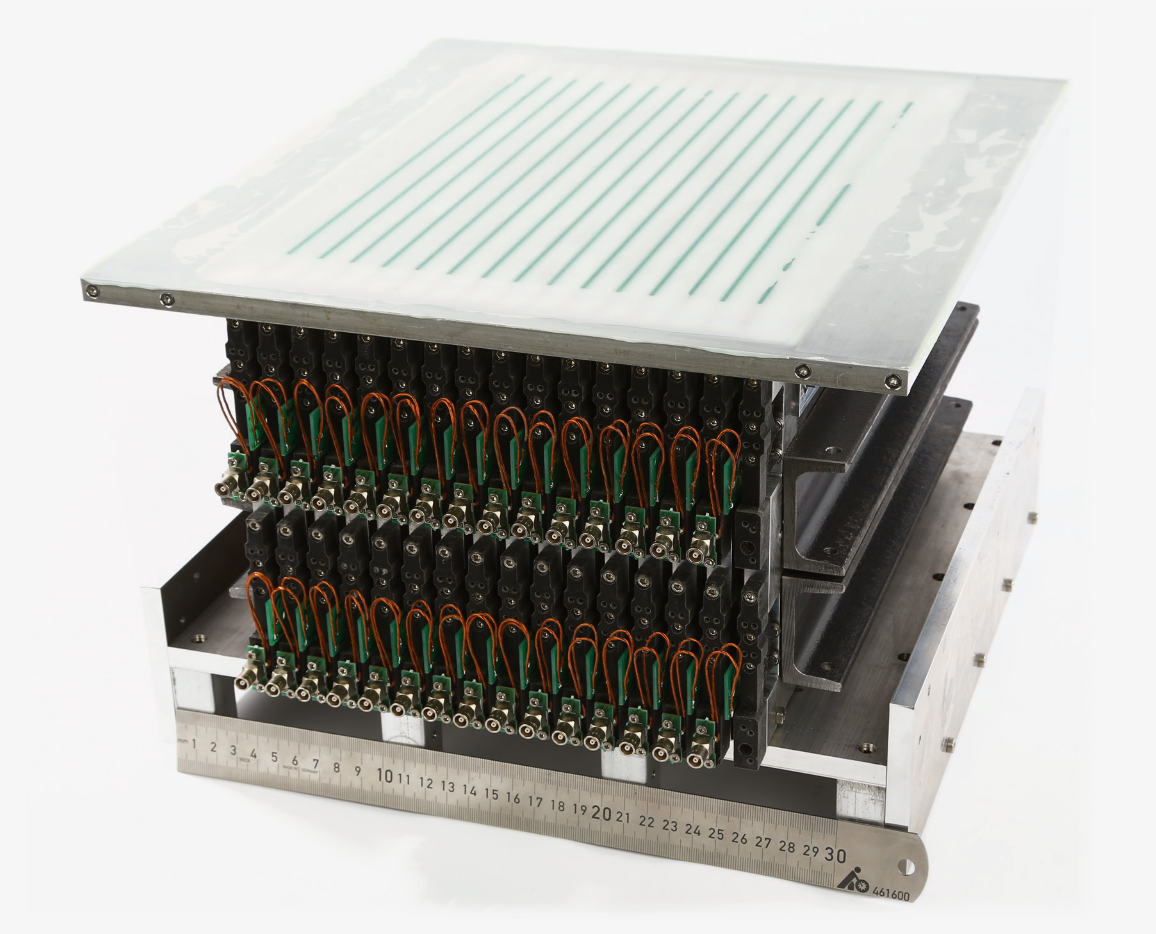

Control and Optimization of a Lorentz Force Based Actuator System for External Flow

Martin Florian Seidler

Energie & Umwelt / Energy & Environment
Band / Volume 524
ISBN 978-3-95806-518-5

JÜLICH Forschungszentrum

Schriften des Forschungszentrums Jülich
Reihe Energie & Umwelt / Energy & Environment Band / Volume 524

Forschungszentrum Jülich GmbH
Zentralinstitut für Engineering, Elektronik und Analytik (ZEA)
Systeme der Elektronik (ZEA-2)

Control and Optimization of a Lorentz Force Based Actuator System for External Flow

Martin Florian Seidler

Schriften des Forschungszentrums Jülich
Reihe Energie & Umwelt / Energy & Environment Band / Volume 524

ISSN 1866-1793 ISBN 978-3-95806-518-5

Bibliografische Information der Deutschen Nationalbibliothek.
Die Deutsche Nationalbibliothek verzeichnet diese Publikation in der Deutschen Nationalbibliografie; detaillierte Bibliografische Daten sind im Internet über http://dnb.d-nb.de abrufbar.

Herausgeber und Vertrieb: Forschungszentrum Jülich GmbH
Zentralbibliothek, Verlag
52425 Jülich
Tel.: +49 2461 61-5368
Fax: +49 2461 61-6103
zb-publikation@fz-juelich.de
www.fz-juelich.de/zb

Umschlaggestaltung: Grafische Medien, Forschungszentrum Jülich GmbH

Druck: Grafische Medien, Forschungszentrum Jülich GmbH

Schriften des Forschungszentrums Jülich
Reihe Energie & Umwelt / Energy & Environment, Band / Volume 524

D 82 (Diss. RWTH Aachen University, 2020)

ISSN 1866-1793
ISBN 978-3-95806-518-5

Vollständig frei verfügbar über das Publikationsportal des Forschungszentrums Jülich (JuSER) unter www.fz-juelich.de/zb/openaccess.

Abstract

The research unit FOR 1779 develops robust methods for the reduction of turbulent friction drag via wavy surface oscillations. For this research, wind tunnel experiments with a Lorentz force actuator system producing traveling surface waves are conducted. An improved version of the system necessitates feedback control that is designed based on iterative learning control and verified in reference tracking and wind tunnel measurements. Due to thermal limits the design does not reach the desired parameters. A new design is optimized with the help of numerical methods and a first prototype reaches the desired parameters.

Kurzzusammenfassung

Die Forschergruppe 1779 entwickelt robuste Methoden zur Reduktion des turbulenten Reibungswiderstandes über wellenförmige Oberflächenoszillationen. Für diese Forschung werden Windkanalmessungen mit einem lorentzkraftbasierten Aktuatorsystem, das laufenden Oberflächenwellen erzeugt, durchgeführt. Eine verbesserte Version des Systems macht eine Regelung notwendig, die auf Basis einer iterativ lernenden Regelung entwickelt und in Führungsfolge- und Windkanalmessungen verifiziert wird. Wegen thermischer Beschränkungen erreicht das Aktuatorsystem nicht die gewünschten Parameter. Eine neue Version wird mithilfe von numerischen Methoden optimiert und ein erster Prototyp erreicht die gewünschten Parameter.

Dedication

To my mother

Acknowledgments

I would like to express my sincere gratitude to my supervisor Univ.-Prof. Dr.-Ing. Dirk Abel for his guidance and support in developing my skills as a control engineer. My gratitude also goes to his colleague and my second supervisor Univ.-Prof. Dr.-Ing. Wolfgang Schröder, who had, as head of FOR 1779, a leading role in providing the framework within which this thesis was prepared. In addition, I would like to thank Univ.-Prof. Dr.-Ing. Stefan van Waasen, head of the ZEA-2, where I spent most of my time working on this thesis, for entrusting me with the project management for this work and supporting me in my decisions.

I am deeply grateful to Dr. Michael Schiek, my team leader and local supervisor at the ZEA-2, for heading the subproject 4 of the FOR 1779, for inspiring my work, strengthening my confidence and helping me to find the best ways to communicate the results of my work. Furthermore, I would like to thank Wolfgang Silex for believing in, advising me on and realizing my ideas on the actuator system with utmost care and patience. Similarly, I am thankful for the design of circuitry necessary for the project by Dipl.-Ing. (FH) Roger Heil. My thanks also go to all colleagues at the ZEA-2, who gave me a friendly, motivating work environment.

I am grateful for Dr.-Ing. Wenfeng Li's instrumental, leading role in wind tunnel measurements and for his advice with regards to their special requirements. Dr.-Ing. Lorenz Pyta and Dr.-Ing. Mathias Hakenberg deserve my sincere gratitude for helping me develop knowledge about theory and practice of control design.

Finally I would like to thank all my friends, who supported me while I was working on the thesis, among whom Amy Van den Bulck lent me her skills as a native speaker of the thesis' language.

Contents

Abbreviations

AIA	Institute of Aerodynamics of RWTH Aachen University
CFD	Computational Fluid Dynamics
CNC	Computer Numerical Control (mills)
CPU	Central Processing Unit
DAQ	Data Acquisition
DE	Differential Equation
DFG	German Research Foundation
DMA	Direct Memory Access
DR	Drag Reduction
DSP	Digital Signal Processing
FEM	Finite Element Method
FIR	Finite Impulse Response (filter)
FPGA	Field Programmable Gate Array
FOR 1779	Forschergruppe (research unit) 1779
GUI	Graphical User Interface
GRP	Glass-fiber Reinforced Plastic
HDD	Hard Disk Drive
IIR	Infinite Impulse Response (filter)
ILC	Iterative Learning Control
LAN	Local Area Network
MIMO	Multiple Input Multiple Output
NRMSE	Normalized Root Mean Square Error
NdFeB	Neodymium Iron Boron (alloy)
op-amp	Operational Amplifier
OS	Operating System
PCB	Printed Circuit Board
PCI	Peripheral Component Interconnect
PD	Proportional Differential (control)
PDE	Partial Differential Equation
PI	Proportional Integral (control)

PIV	Particle Image Velocimetry
PTV	Particle Tracking Velocimetry
SCSI	Small Computer System Interface
SISO	Single Input Single Output
SSD	Solid State Drive
ZEA-2	Central Institute of Engineering, Electronics and Analytics Electronic Systems

1 Introduction

Friction drag is an important economic and ecological issue throughout most of modern transportation systems. Much of the resources for transportation are used up to overcome friction drag. For example it contributes up to 50 % to the total drag in subsonic aircraft [36].

One promising way to address this economic and ecological issue is to reduce friction drag [22]. For this purpose passive and active measures are discussed [17]. Within this field, the research unit FOR 1779, funded by the DFG (German research foundation) [7], studies active drag reduction via wavy surface oscillations. The participating researchers perform numerical simulations [20] as well as wind tunnel experiments [36] [22] [23] to develop robust methods for the reduction of turbulent friction drag.

The wind tunnel experiments require an appropriate actuator system, which can produce surface waves with wave parameters that have been shown in numerical simulations to be promising [27] [26]. Within the first funding period of FOR 1779 a Lorentz force based actuator system with 10 parallel bars at 20 mm distance has been developed, enabling the generation of transversal surface waves with a wavelength of 160 mm and 500 µm amplitude at up to 81 Hz frequency. The wave parameters had to be calibrated manually before the wind tunnel experiments. To enable the generation of waves with shorter length, higher amplitudes at higher frequencies, and to allow for online adaptation of the wave parameters during the experiments an improved 20 bar actuating system featuring smaller bar distances of 10 mm and optical sensors for online monitoring of the actuator bars amplitudes was built. Controlling and improving this actuator system is the topic of this thesis.

The following sections will introduce the work of the research unit FOR 1779 (Section 1.1). The target wave parameters which have to be realized by the controlled actuator system will be discussed in (Section 1.2). Finally an overview of the structure of this thesis is given (Section 1.3).

1.1 Research Unit FOR 1779

Figure 1.1: The logo of the research unit 1779 illustrates transversal surface waves on an airplane wing perpendicular to the airflow influencing the turbulent boundary layer.

The scientific focus of research unit FOR 1779 is technology oriented external flow research to develop robust methods for active drag reduction by transversal surface waves (see Figure 1.1). In contrast to today's approach, aiming to stabilize the laminar state of the boundary layer flow, the new approach followed by FOR 1779 is to only dampen the near-wall coherent structures and, by this manipulation, to decrease the wall shear stress of the turbulent boundary layer efficiently. Besides the reduction of transport energy consumption, this approach will also help to reduce turbulence related traffic noise.

The development is based on numerical studies and wind tunnel experiments. The studies and experiments include the combination of the active transversal waves with the passive approach of a riblet structured surface. In order to match the experimental results with the numerical studies, which are performed for realistic Reynolds numbers, the transversal waves in the wind tunnel have to exactly match the specification.

The first actuator system developed within the framework of FOR 1779 at the Central Institute of Engineering, Electronics and Analytics (ZEA-2) was based on piezo actuators achieving a wave amplitude of 45 µm, which was considered too small to reduce friction drag at given wind tunnel conditions. Therefore a Lorentz force based actuator system was developed (see Chapter 2). The system could generate maximum wave amplitudes of 500 µm at a frequency up to 81 Hz, but did not provide online wave amplitude information. With this system, drag reduction could be realized experimentally with flat and with riblet structured surfaces.

For further experimental studies, larger wave amplitudes at higher frequencies and shorter wavelength were of demand. Additionally, the wave parameters needed to be adapted online to changing inflow conditions induced as part of new wind tunnel experiments. These demands required the development of a new system including sensors for monitoring amplitude and capability for wave control. The results of the new wind tunnel experiments and the ongoing numerical studies will help to develop robust and efficient model based control methods to reduce friction drag.

1.2 System Requirements

Table 1.1: Target wave parameters.

Wave parameter	**Target range**
Frequency in Hz	80 to 135
Amplitude in µm	260 to 1000
Wavelength in mm	80 to 160
Unevenness	$< 10\,\%$
Maximum temporal standard deviation	$< 10\,\%$

The range and accuracy of the wave parameters to be realized by the new, controlled actuator system are listed in Table 1.1. The quality parameters warrant further explanation. One obvious measure is the deviation Δ_A

of the mean wave amplitude $\langle \bar{A} \rangle_k$ from the reference amplitude R. It is defined as:

$$\Delta_A = \frac{|R - \langle \bar{A} \rangle_k|}{R} \qquad \in [0, \infty) \tag{1.1}$$

It should be smaller than 10 %. To refine this general measurement, additional figures of merit are defined to separately evaluate spatial and temporal deviations during wave actuation.

The figure of merit focused on the spatial quality is called unevenness. For evaluation of the average amplitude of the bars m to n, the time averages of the instantaneous amplitudes, designated $\bar{A}_{m\ldots n}$, are determined via the Hilbert transform. Their average with regard to the actuator index $\langle \bar{A}_{m\ldots n} \rangle_k$ is also calculated. The unevenness μ_A in amplitude is defined as:

$$\mu_A = \frac{\max(\bar{A}_{m\ldots n}) - \min(\bar{A}_{m\ldots n})}{2 \cdot \langle \bar{A}_{m\ldots n} \rangle_k} \qquad \in [0, \infty) \tag{1.2}$$

Due to the time averaging and restriction to amplitude this figure of merit is neither impacted by local phase velocity nor wave shape. It is required to be smaller than 10 %.

Another figure of merit focuses on the temporal properties of the wave. Instead of averaging the instantaneous amplitudes, for the kth bar the standard deviation over the time span evaluated $\sigma_t(A_k)$ is determined. Thus, the figure of merit that will be called maximum normalized temporal standard deviation in amplitude is defined as:

$$\hat{\sigma}_{t,A} = \max\left(\frac{\sigma_t(A_{m\ldots n})}{\bar{A}_{m\ldots n}}\right) \qquad \in [0, \infty) \tag{1.3}$$

The standard deviation gives an estimate of the typical deviation from the sine shape and avoids over-emphasizing single over- or undershoots. It is required to be smaller than 10 %.

Figures for the temporal averages of differences between the instantaneous phases of the actuators $\bar{\phi}_{m...n}$ are defined analogously. The figure μ_ϕ is calculated without normalization:

$$\mu_\phi = \max(\bar{\phi}_{m...n}) - \min(\bar{\phi}_{m...n}) \qquad \in [0°, 360°) \tag{1.4}$$

An analog to $\hat{\sigma_{t,A}}$, $\hat{\sigma}_{t,\phi}$, is also added. It is calculated from the differences between the instantaneous phases of the actuators $\phi_{m...n}$:

$$\hat{\sigma}_{t,\phi} = \max(\sigma_{t,\phi}(\phi_{m...n})) \qquad \in [0°, 360°) \tag{1.5}$$

1.3 Thesis Overview

After this introduction six chapters and a conclusion follow, the first of which is Chapter 2. It describes the working principle of the Lorentz force based actuator system and all important components. It also establishes definitions used throughout the remainder of the thesis, of which the axes and system version numbers are most frequently used. The system built in the first funding period and the one for the second funding period, completed just before the work on this thesis began, are described and compared. The chapter closes with a short classification of the system and comparison of another recently build actuator system for similar purposes.

Chapter 3 focuses on the tools used to build, optimize, model and control the actuator system. The Matlab Simulink Real Time software and Speedgoat target computer, which were central for the control design process, are introduced first. They are followed by software tools used by specialists at the ZEA-2 for designing parts for the actuator system and the hardware involved in building the designs. The last part of the chapter covers a range of sensors used for calibration, reference or verification of simulation results.

The following two chapters, Chapter 4 and 5, revolve around models and control design for the actuator system. They are the core of this thesis. Chapter 4 first develops a model from the basic laws of physics governing the system. Due to some simplifications made in its derivation, this model does not predict rotational oscillations, which are instead studied using a numerical method. Based on the results of these studies, a new sensor design is developed and implemented. In addition, various upgrades are made to the system to prepare it for feedback control.

The first part of Chapter 5 focuses on a test system with three actuator bars. On this system a proportional-differential control, tuned based on the previously developed differential equation model, is tested. The results show that a different control method is necessary. For this purpose, iterative learning control is proposed, as it is particularly well suited to inherently periodic tasks like wave control. A description of the basic working principle of iterative learning control and previous research on the topic is followed by the implementation of iterative learning control on the three bar system. The second part of Chapter 5 revolves around the adaptations necessary to apply the control design tested on the three bar system to the full-scale 20 bar system. To this end, feed-forward decoupling at the target frequency is developed and feedback is applied at two timescales, steady state and target frequency using different methods. With this design, the actuator system can be controlled within the target parameter ranges.

The last two chapters before the conclusion, Chapters 6 and 7, are concerned with verification and optimization of the actuator system's capabilities. Chapter 6 contains a verification in two parts. The first part describes test stand results on amplitude, frequency and wavelength, reaching parameter sets within the target range, but not fully covering it. It also applies the quality measures detailed in the previous section. The second part presents measurements with the system taken in a wind tunnel of the Institute of Aerodynamics of RWTH Aachen University (AIA). The setup is described and the results compared to similar measurements taken previously with the older actuator system built during the first funding period.

Chapter 7 further elaborates on optimization of the system. However, unlike in Chapter 4, a completely new system is designed with the help of numerical simulations. These simulations predict the performance impact of design decisions enabling systematic optimization. As a result two prototypes are presented, on which first tests are conducted that show the success of the optimization by reaching the maximum target amplitude and even higher frequencies than required.

This thesis closes with a conclusion and outlook (see Chapter 8), which summarize the results and discuss how control and performance could be further improved in the future.

During the work on this thesis, the thesis work of four students was supervised:

- "Modellbasierte Implementierung klassischer Regelungsstrategien für ein elektromagnetisches Aktuatorsystem in der Turbulenzforschung", completion of the already begun Bachelor thesis of Julius Trabert, Hochschule Fulda
- "COMSOL Finite Element Simulation of an Electromechanical Actuator System for Turbulence Research", Master thesis of Masanam Balakrishnan Bharat Vikas, University of Duisburg-Essen
- "Time-dependent electromagnetic and thermal finite element simulation of an actuator system for turbulence research", Master thesis of Christoph Rausch, Heinrich-Heine University Düsseldorf
- "Time-Independent Finite Element Simulations of Magnetic Behavior in an Actuator System Used for Research Concerned with Active Drag Reduction", Master thesis of Courtney Ford, University of Bonn

2 Lorentz Force Actuator System

The actuator system this thesis is concerned with produces the traveling wave discussed in the introduction (Section 1.2) by periodically bending a roughly $300\,\mathrm{mm} \times 400\,\mathrm{mm}$ large sheet of surface material. For this purpose each actuator moves on a sine trajectory with linearly increasing phase shift along the propagation direction. The topic of this chapter is how the actuator system is constructed to achieve this movement at the frequency, amplitude, wavelength and quality required. First the mechanical construction and then the drive mechanism are laid out. The chapter closes with sections dedicated specifically to individual actuator systems, which are relevant to the following chapters, and a comparison to another type of actuator system for the same purpose. Further developments to improve over the Lorentz force actuator systems described in this chapter can be found in Chapter 7.

2.1 Mechanical Properties

For better orientation when describing the actuator system a standard Cartesian coordinate system is used. The direction of the intended wave propagation, perpendicular to the intended air flow, also called the spanwise direction, is referred to as the x-direction. The direction of the intended air flow, also called the streamwise direction, will be referred to as the y-direction. And finally the direction in which the bars should move, also called the wall normal direction, will be referred to as z-direction or up and down (see Figure 2.1). In addition, shorthands for rotations are used in the following. For rotations in the y-z-plane (i.e. rotational axis parallel to the x-axis) are shortened to y-tilting. Analogously, rotations in the x-z-plane (i.e. rotational axis parallel to the y-axis) are shortened to x-tilting.

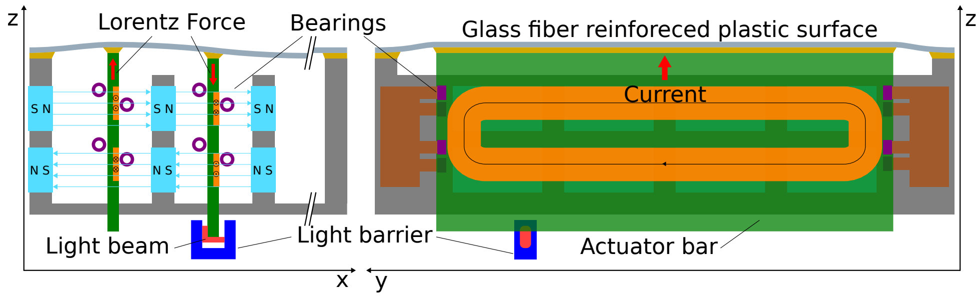

Figure 2.1: Cross-sections of the actuator system. It is cut along x-direction (left), the propagation direction of the wave, and y-direction (right), the direction of the airflow. The z-direction is the direction of the actuator bar movement.

The research for this thesis was conducted with multiple actuator systems. To differentiate them, the system built and used during the first funding period of the project will be called system 1.0. The successor system whose goal was higher spatial resolution will be called system 2.0. Upgrades and further developments (systems 2.1, 3.0 and 3.1) will be covered in Chapter 4 and Chapter 7.

The actuated surface is naturally an important part of the system. It obviously needs to be elastic, so it can be deformed into the surface wave. Since it directly interacts with the flow, its shape is important. For some experiments conducted with the system it has to be smooth. For others it needs to be formed into a riblet structure[22]. Regarding elasticity, an appropriate compromise between generally low effort for elastic deformation and avoiding undesirable fluttering (e.g. in thin cloth [internal communication]) is needed. In addition, the mechanical properties should not quickly degrade under the typical mechanical stresses and environmental conditions in the wind tunnel. Many materials can fit these criteria, for example metal sheets. The obvious choice was aircraft aluminum (thickness 0.3 mm), which is widely used in modern aircraft. It is also easy to machine into riblets, underlining the flexibility in surface choice possible with this system [22].

The surface is glued to a rectangular frame, while the frame is fixed to the body of the actuator system (see Figures 2.3 and 2.4). This measure

Table 2.1: General mechanical, electrical, magnetic and performance properties of the different actuator models. Dimensions given as width × height × thickness.

Parameters for system version	**1.0**	**2.0**
Spacing in mm	20	10
Aluminum surface thickness in mm	0.25	0.3
Dimensions of magnets in mm	50 × 15 × 15	50 × 15 × 5
Magnetic energy product in MGoe	48	48
Coil dimensions in mm	285 × 47 × 1.0	285 × 44 × 1.0
Coil Cu-wire diameter in mm	0.12	0.28
Number of turns	200	80
Coil resistance in Ω	170	14
Coil ampacity in A	0.25	1.25
Bar total mass in g	57	90
Magnetic flux density in T	0.6 to 0.8	0.54
Maximum acceleration in m/s^2	320 to 430	320

is necessary to avoid exposing sharp edges to the airflow which might disturb aerodynamic measurements. The actuator bars are also glued to the surface. They are oriented parallel to each other in y-direction at a fixed spacing (see Table 2.1). While the frame provides a large surface area and, therefore, a mechanically robust connection to the surface, the top of the actuator bars has to be much slimmer (approx. 1 mm) to leave room for the surface material to bend and to keep its mass low (see also Chapter 7). Since sensors are generally placed on or at the actuator bar while the surface displacement should be measured, the connection of the bar to the surface also needs to be as stiff as possible. These requirements and the fact that a certain gap filling capability is also needed led us to use the Loctite 9466 two component glue [14]. Unfortunately even this high performing glue can be overwhelmed by peeling forces appearing at the ends of the actuators due to uneven accelerations there. This area proved the most common point of failure in the systems 1.0 and 2.0 and required regular maintenance.

The stable, resting body of the actuator is made up of a stack of magnet holders. They are thick aluminum sheets (thickness aligns with magnet thickness, see Table 2.1) with receptacles for magnets and various screw threads for mounting other parts of the system (e.g. sensors, signal collector board, surface frame, feet etc.). The permanent magnets are held in place by clamping force and glue. The magnets in turn press the stack together securely fixing the spacers keeping the holders apart.

In order to keep the actuator bars from x-tilting and potentially hitting the walls of the shaft they are operating in, which would cause abrasion, they are guided by bearings. The bearings themselves are linear bearings (Misumi BSGM6-25 [28]) for actuator 1.0 and 2.0. The 3D printed holders of the bearings have to allow for movement in y-direction to avoid jamming issues but keep tight guidance in x-direction.

2.2 Lorentz Force

The primary purpose of the permanent magnets is to provide the magnetic flux necessary for the operation of the actuator bars. For this purpose, very strong neodymium-iron-boron (NdFeB) rare earth permanent magnets are used with an energy product of 48 megagauss oersted (approx. $384\,\mathrm{kJ/m^3}$), commonly written as N48 (Table 2.1). The magnets are placed such that opposing and, therefore, attracting poles face each other resulting in a relatively homogeneous magnetic flux density between them. Inside this magnetic field an elongated rectangular air core coil is placed. It is glued into a milled out groove in a bar of Glass-fiber Reinforced Plastic (GRP) so it takes up as little space as possible and so it sits roughly in the center below the area where force is applied to the surface. This assembly forms the actuator bar (see Figure 2.2). Under the assumption that field and coil wire are perpendicular, the bar experiences a Lorentz force described by the formula:

$$F_L = lnBI \tag{2.1}$$

with B the magnetic flux density, n the number of turns of the coil, I the current and l effective length of coil sections immersed in the magnetic field. The magnets are placed along the long, straight upper and lower portion of the coil. The upper magnets are directed opposite to the lower magnets to ensure the Lorentz force on the lower part of the coil points in the same direction as the one on the upper part (see Figure 2.1). This operating principle provides very linear force-displacement relation as long as the coil does not leave the homogeneous part of the magnetic field. It has an electrical bandwidth limited by the self resonance of the coil in the 100 kHz range and provides high acceleration due to the low mass of the bars.

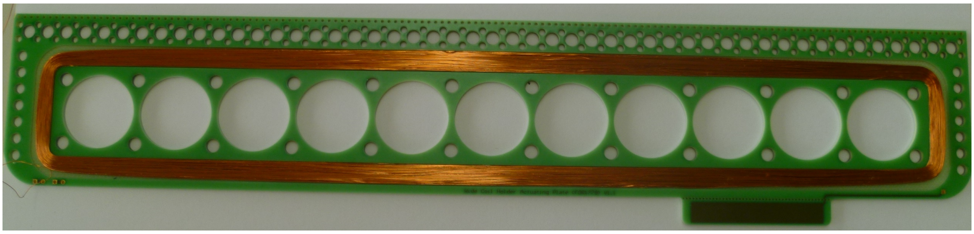

Figure 2.2: A system 1.0 actuator bar with glued coil.

2.3 Actuator System 1.0

The actuator system later dubbed system 1.0 (see Figure 2.3) was the first actuator system built for FOR 1779 to use the concept described above. Before that, other systems like voice coils and piezo stacks were tested, the former failing because of jamming issues, the latter being impractical for the target amplitudes. A detailed description of this actuator system 1.0 can be found in [8].

Before use, for actuator system 1.0, each bar has to be calibrated manually to produce a decent traveling wave for a given target frequency and amplitude. This is done using reference position sensors (see Section 3.8) to determine the waveform and adjusting phase and amplitude of the input voltages. Online, an acceleration sensor (ADXL377 by Analog Devices [3]) in each bar gives insight into the phase shift between the actuator bars. The originally intended reconstruction of the amplitudes of the actuator

Figure 2.3: Actuator system 1.0.

bars based on the accelerator signals failed mainly due to the high noise level.

The system is driven by a Matlab program making use of the Mathworks Data Acquisition (DAQ) Toolbox to access the National Instruments DAQ PCI (Peripheral Component Interconnect) cards to acquire the acceleration sensor and the reference sensor signals and to drive the electrical currents in the actuator coil via the amplifiers (Thomann, TSA 4-1300, bandwidth 20 Hz to 20 000 Hz [29]). The program provides a GUI (Graphical User Interface) with which the current through the actuator coils and the phase shifts between the currents of the actuators can be defined. The realized phase shifts between the actuator bar movements derived from the accelerator signals can be visualized online. Additionally, during the calibration the output of the reference sensor can also be visualized. The calibration parameters for each amplitude and frequency setting are saved in a data base and can easily be loaded for the experiments.

Wave amplitudes between 250 µm and 500 µm with frequencies between 40 Hz and 81 Hz at a fixed wave length of 160 mm have been generated during the wind tunnel experiments with the actuator 1.0.

Most wind tunnel measurements published to date for the FOR 1779 have been obtained with this system [20][22][23]. Besides the problems with glued bars peeling off the surface, the system is relatively robust, but also limited in its flexibility due to the necessary offline adjustment, which had to be repeated after each installation into the wind tunnel.

2.4 Actuator System 2.0

Figure 2.4: Actuator system 2.0.

After the successful application of system 1.0 a new system was designed, system 2.0 (see Figure 2.4). The goal was to improve spatial resolution by reducing the spacing form 20 mm to 10 mm. This improvement would make the direct numerical simulation of the setup easier since the wavelength could be reduced from 160 mm to 80 mm in turn reducing the volume of the flow that has to be simulated.

Furthermore, a new sensor system was devised using analog light barriers

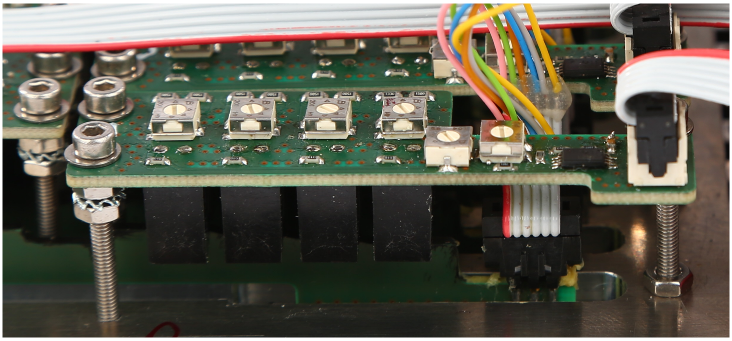

Figure 2.5: The stair light barrier sensor with four analog light barriers (black) soldered to a Printed Circuit Board (PCB) with analog adders mounted to the bottom of actuator system 2.0.

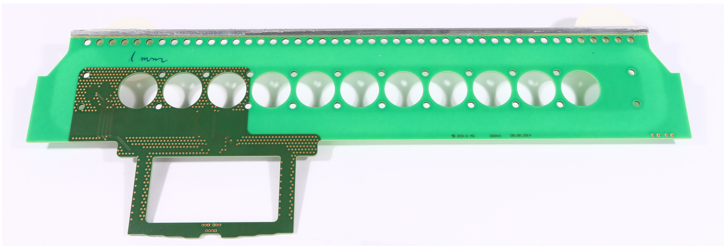

Figure 2.6: The actuator system 2.0 bar design with stair extension (bottom left) and aluminum profile (top).

to directly detect the position of the bars (see also Section 4.2), abandoning the acceleration sensor approach taken in system 1.0, which produced only unreliable position data. Analog light barriers function by measuring how much of a light beam is occluded by an opaque object, in this case the actuator bar, changing their voltage output accordingly. The range of the specific barriers used here is 0.6 mm. For actuator system 2.0 it was extended by adding the signals of four barriers together while the actuator bar has a stairs-shaped extension to block one barrier after the other (see Figure 2.5 and 2.6). This way, as soon as one of the light beams is completely occluded, the next barrier enters its linear measurement range. The outputs of four barriers are summed using analog electronics and generates an approximately linear measurement over a range of ± 1.2 mm, which fully covers the envisioned amplitude range.

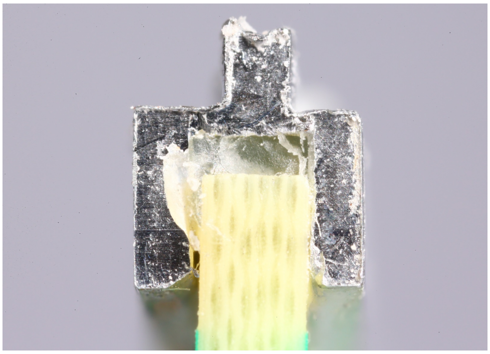

Figure 2.7: Aluminum profile for stabilization and reduction of glue spread glued to top of the actuator bar, which is made of glass fiber reinforce plastic.

Like its predecessor the actuator system 2.0 was driven by an audio amplifier. The amplifier in question (Thomann, TSA 4-1300, see above) is built to drive loads with an impedance of 8 Ω. As shown in Table 2.1, the impedance at target frequency (≈ ohmic resistance) of the coils of actuator system 2.0 is far closer to this value, allowing the amplifier to apply higher power due to higher current at maximum output voltage. Indeed at the time of completion of system 2.0 the system was expected to be capable of peak currents of 3 A without and 5 A with active cooling [8, p. 68]. Assuming sine currents, the peak currents correspond to effective currents of 2.1 A and 3.5 A (see Section 4.4). The high current was expected to make the same or even larger amplitudes possible than in actuator system 1.0. In addition, to the audio amplifier a low bandwidth amplifier, which would be capable of supplying direct current, was envisioned to be coupled with the audio amplifier to overcome the force of gravity on the actuator bars to allow for accurately keeping the zero position level with the surrounding surface.

Due to concerns with the stability of the bars against deformation along y-direction, to help accurate application of the glue and potentially curb the peel off issues experienced before, an aluminum profile was added to the top of the bar (Figure 2.6 and 2.7). This profile offered a slim point of contact with the surface with a light groove running along in the center. This way the profile was expected to confine glue to a very slim region leaving the surface material between the actuators free to move. This effect is difficult to verify with an aluminum surface as optical inspection from below is very limited due to constrained space (further see Section 4.5).

However, it proved much more difficult to establish a traveling wave on this actuator system compared to system 1.0. The introduction of feedback control using the position sensors offers a solution to this problem and the added benefit of increased online flexibility.

2.5 Classification and Comparison to MAKOS

The Lorentz force based system described in this chapter falls in the category of moving surface flow control actuators (for the corresponding taxonomy see [6]). Among actuator systems of this type, the resonant piezoelectric actuator built for the MAKOS project is the most similar one [25]. This system uses piezoelectric actuators with a clever leverage scheme to excite vibrations in thin (190 µm) metal sheets which exhibit high Q-factor mechanical resonances. Since the displacement is large (500 µm) relative to the sheet thickness, the reset force is nonlinear, leading to the broadband resonance behavior of a Dunning oscillator around the operating frequency of 1200 Hz, increasing frequency tuning range compared to a linear oscillator.

The resonant piezoelectric transducers are used in arrays where they can oscillate with adjustable phase shifts between each other. This way, a movement similar to a traveling wave can be produced. In comparison the actuator bars in the system presented in this chapter directly neighbor each other, without any fixture in between, making a traveling wave in the strict sense of the word possible. For this purpose, it forgoes the use of high Q-factor resonances, which makes it less sensitive to the choice of surface material. This flexibility is only possible due to the much lower operating frequencies. However, even at those it remains very challenging to reach similar amplitudes as the resonant system.

2.6 Summary

The actuator system presented in this chapter is driven by Lorentz force, like e.g. electric motors or loudspeakers. The drive mechanism is tailored very specifically to achieve the task of wave actuation at the parameters described in the introduction. It allows for much needed flexibility in wavelength and choice of surface material, while also providing an uninterrupted traveling wave. Due to forgoing the use of mechanical resonances to gain this flexibility the system is limited to frequencies on the order of 100 Hz for high amplitudes.

Two versions of the system have been described, 1.0 and 2.0. They follow the mission statement of developing robust methods for drag reduction in the main changes in their design: the increase of spatial resolution, which was specifically targeted to ease exploration of a larger common parameter space with numerical simulations. The next chapter first gives an overview of the tools (software and hardware) which helped in the design of this control. Then Chapter 5 details the control design and some important changes to the actuator systems, which had to be developed in parallel with the control design.

3 Software Tool Chain and General Purpose Hardware

This chapter gives an overview of the tools, which will be used in the following chapters to develop models and control designs, and to implement control of the actuator system introduced in the previous chapter. The first section describes the use of Matlab Simulink Real Time and the digital control hardware used alongside it. The next sections describe the simulation software COMSOL followed by the 3-bars test actuator system, the software packages for electric circuit design and the mechanical construction and the 3D printer used for the fast production of specific system components. The last section shows various reference sensors used to calibrate and evaluate the actuator system.

3.1 Simulink

As the software tool for control design and modeling of the actuator system Matlab Simulink 2015b [48] was chosen. It is a commonly used computing environment in the control design community. Simulink is particularly appealing as it provides a graphical programming interface akin the block diagrams often used to illustrate and analyze control methods. Matlab is a base software that can be adapted to a specific task by adding software packages called toolboxes (of which Simulink is one).

For interfacing with the hardware Simulink Real Time is an important toolbox. It is used in the so called external mode with the actuator system: an x86 based target computer with special cards providing analog in- and output runs the proprietary Simulink Real Time Operating System (OS). Such an OS is important as it guarantees that a given set of instructions,

Figure 3.1: The test stand with tools and the actuator system 2.1 (see also Chapter 4). The development computer (1) is a desktop PC running a windows OS and Matlab Simulink. It is connected via Ethernet LAN (Local Area Network) to the Speedgoat Performance Target computer (2), wich shows important data on the connected screen (3). In the same box, there are also racks containing amplifiers (4, see Section 4.3) and power supplies (5) for sensors (6, see Section 4.2). Finally, there are the actuator system (7) and a frame holding the position reference sensors (8), whose readout electronics are placed on top of the box (9).

Table 3.1: This table shows the software tools used for control design and some properties of the most important hardware outside of the actuator.

Purpose or property	**Name or value**
Developement software	Matlab Simulink 2015b
Target computer operating system	Simulink RealTime
Target computer type	Speedgoat performance real-time target machine (2017)
Target CPU	Core i7 4-Core, 3.5 GHz (2017)
Target RAM	4 GB
Target ADC Card	1×IO106
Number of channels	64 single ended
Maximum sample rate	200 kSps all simultaneous
Input range	±10 V
Effective number of bits	16
Target DAC Card	2×IO110
Number of channels	2 × 32 single ended
Maximum sample rate	100 kSps all simultaneous
Output range	±10 V
Effective number of bits	16

say, one step of a control algorithm, is fully executed within a certain, relatively short time frame (e.g. 1 ms). In feedback control, it would be problematic if the execution of such a step were delayed, e.g. due to a user input interrupting it, which can in general happen for most modern OSs typically used with personal computers. Meanwhile a development computer running Matlab under such a normal OS, i.e. Windows 8.1, is connected to the target via Ethernet. It compiles the control program from code in the form of a block diagram called the Simulink Model. The resulting binaries are sent to the target machine and the execution is started from the development computer. The Simulink Model is also used as GUI to change parameters of the program, e.g. the amplitude of the wave, manually during actuation, if desired. At the same time the target can display information on the program currently run on a connected screen, e.g. the trajectories of the actuator bars. The test stand with such a setup is shown in Figure 3.1 together with other important tools described in this chapter.

One of the Toolboxes which were used in modeling applications is the System Identification Toolbox. It makes generation of all common excitation signals available, which can be directly fed into a Simulink Model. The data collected by executing the model can then be imported, filtered and fitted to a variety of the most commonly used linear and nonlinear models. In addition, the DSP (Digital Signal Processing) Toolbox is used for its filter design tools and other utilities.

3.2 Speedgoat

As the target computer running the Simulink Real Time OS a custom built system by the Swiss company Speedgoat was chosen. Its specifications are shown in Table 3.1. This choice was made primarily because the Speedgoat systems are especially made for use with Matlab Simulink Real Time [44]. Hardware of other vendors offering the capabilities needed is either not well supported in Simulink Real Time, like National Instruments (NI), who offer their own software solution in Labview, or more geared towards vehicle applications like the Autobox by dSpace. The specific system used here is, besides the high performance Intel CPU (Central Processing Unit) and SSD (Solid State Drive), primarily characterized by the converter cards it contains. They offer more than enough channels, 64 both for in- and output, which is necessary for a system with a high number of actuator bars. With 100 kHz they provide more than sufficient sample rate for the target frequency range of 80 Hz to 135 Hz, as the rule of thumb is to use a sampling rate about 7 to 10 times greater than the dynamics to be controlled.

For digital feedback control hardware the minimum delay between in- and output, also called dead time, is an even more important factor than sampling rate (as it is always higher). For the Speedgoat system a minimum dead time of 21 µs has been given by the manufacturer, composed of 8 µs for input in Direct Memory Access (DMA) mode, 5 µs for 20 outputs and

8 µs for only kernel scheduling of the real time operating system. This time is shorter than the sampling time of 100 µs usually used with the system and much smaller than the relevant time constants of the actuator system of approximately 1 ms. Dead time from other, fully analog hardware in the control loop is negligible by design.

In addition to the hardware installed in the system, the availability of an option of using Field Programmable Gate Array (FPGA) cards to significantly boost computing power of the system was considered important. It served as backup plan in case the algorithm used for control turned out to be too computationally expensive for the Intel CPU alone.

3.3 COMSOL

Simulink and the Speedgoat system are important for controlling and modeling the actuator system. For optimization, a numerical simulation tool which helps predict the impact of planned changes and makes properties that are impractical to measure readily available is essential. As tool for this purpose the COMSOL software suite was selected.

COMSOL works based on the Finite Element Method (FEM), a common technique for solving Partial Differential Equations (PDE) occurring in physics, which often cannot be solved analytically. The object to be simulated is subdivided into the namesake finite elements (e.g. triangles in 2D and Tetrahedrons in 3D). A piece wise continuous trial function, which respects the boundary conditions, is defined for each finite element. In this way a suitable algorithm can iterate on the functions and, thus, approximate the solution of the PDE until the estimated deviation from the solution is considered sufficiently small [42]. COMSOL is one of many available software suites for streamlining the process by taking on the more sophisticated mathematical and programming challenges in the background, letting users focus on the specifics of their problem and even providing guidelines as default settings for an initial approach.

COMSOL is set apart from other FEM software by its focus on multiphysics. It is not necessarily as specialized in some areas as other software, but covers almost all physics simulations possible with FEM. Similar to Matlab it provides modules (the equivalence of Matlabs toolboxes), which are made to deal with specific problems but can also work together seamlessly. For the purposes of this thesis the Structural Mechanics, Shell Mechanics, AC/DC (for low frequency electromagnetism), Heat Transfer and Computations Fluid Dynamics (CFD) module were used (see Sections 4.1.4, 7.2.1 and 7.2.2).

3.4 Altium

Altium is a software for design of printed circuit boards. It was used to design circuit boards for custom sensor assemblies, signal collection and power supply. The primary challenges designers were faced with for this project, were high currents and to a lesser extent limited space. High currents were encountered especially in custom design of an amplifier for the system (see Section 4.3). To properly handle these challenges, a simulation tool similar to COMSOL is integrated in the software. It allows for the analysis of current flow and power dissipation throughout the layout. Geometry can then be adapted to make sure no parts of the board will overheat.

The other important feature for the workflow used is the ability to exchange models of the designs between Altium and the computer aided design software for mechanical design used for the project, Inventor, which is the subject of the next section. This ability helped to make sure the shapes of all PCBs fit into the remaining mechanical setup and was instrumental in overcoming challenges with tight spacing, e.g. the sensor upgrade (see Section 4.2.2).

3.5 Inventor

Inventor is a computer aided design program. It is used to realize 3D computer models for new parts of the actuator system from scratch. Other parts are either imported from their manufacturers who sometimes supply mechanical models for parts like bearings or analog light barriers. Also parts created in other tools like Altium can be transferred. These models are merged into a bigger model of the assembly that is then used to plan ahead and make plans for complex custom mechanical parts. These parts are then manufactured by the in house workshop based directly on the digital 3D data on Computer Numerical Control (CNC) mills (e.g. magnet holders) or 3D printers (e.g. bearing holders). In simpler cases printed drawings also from the software are still competitive by taking up less precious machine time for tasks done just as quickly by hand, i.e. with less hi-tech machines (e.g. drills, saws, etc.).

By providing this interface between planning and building of the actuator setup, and by avoiding most time consuming mechanical errors, this software enables rapid prototyping used to do many of the iterations on hardware described in this thesis.

3.6 3D Printer

The most important tool for rapid iterations on mechanical parts of the actuator system is a 3D printer, the Stratasys Connex3 Objet 350 [45]. It functions by spraying thin layers (down to 16 µm) of liquid photopolymer and quickly curing them with ultraviolet light. For small features or objects (<50 mm) the accuracy of the printer is within 20 µm to 85 µm, while for larger ones (up to 342 mm × 342 mm × 200 mm) it is below 200 µm. This accuracy seemed promising enough that a test was undertaken to print a riblet surface for aerodynamic experiments. Unfortunately, the result was not sufficiently smooth and would have required significant post processing. Therefore this approach was not pursued further. Other parts printed for the actuator system include extensions to attach bearings, slopes for new sensor assemblies and adapters to attach additional bearings to the actuator bar. They still require high precision, e.g. for bore holes to thread screws through or into, but not as strict globally as for a riblet structure and were thus well served with the Objet 350.

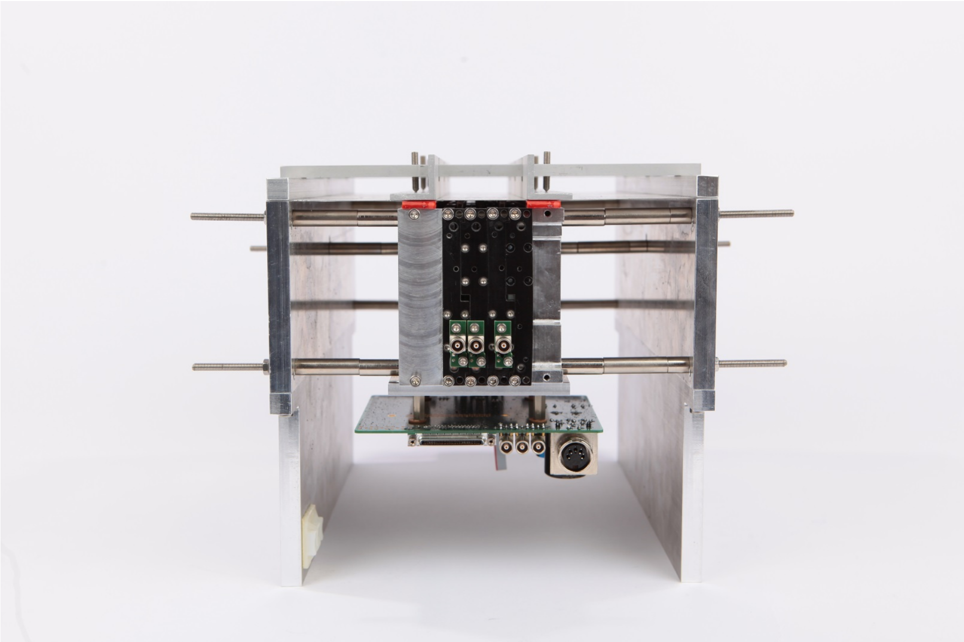

Figure 3.2: The three bar system with clamping. Only the three bar system has no circumferential frame, allowing for plastic counter blocks to be placed below the surface onto which steel L-profiles are pressed with screws. This serves as a way to vary the distance between outer actuators and fixed boundaries.

3.7 Three Bar System

For initial testing a system with only three bars (see Figure 3.2) was built to speed up prototyping by lowering the complexity. It is much less time consuming to place preliminary modifications on three instead of 20 bars, especially if they require some adjustments or calibration (e.g. sensors). The three bar system can also be disassembled and reassembled much easier when a modification does not work or results in the system failing. Also, the surface material is more accessible as the frame is not glued but screwed in (so the material can be re-aligned). And the frame does not fully surround the surface sheet, but lacks sections at the ends of the bars, which allows for clamping down on the surface at freely adjustable

Table 3.2: Most important properties of the National Instruments cards used with the three bar setup.

Purpose or property	PCI 6071E	PCI 6251
Number of channels	2 Outputs	16 Inputs
Maximum sample rate	>400 kHz	1 MHz
Output range	±10 V	±10 V
Effective number of bits	12	16

positions (see Figure 3.2). In all other aspects however, it is built in the same way as the full actuator system 2.0.

As a preliminary solution, before the use of the Speedgoat system, converter cards by NI (two PCI 6071E [31] and one PCI 6251 [30]) were used. This setup was limited by the number of output channels to apply feedback control to up to four bars. Specification of the cards are shown in Table 3.2. Driver support of the cards is available for Simulink Real Time up to version 2015b. This system worked in the same Simulink Real Time external mode, as the system with the Speedgoat target.

As with the Speedagoat system also here dead time is of vital importance to the functioning of the feedback control. Since delay by analog components was unclear the total dead time was tested by step response for the system. No detectable dead time was found, suggesting that it is <100 µs.

3.8 Reference Sensors

Position

In general the purpose of position sensors in the actuator system is to track the displacement of the surface as well as the center of mass of the actuator bar. The former is what has to be controlled for accurate aerodynamic measurements. The latter gives insight into the translation movements of the actuator bar, which is helpful for control. In addition, the rotational

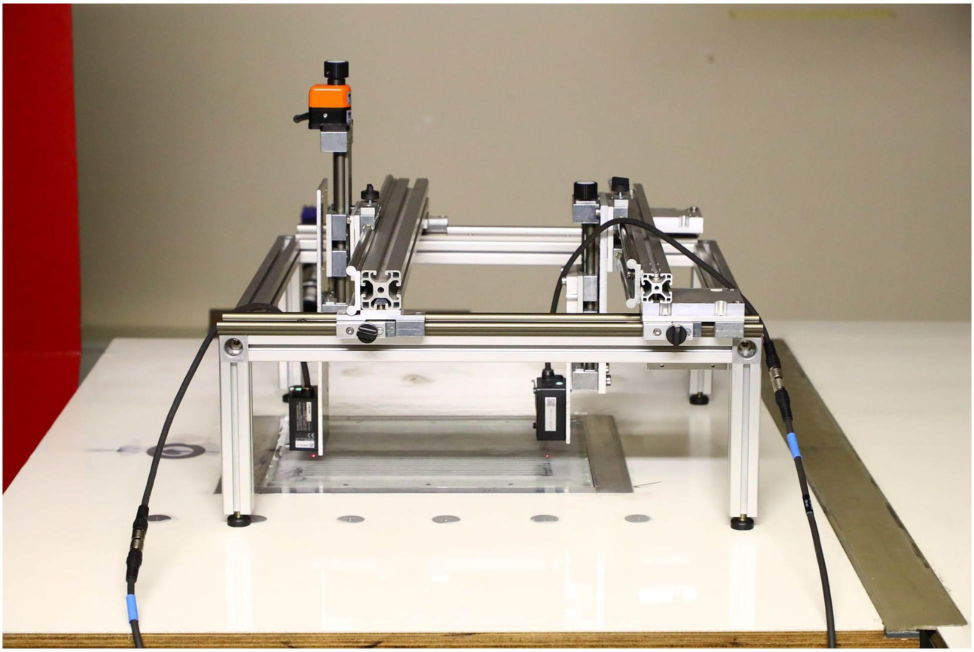

Figure 3.3: Reference sensors (black) attached to an aluminum frame and positioned over the surface of actuator system 2.1 inside the wind tunnel.

oscillations described in Section 4.1.4 should be tracked and, if possible, counteracted.

This task is typically performed by online sensors discussed in Section 4.2. These sensors are needed to develop and run a feedback wave control system making a wider wave parameter range available. However, the online sensors are not pre-calibrated.

Therefore a position reference is needed, which is provided by two Keyence LK-H022 laser triangulation sensors [18]. Each tracks the position of one spot on the surface and can be easily placed over any actuator bar and be quickly removed after calibration and before the start of the experiment (see Figure 3.3).

This is important because it is strictly required to keep the whole set-up including online sensors well below the level of the surface not to disturb the flow above it, which is the subject of the experiment. The tight spacing also limits the selection of sensors in general and is one of the main reasons not to use a larger number of the reference sensors for online tracking.

Force

For additional evaluation of certain setup characteristics other offline sensors are used which do not have an online complement. One of those is the Alluris FMI-B50C5 force sensor [2] mounted on a threaded rod in the FMT-210 test bench. It can measure forces up to 500 N and was used for testing the reset force of the surface (see Section 4.1) and the force exerted by the individual actuator bars (see Section 2.4 and Section 7.3). The error margins given by the manufacturer are $\pm 0.3\,\%$ $\pm 0.1\,\mathrm{N}$.

Magnetic Flux

To verify simulation results, a Hirst GMO8 magnetic field sensor [16] is used (see Section 7.2.1). It is a handheld device with a tip on which a Hall sensor is placed. The tip is small enough to fit into the small gaps left in our actuator system. The sensor provides data with error margins of $\pm 1\,\%$ $\pm 0.1\,\%/\mathrm{K}$.

Temparature

In determining the temperature of coils under load a contact less heat sensor was indispensable. The sensor used is an Ahlborn MR 7843 optical temperature sensor [1]. It has an accuracy of $\pm 1\,\mathrm{K}$ for the measurements taken for this work.

3.9 Summary

The computer hardware is specifically made and provided with drivers for a software suite, which could be used for control design and modeling tasks required in this work. Such a constellation is advantageous as it maximizes time spent on the control design. To provide the interface with the actuator system, the computer is fitted with analog to digital and digital to analog converter cards with 64 channels each and the minimum delay is far smaller than the typical timescale of dynamics in the actuator system. Software for simulation and design of the actuator system has been described. Together with advanced manufacturing tools like 3D printers and a reduced complexity three bar system they enable rapid hardware iterations.

The trajectories on which the actuators move have to be measured to use feedback control and to make sure the correct amplitude is applied during a wind tunnel test. The laser triangulation sensors used for reference can provide very accurate absolute measurements, but would obstruct the flow in the experiment. Therefore, they are mostly used for calibration. Other sensors are not directly involved in the control of the setup, but help understanding specific important properties of the system relevant to its performance. Other reference sensors provide information on force, magnetic flux and temperature. The next chapter shows the models and some upgrades developed using the suite of tools presented here.

4 System Models and System Upgrades

The previous chapters described the system and the tools for analyzing and controlling the system. This chapter revolves around modeling the system according to the laws of physics that govern it and refining this analytical approach, which contains some simplifications. For the analytical model a differential equation is developed from voltage and force equilibria (Section 4.1). This analysis does not account for rotational motion, which is studied in numerical simulations (Section 4.1.4). As a result of the findings of these simulations, changes are made to the actuator system. They include a complete redesign of the sensors to detect and separate center of mass motion and rotation of the actuator bar. Two techniques are proposed, one based on Hall sensors and one based on a different placement of the analog light barriers already in use. The redesigned light barrier arrangement is selected and applied to the system (Section 4.2.2). Other changes made to the system include a different surface material, glue and type of bearings (Section 4.5). A mechanical hysteresis is found in the system but deemed inconsequential for the high frequency behavior. Equipped with all upgrades described in this chapter the system is referred to as version 2.1 up from 2.0. The next chapter describes how control of such a system can be achieved.

4.1 Model from First Principles

The actuator system is an electro-mechanical system and, therefore, governed by the laws of electromagnetism and mechanics. Starting from the electromagnetic behavior, the following will develop a differential equation describing the relationship between input voltages and the position trajectories of the actuator bars. Changing the coil voltage U, results in change of the coil current. This process is of course not instantaneous. The inductivity of the coil, induction due to movement of the coil through the magnetic flux density B and the ohmic resistance R are in an equilibrium with the input voltage.

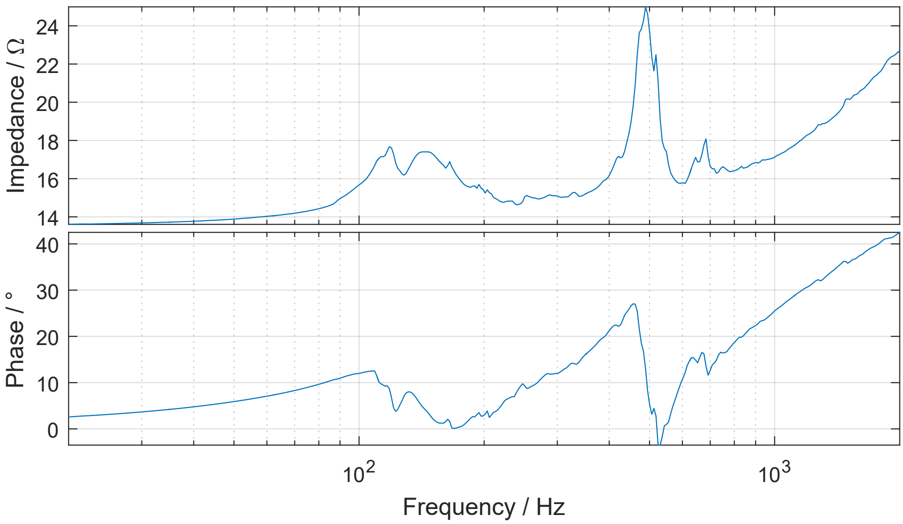

Figure 4.1: This graph shows impedance magnitude and phase for the middle actuator of the three bar test setup over a frequency range from 20 Hz to 2000 Hz. The resonances are mechanical.

The first two influences determine the dynamics of the system. Inductivity L of the coils used is low enough compared to resistance that it only has significant impact above 1000 Hz. Induction due to moving through the magnetic field of the permanent magnets has limited influence at target frequencies as illustrated by a 4 Ω increase over the 14 Ω coil impedance at rest in the three bar 2.0 type test system (Figure 4.1).

The Lorentz force is proportional to the current I in the coil. It is in equilibrium with inertia, viscous friction and reset force. The reset force is modeled as linear spring force between the ith actuator and its next neighbors or, if applicable, the frame. Further away neighbors are not affected in a significant way for the target actuation scenarios. The full force equilibrium for the ith actuator suppressing the index i is (for values of constants see Table 4.1):

$$\frac{lnB}{R} \cdot \left(U - L\dot{I} - lnB\dot{z}\right) = m\ddot{z} + f\dot{z} + cz + c_{-}\left(z - z_{-}\right) + c_{+}\left(z - z_{+}\right) \quad (4.1)$$

In the equation above, l is the effective coil length inside the magnetic field, n the number of turns, m the mass of the actuator bar, z the ith actuator position, z_{-} the $i-1$th, z_{+} the $i+1$th, f the friction coefficient, c the spring constant due to the frame and c_{-} and c_{+} the ones due to the $i-1$th and $i+1$th neighboring actuators. This differential equation can be converted into a transfer function or state space model.

Table 4.1: Constant parameters for Equation 4.1: Resistance R, length l, number of turns n, magnetic flux density B, mass m and spring constants c_{+}, c_{-} and c with regards to previous, next neighbor and the bar itself. The friction parameter f has not been measured.

R / Ω	l / mm	n	B / T	m / g	$c_{\pm}$ / N/mm	c / N/mm
14	400	80	0.54	90	800 to 2400	$\ll 100$

Before that, two assumptions regarding the forces have to be evaluated: friction and reset force. Unfortunately, the friction term in the setup could not be determined by measurements. Based on the design it should mostly be rolling friction from linear or miniature ball bearings and internal friction in the surface material.

4.1.1 Reset Force

The estimation of the reset force performed during the first funding period focused on the nonlinearity [8, pp. 60 – 61]. This term is calculated under the assumption that the force is exclusively caused by the elongation $\epsilon = \frac{\Delta d}{d}$ of the piece of surface material between two actuators with spacing d (see Figure 4.2). The surface material is assumed to be thin (no bending force) with elongated length $d + \Delta d$. The basic relationship of force F and elongation is:

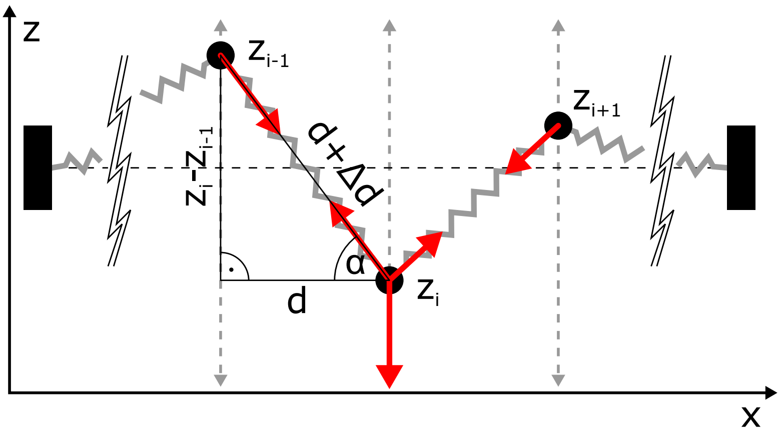

Figure 4.2: Schematic of the elongation of surface material between three actuators. The actuator spacing d gives the unelongated length of the surface between two actuators. The displacements z_{i-1}, z_i and z_{i+1} lead to one of the surface sections being elongated from d to $d + \Delta d$. From these facts a reset force can be calculated.

$$F = EQ\epsilon \tag{4.2}$$

where E is the Young's modulus of the surface material and Q is the cross section perpendicular to the elongation direction. Using the angle α between the x-direction and the connecting line between the displaced surface points, the following reset force pointing in z-direction can be derived:

$$\begin{aligned} F(z_i, z_{i-1}) &= EQ\epsilon \sin(\alpha) && (4.3)\\ &= EQ\epsilon \frac{z_i - z_{i-1}}{d + \Delta d} && (4.4)\\ &= EQ\left(1 - \frac{1}{\sqrt{1 + \left(\frac{z_i - z_{i-1}}{d}\right)^2}}\right)\frac{z_i - z_{i-1}}{d} && (4.5) \end{aligned}$$

The Taylor series approximation around zero of this force is:

$$F(z_i, z_{i-1}) = \frac{EQ}{2}\left(\frac{z_i - z_{i-1}}{d}\right)^3 + \mathcal{O}\left((z_i - z_{i-1})^5\right) \tag{4.6}$$

In an analog way $F(z_i, z_{i+1})$ can be calculated.

The derivation of the nonlinear reset force assumes that the force due to bending the surface material is negligible. This assumption is valid for large displacements. However, for displacements which are very small compared to the material thickness bending is the dominant phenomenon. It is usually described by the Euler-Bernoulli beam bending theory. For the range over which it is valid a common estimate is that the displacement has to be smaller than the thickness of the bar. In the framework of this theory consider three actuator bars. Two are fixed at zero level, one is forced up or down through actuation. Neglecting surface tension, this scenario is equivalent to a simply supported beam with central load, for which the force to displacement relation is [11, p. 909]:

$$F = \frac{6EI}{d^3} z \tag{4.7}$$

This equation is a reordering of the more commonly given result for displacement as a function of force with I being the second moment of area of the beam in question. The fact that the fraction in front of z, effectively acting as spring constant, increases with the inverse of the third power of the spacing d, illustrates the impact of the spacing on the coupling between actuators.

Since the amplitudes intended for the actuator system range from one to five times the surface thickness, linear and nonlinear effects both should have some impact. To ensure an accurate model and compare surface materials, the reset force on the three bar system was measured.

For this measurement the three bar system was modified. The surface was clamped such that the width of the mobile part with the central actuator in the middle was 40 mm in total. Then the force sensor test stand described in Section 3.8 was used to press down at the center while measuring the displacement with the position reference sensors described

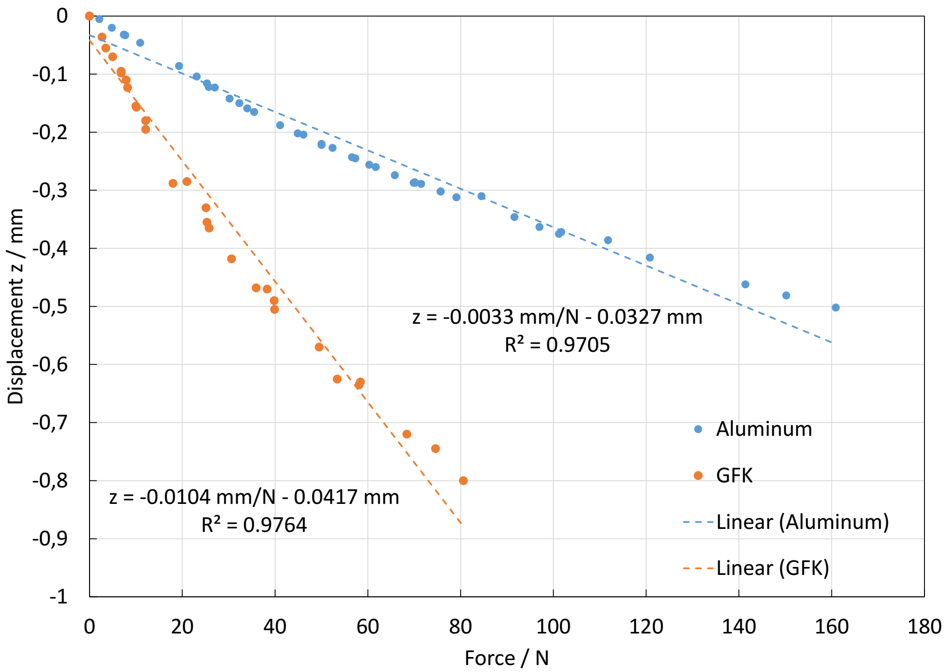

Figure 4.3: Force – displacement relationship in the three actuator test system for aluminum and GRP. Measurements have been performed using the force sensor and test stand described in Section 3.8. The boundaries are fixed at 20 mm distance from the central actuator each. Therefore, the situation corresponds to one actuator displacing a half wave of an 80 mm wavelength.

in the same section. The displacement was increased step by step and the corresponding force was measured. As Figure 4.3 shows, the linear term alone is a good approximation for displacements smaller than the surface thickness, confirming the estimate mentioned above. Beyond that range the impact of the nonlinear term becomes apparent, though it still does not dominate the reset force even for maximum displacement (1 mm) and minimum surface material thickness (0.2 mm). As the theory of modeling and controlling a linear system is far simpler than a nonlinear one, the linear description of the reset force is used in the following as a decent approximation.

4.1.2 Hysteresis

The surface material in the actuator system is subject to high tensile forces between the actuators and between the boundary actuators and the frame. To avoid irreversible deformation in the aluminum surface sheets, a maximum elongation has to be estimated. For this estimation, the same geometric considerations are used as for the calculation of the nonlinear reset force. Since the goal is to find the maximum elongation the value of this maximum is also required. The maximum phase shift between actuator bars considered for operation is 60°. Since the traveling wave has a sine shape along the x-axis the maximum difference in displacement is found symmetrically around the zero crossings. For a given phase shift ϕ and amplitude A it is:

$$\max(\Delta z) = 2A \sin\left(\frac{\phi}{2}\right) \tag{4.8}$$

giving $\max(\Delta z) = A$ for $\phi = 60°$. The elongation is then:

$$\max(\epsilon) = \frac{\sqrt{\Delta z^2 + d^2} - d}{d} = \sqrt{1 + \left(\frac{\Delta z}{d}\right)^2} - 1 \tag{4.9}$$

so for the worst case, which is actuator system 2.1 with $d = 10\,\text{mm}$, $\phi = 60°$ and $A = 1\,\text{mm}$ this would mean:

$$\max(\epsilon) = 5.0 \times 10^{-3} \tag{4.10}$$

This value is barely within the limits for elastic deformation of aircraft aluminum ($\max(\epsilon) \approx 6.0 \times 10^{-3}$ for Al 7075), but comfortably within the limits for GRP ($\max(\epsilon) \approx 4.8 \times 10^{-2}$ for E-glass fibers). However, even for GRP the glue fixing it to the frame might start to creep under high stress.

The result after some use is a slightly deformed sheet forming a bowl shape within the frame when at rest, even with the weight of the actuators compensated for. Only when the upward force exerted on the surface by the actuator exceeds a certain value the surface approaches the zero level given by the frame. While further increasing the upward force, the surface yields more easily than expected and forms a dome, which in turn hinders the return downwards to the zero level. This effect constitutes a mechanical hysteresis, which was measured by slowly moving a 0.2 mm thick GRP surface sheet through 10 cycles, each one lasting 10 s (see Figure 4.4). Fortunately at higher frequencies the effect has far less impact, becoming negligibly small at target frequencies around 100 Hz (see Figure 4.5). Therefore, modeling the hysteresis was not considered to be necessary.

4.1.3 Inductive coupling between the coils

One more point has to be added regarding coupling between actuator bars. Since the magnetic field of the coil might extend to its neighbors it could also lead to an additional coupling. This phenomenon was tested by fixing a bar and its neighbors without a surface in the actuator 2.0 setup and measuring induced voltage at target frequency in the coils of the neighboring bars. It was determined to be lower than 10 % of the input voltage even connected to a high impedance (1 MΩ) measurement oscilloscope. The associated force would be at least 10 times smaller than the total Lorentz force, while mechanical coupling poses a much more significant fraction of the total Lorentz force.

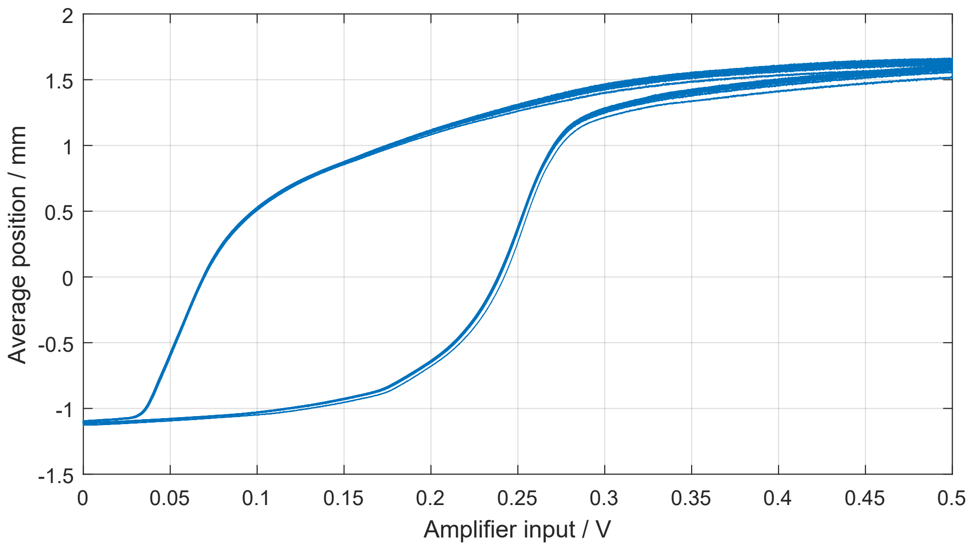

Figure 4.4: Mechanical hysteresis near equilibrium. Each cycle was completed in 10 s. An amplifier input of 0.1 V means a raw force on each actuator of approximately 0.5 N.

4.1.4 Rotational Oscillations

The differential equation describing the actuator system only takes the center of mass movement of the actuator in z-direction into account. The direct connection of the bars to the surface, which is very stiff in x- and y-direction, makes it plausible that movement in this direction and rotation around the z-axis is practically zero. Rotations around x- and y-axis have to be limited by the bearings. To verify these assumptions, a numerical method (FEM) was used. The first problem to be addressed with FEM was the y-tilting [49].

The simulations identified actuator tilting as an effect of eigenmodes shown in Figure 4.6 and 4.7, which are comparable non-tilting and tilting modes. The associated eigenfrequencies are very close to each other. Therefore, disturbances from uneven forces acting on the actuators due to uneven spring force (inhomogeneity of surface material, limited manufacturing precision) and dynamic variations of load on the bearings, and accordingly varying friction force, tilting oscillations are easily excited. Sensors mea-

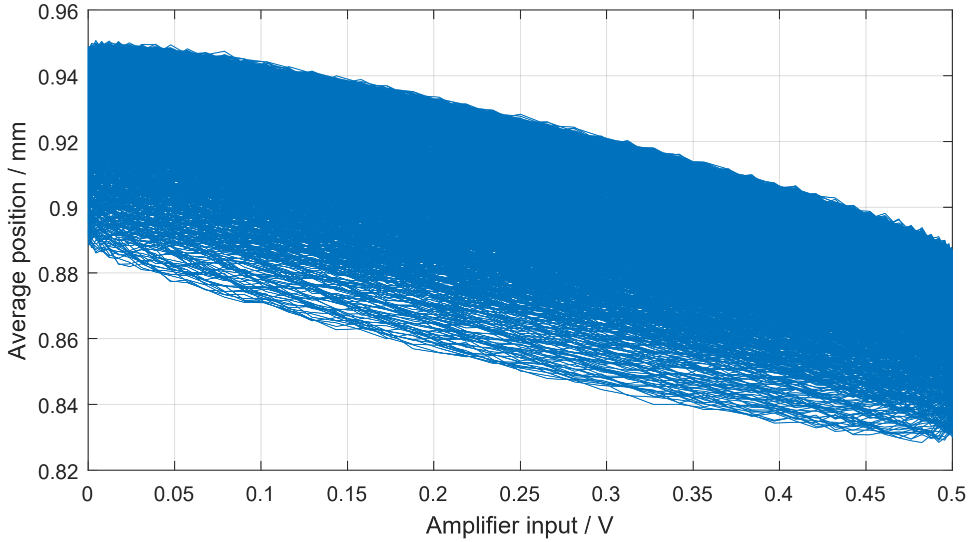

Figure 4.5: Mechanical hysteresis at target frequency. No clear hysteresis curve is distinguishable. Other effects produce stronger variations between the cycles and hysteresis is not as important.

suring the z-position on one end of the bar only, therefore, gave readings inconsistent with the center of mass of the actuator bar. This problem was addressed with a sensor redesign (see Section 4.2.2). Nevertheless, the tilting oscillation may still impact aerodynamic measurements.

Unfortunately, the tilting oscillations cannot be actively counteracted in the actuator system 2.0. Upgrading the setup with additional coils and amplifiers is an option but increases the complexity of the control significantly. In addition, FEM simulations on the placement of additional bearings were performed. They showed that the addition of the bearing shifts the eigenfrequency of the tilting oscillations to such high frequencies ($> 900\,\mathrm{Hz}$) that they do not interfere with actuation at our target frequencies anymore. Due to concerns about the additional weight and mechanical robustness this upgrade was, despite first successful tests on the three bar system, not part of the upgrade from system 2.0 to system 2.1, but part of the later actuator system 3.0 (see Section 7.3).

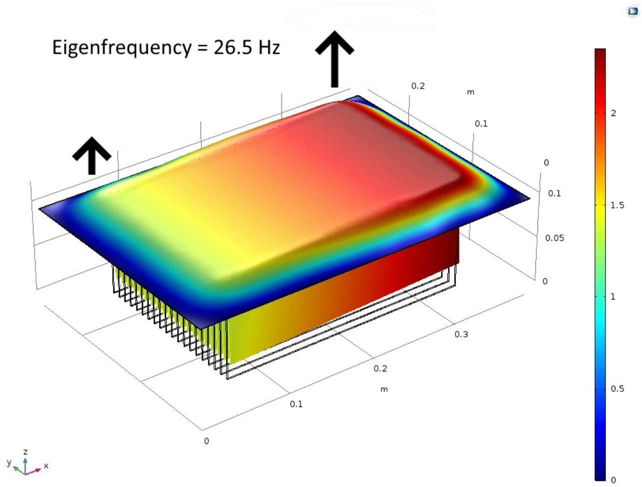

Figure 4.6: Displacement in pseudo-colors on an exaggerated model of the actuator system depicting an oscillation mode where the ends of the actuators move in the same direction (though not necessarily at the same amplitude). This mode has an eigenfrequency of 26 Hz.

4.2 Online Sensors

The most significant improvement made during the upgrade to version 2.1 was the redesign of the online sensors. The problem of y-tilting motivated a sensor design aiming to measure this tilting as well as the true center of mass movement of the bar, which is also a good approximate for the surface displacement. Two methods were studied for this purpose: a different sensing principle based on Hall sensors and a different placement and evaluation of the light barrier sensors [41].

4.2.1 Hall Sensors

One alternative to the reference sensors for distance measurement is a Hall sensor combined with a small bar magnet [21]. Due to its operation principle the Hall sensor only measures the magnetic field in one direction.

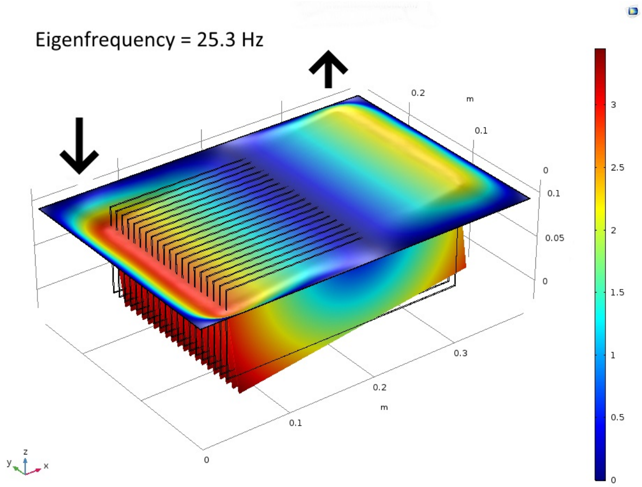

Figure 4.7: Displacement in pseudo-colors on an exaggerated model of the actuator system depicting an oscillation mode where the ends of the actuators move in opposite directions. This oscillation is undesired and has an eigenfrequency of 25 Hz. It is therefore just as easily excited as the desired oscillation.

The sensor was placed as close as possible to the bar magnet for the largest possible signal per unit of displacement. Its measurement axis is oriented orthogonal to the axis of the bar magnet shown in the schematic Figure 4.8. Since the magnetic field of a bar magnet is parallel to its axis at the equator [13, pp 243 – 267], the Hall sensor reading is zero at this point. Moving the magnet up or down results in a change of direction and magnitude of the magnetic field at the position of the Hall sensor and corresponding change of the sensor signal. When moving only between the magnetic poles, this change is monotonic but not linear. It is to be calibrated to position values using the reference sensor.

The x-tilting can be neglected if the sensor is placed close to the bearings in proper orientation. The y-tilting is even less problematic, since the y-component of the field does not contribute to the measurement. For measuring the y-tilting, as is the goal, magnets and sensors are placed at both ends of the actuator bar.

The Hall sensor also picks up the drive coil stray field. To avoid this pick-

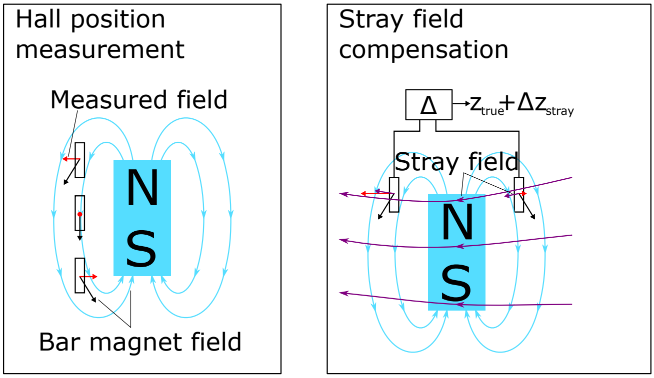

Figure 4.8: This schematic shows the working principle of the Hall sensor based position detection.

up, it was placed as far away from the drive coils as possible since the field decays cubically with distance [13, pp 243 – 267]. However, the existing structure of the actuator system limits placement options and forces the sensors into the stray field. The pick-up and the actuator movement are same frequency sinusoids under typical operating conditions. Therefore, the stray field component cannot be removed by filtering. Nevertheless, by placing two Hall sensors on opposite sides of the bar magnet, it is possible to cancel out the stray field to a certain extent. The accuracy of this approach depends on how much the stray field component parallel to the measurement axis of the Hall sensors changes from one side of the magnet to the other, as shown in the schematic Figure 4.8. Assuming symmetrical placement of the sensors and a symmetrical field around the bar magnet, meaning an equal magnitude but opposite direction bar magnet field at the location of the sensors, one gets:

$$(B_{1,stray} + B_{bar}) - (B_{2,stray} - B_{bar}) = \Delta B_{stray} + 2B_{bar} \tag{4.11}$$

where $B_{1,stray}$ and $B_{2,stray}$ are the stray field components and B_{bar} the bar magnet component. Then ΔB_{stray} is the change of the stray field from Hall sensor 1 to Hall sensor 2. This technique is useful as long as $2\Delta B_{stray} < \min(B_{1,stray}, B_{2,stray})$. The results can be seen in Figure 4.9, deviation from the reference is <10 %.

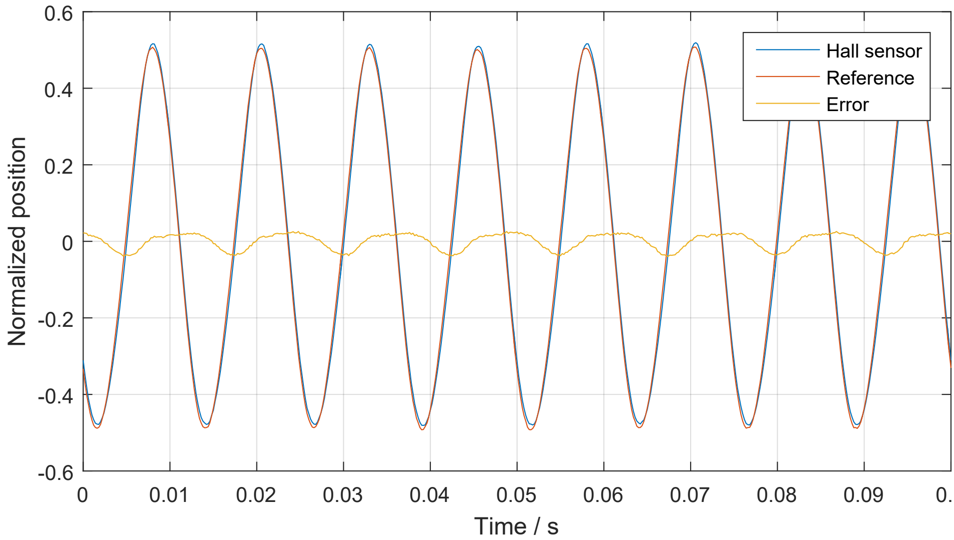

Figure 4.9: This plot shows a test of the Hall sensor based position detection after calibration compared to the reference sensors.

Despite these improvements the performance of the Hall sensor deteriorates in unfavorable stray field conditions. Especially at high phase shift of $\frac{\pi}{4}$ between neighboring actuators the coil currents differ significantly more than in the displayed tests without phase shift. In addition, actuators move less, impeded by their neighbors. Larger ΔB_{stray} and reduced amplitudes have to be expected. For these reasons Hall sensors were not further pursued as position detectors.

4.2.2 Light Barrier Sensors

Analog light barriers were used as position detectors already in the actuator system 2.0. An analog light barrier registers how much of the light beam emitted from one side reaches the other [50]. When inserting a sheet of non-transparent material with a straight edge and clipping the light beam, the position of the edge of the sheet is detected by measuring the sensor output and linking it to a reference position measurement. The maximum displacement the sensor can cover depends on the transversal spatial extent

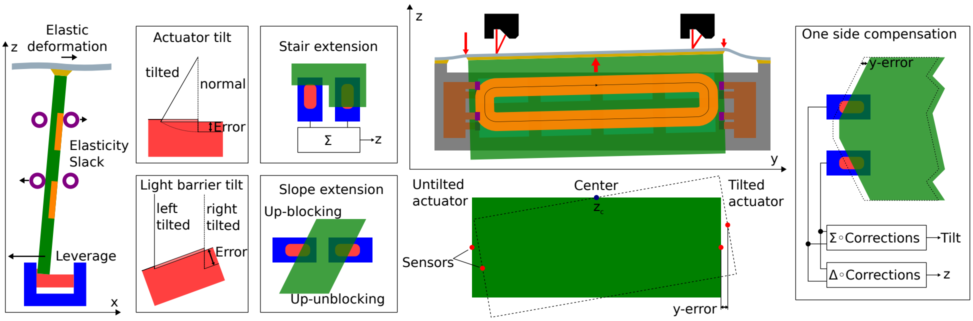

Figure 4.10: This schematic gives an insight in tilting of the actuator as a source of error in light barrier position measurements. It also shows the working principle of the geometric separation of tilting and linear z-direction movement.

of the beam. Unfortunately the maximum range of 0.6 mm of a single light barrier [50] used this way is insufficient.

By using a slope one can extend this distance, trading precision for range (see Figure 4.10). For the target amplitude of ±1 mm a 1:4 slope would be sufficient, extending 0.6 mm of linear range to 2.4 mm. Alternatively, multiple light barriers can be combined with a stair-like edge, such that as soon as one barrier is completely blocked another one takes over. In practice, this is done by summing all analog signals using an operational amplifier, such that in the overlap region one light barrier fades out when the other fades in, creating an approximately linear behavior. This method was used in system 2.0. Therefore, the bars did not include the necessary slopes. Instead of fully disassembling the setup to replace the bars the slopes could be added much faster by 3D-printing extensions of the existing bars, and gluing them to the sides of the bars with the same glue used for attaching the surface material.

Geometrical considerations show that movement in x-direction is largest at the bottom of the actuator bars (see Figure 4.10). Deviations caused by this effect are small, but can be exacerbated if the light barrier is not mounted perfectly perpendicular to the actuator bar. Placing the light barriers on the side of the setup instead, close to the bearings minimizes the amount of x-direction movement and associated disturbances of the measurement.

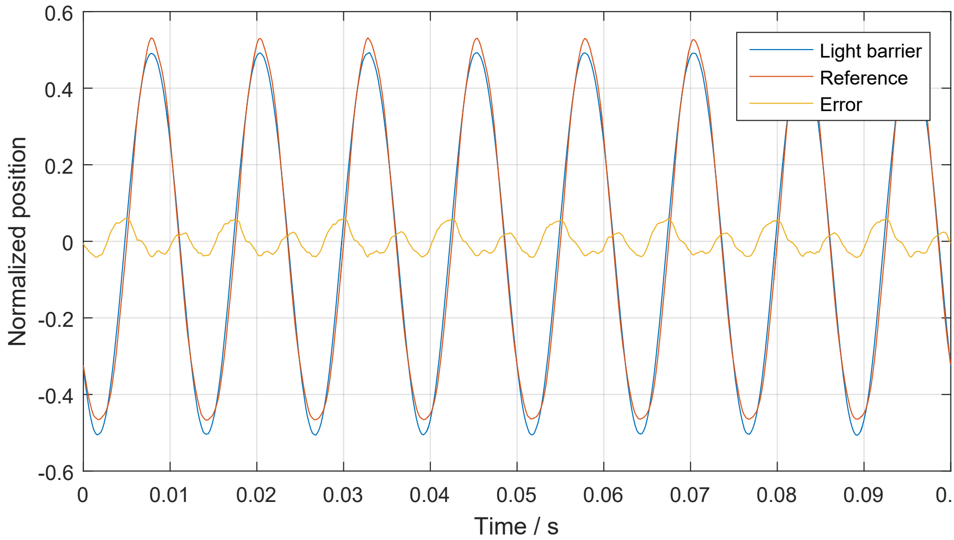

Figure 4.11: This plot shows a test of the dual light barrier sensor based position detection after calibration compared to the reference sensors.

The y-tilting requires compensation with a second sensor on the same actuator bar for the slope configuration. To keep one of the sides of the actuator shaft open for cooling, sensors are mounted on one side only. The configuration shown on the right of Figure 4.10 is used for this purpose. The top sensor is on an up-blocking slope, the bottom sensor is on an up-unblocking slope. The local z_l at the sensors' y-position is determined from the difference of the output voltages of the top sensor u_t and the bottom sensor u_b:

$$z_l = m_{vd}(u_t - u_b) \tag{4.12}$$

The additional constant m_{vd} converts voltage to distance and is attained through calibration. Assuming that the axis of rotation lies within the plain given by the surface in zero position, tilt can be calculated from the sum of the voltages:

$$\Delta z = 2m_{vd}Y\left(\frac{u_t}{Z_t} + \frac{u_b}{Z_b}\right) \tag{4.13}$$

The fixed distances Y from the sensors' location to the center of the bar in y-direction and Z_t and Z_b from the sensors' positions to the zero z-position determine the leverage of the tilting motion. The factor 2 is necessary due to the definition of Δz as difference between the z-positions at the opposite ends of the actuator bar. The center position of the actuator bar z_c can be calculated from z_l and Δz:

$$z_c = z_l + \frac{\Delta z}{2} \tag{4.14}$$

Light barriers reached a similar accuracy as Hall sensors and magnets (see Figure 4.11, deviation is <10 %, typically 3 %) without the drawback of interacting with the coil stray field. Therefore, a more refined version of this sensor unit was built. The full 20 actuator system was fitted with these units complemented by 3D printed extensions (see Figure 4.12) and an adapted collector circuit board.

To use the sensors to their full accuracy, they need to be calibrated with the position reference sensors introduced in Section 3.8. This calibration procedure is automated for each actuator bar. During the procedure all bars are moved in steps alternating up and down without feedback control (as control would require the sensors to be calibrated). The voltages applied to achieve these position changes are a sum of an offset voltage and positive and negative displacement voltages. From the measured output of the sensors after a sufficient settling period of 1 s, and the measured position of both ends of the actuator bar, a calibration table for the sensor is determined. As an example the measurements and results for such a procedure for one light barrier sensor are shown in Figure 4.13.

4.3 Power Amplifier

The computer system described in Section 3.2 on its own cannot supply the electrical power needed to drive the actuator system. High power

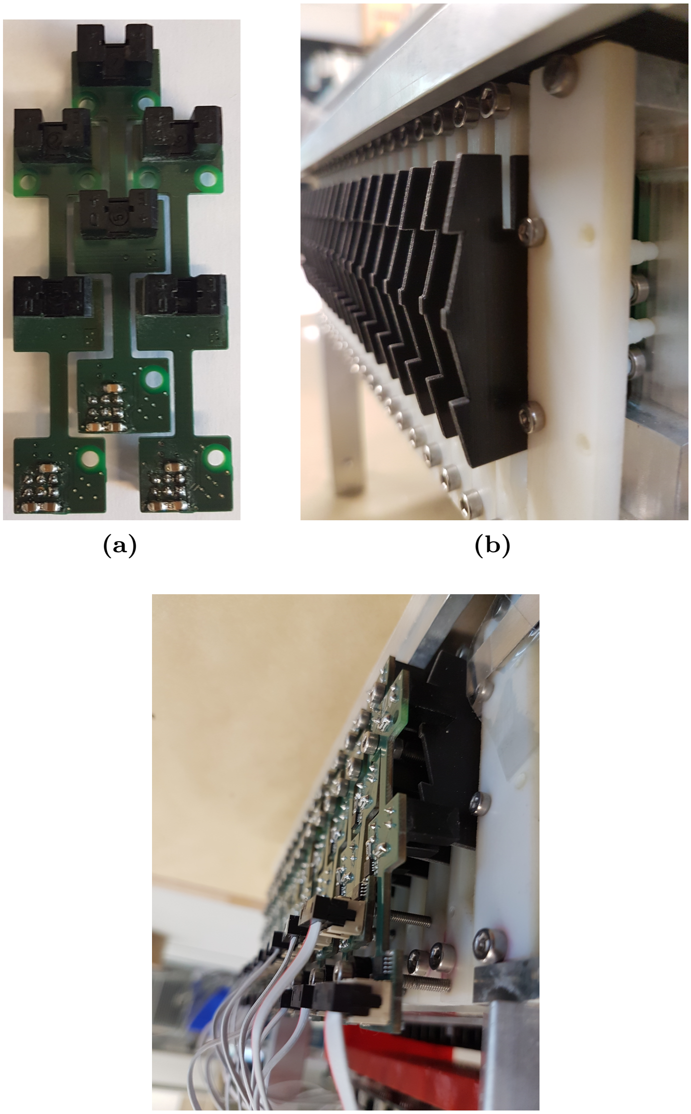

(a) (b) (c)

Figure 4.12: The light barriers have to fit a tight spacing and are mounted on a special PCB for this purpose (a). The black 3D printed extensions (b) are glued to the bar (green) and the sensors are mounted to work on the slopes they provide (c).

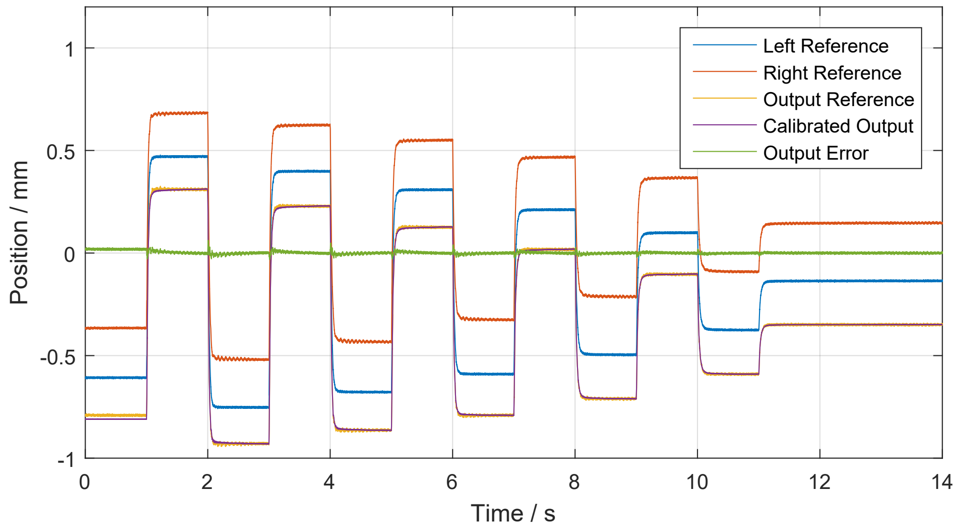

Figure 4.13: This graph shows a time trace of the automated calibration procedure.

operational amplifiers (op-amp) [47] are used to increase voltage and current capacity (two channels, each: maximum 38 V, 5 A continuous, current limited by power supply). Due to its high bandwidth of ≫10 kHz it does not interfere with the wave actuation at 80 Hz to 135 Hz.

The power output of the op-amp is restricted due to the safe operating area. To address this concern, the response of a 2.0 type actuator bar in a 3 bar test system was measured. As can be seen in Figure 4.1, phase angle at operating frequencies of the system is not large enough for the safe operating area to be of concern. It can be reasonably assumed that coils in all systems to be driven by this amplifier will have roughly similar winding numbers and dimensions and, therefore, behave similarly.

For cooling, five power op-amps at a time are set into custom aluminum heat sinks (see Figure 4.14). Air is pushed through these heat sinks by cooling fans. This system is designed for a power dissipation of 1100 W.

Three power supply poles (−38 V, neutral, 38 V) are provided by two power supplies (type TDK RWS1000B) to the op-amps placed together in one rack. The power supplies are capable of supporting 1000 W supply side

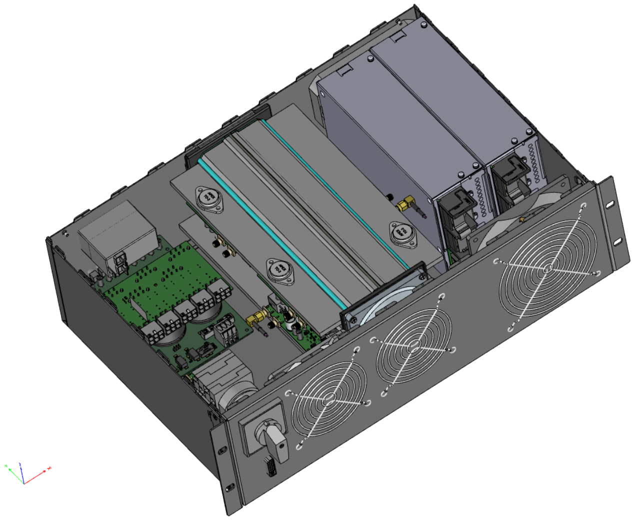

Figure 4.14: The 3D model of the full custom amplifier setup.

power. For 20 Channels two racks of five op-amps and, therefore, a total power of up to 4000 W are necessary, which requires a three phase current supply rated for 400 V and 16 A (11 kW). As peak power is not reached with actuator system 2.1 due to thermal constraints on the actuator system (next section), a single phase power connection (230 V, 16 A, 3.6 kW) is used.

To prevent high output currents during powering the system on or off, the output sockets are initially disconnected from the op-amps by relays. A three setting lever can then be used to close the relay, open it or make it close or open depending on a trigger signal. The latter is typically used with trigger signals sent from the control computer, while the former can help with debugging.

4.4 Ampacity of the Actuator Coils

The Lorentz force in the actuator system, and with it the acceleration and, thus, the maximum amplitude the setup reaches solely depends on

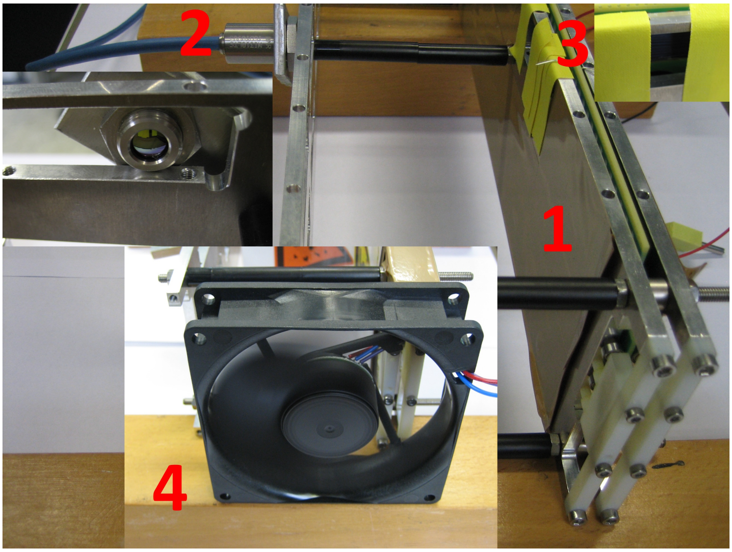

Figure 4.15: A setup for determining the ampacity of a system 2.0 coil. The shaft is closed off with tape on the sides (1), a thermal sensor is placed (2) and pointed at a hole left for this purpose (3). The shaft is covered and a PC fan is placed to simulate cooling from the wind tunnel (4).

the current. All other parameters are practically fixed when the system is built. Therefore, the maximum amplitude will directly depend on the maximum current that can be applied. As long as an amplifier with sufficient output voltage and power is used this limit is determined by the behavior of the actuator bar under the resulting thermal stress, which determines the highest admissible current, the ampacity. Well known, very conservative empirical guidelines are not useful in this context as the goal is highest performance. For this reason tests were conducted to determine ampacity.

For the first test a bar was placed flat on a laboratory desk with the coil facing up. It was heated up by applying direct current with a laboratory power supply with current control (R&S Hameg HMP4040 [37]). In parallel an optical thermal sensor (Ahlborn MR 7843-32) detected the temperature at the coil surface contactlessly. At temperatures above 130 °C the coil detached from the GRP bar due to softened glue and tensions in the coil.

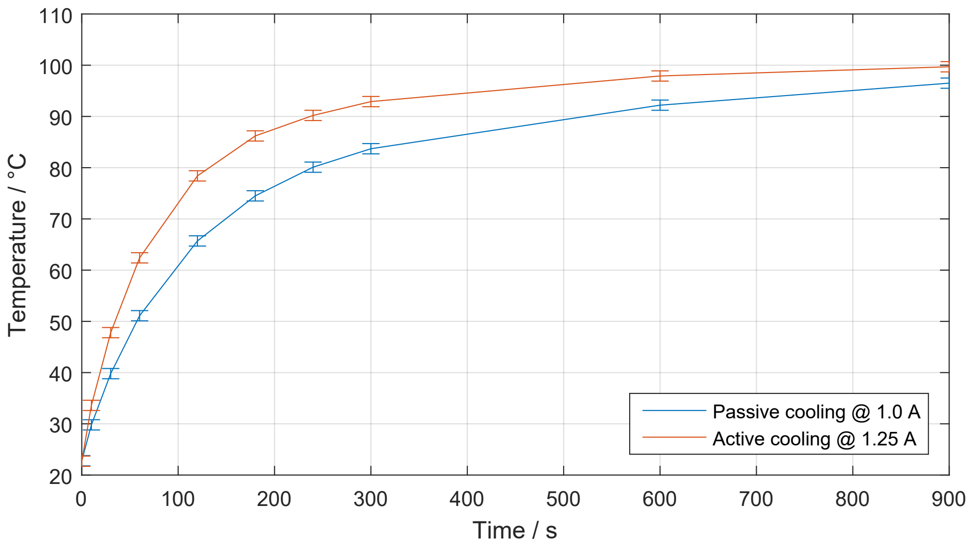

Figure 4.16: Temperature progression during ampacity measurement. The errors are at ±1 °C for the measurement range (see Section 3.8). Only the two measurements used to determine passively and actively cooled ampacity are shown.

The tensions stem from larger thermal expansion on the side facing the GRP bar, which was not cooled as well as the side facing the air. In addition, the glass transition temperature of the specific GRP material used here is in the same temperature range (typically 135 °C [53]), meaning that it would also soften. Therefore, this temperature must not be reached during actuator operation. For safety reasons it was decided, that the ampacity should be determined as the current that would result in a steady state temperature of $\leq$100 °C.

After establishing this temperature limit, the bar was tested in a shaft made from two magnet holders without magnets (see Figure 4.15). All holes were covered with tape except one, which allowed access for the optical temperature sensor. Also the top was closed off as the surface is too close to the top of the holders to allow for ventilation. Tests were conducted without and with a fan blowing air into the shaft. The former is important for the test stand, where usually no active cooling is applied, the latter is closer to the conditions at the wind tunnel which also blows air into the actuator system. In Figure 4.15 results of a thermal test for system 2.0 are shown. The value at 900 s is considered steady state (and no wind tunnel experiment is expected to take longer for one run), resulting in an ampacity of 1.25 A. Thus, the maximum amplitude of the sine current is set to 1.77 A.

4.5 Utility Upgrades in System 2.1

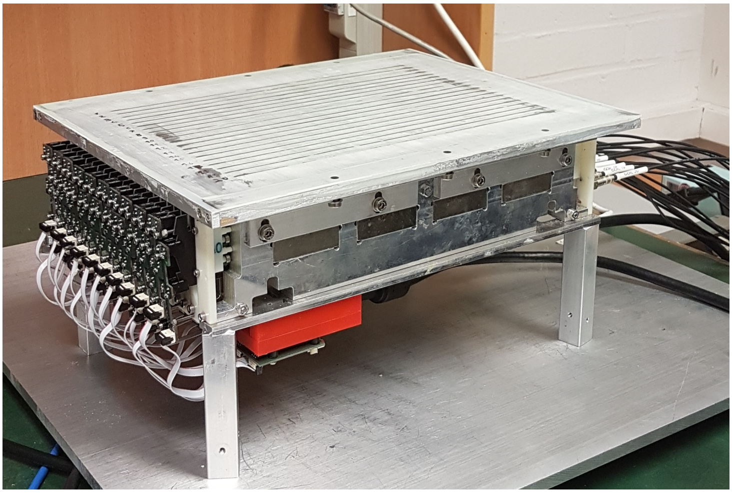

Figure 4.17: Actuator system 2.1.

This section deals with some minor changes, which were made to enhance the performance of actuator system 2.0 and enable the control. After the upgrades the system is referred to as system 2.1, reflecting the significant changes made.

The first step was strictly speaking not within the actuator system: the amplifier described in Section 4.3 was developed, replacing an audio amplifier, which was not capable of supplying direct current. Following this improvement, thermal testing of the actuator bars described in the last section was conducted.

It became clear that the determined ampacity was not sufficient to reach the target amplitude with system 2.0. One of the first approaches to deal with this problem, was testing GRP (of the type FR4, also commonly used for PCBs) of thickness 0.2 mm to 0.3 mm as surface material. It is indeed less stiff at the same thickness (see Figure 4.3). As added benefit it is not prone to performance degrading dents. Thinner aluminum sheets that reach similar stiffness are too fragile for use in the actuator system and are, therefore, no alternative. Finally, the specific GRP we tested has another advantage: it is transparent, allowing for direct inspection of the critical connection between actuator bars and surface.

To accommodate GRP as new surface material, the glue connecting bars and surface was changed from Loctite 9466 to Loctite HY 4090 hybrid glue [15]. Using this glue, bars did not detach due to peeling anymore. In absence of a reason for decreased peeling forces this observation suggests that this material and glue combination is better suited for the task than the previous one.

Another part which was upgraded were the bearings. Miniature ball bearings (Schaeffler SMR63-2Z based on DIN 625-1) at either side of the actuator bar at both ends replaced the linear bearings (see Section 2.1). The reason for switching to ball bearings was that the linear bearings could not apply their guidance in y-direction properly due to jamming issues. They also had individually strongly varying dynamic friction. When bearings with different amounts of friction are mounted on opposing ends of a bar, this factor, among others, can lead to tilting oscillations where one end of the actuator bar is not moving up and down on the same trajectory as the other. The miniature ball bearings are not pressed onto the actuator bar to avoid unnecessary friction. Therefore, they allow limited x-tilting through slack and elasticity of their 3D-printed holders.

4.6 Summary

The actuator system has been described in terms of the physical laws governing it and the respective differential equation has been deduced following some significant assumptions. These assumptions have been challenged as the function of bearings is studied more closely and numerical simulations on this basis find that bars tend towards a y-tilting motion. As a solution an additional bearing is determined sufficient by the simulation.

However, additional considerations predicted a degrading of the system performance and a mechanical weakening of the overall construction. Therefore, this additional bearing has not been implemented.

The sensor redesign has made it possible to separately detect the center of mass trajectory and the tilting. Two concepts have been examined, Hall sensors and light barriers placed on a slope, of which the Hall sensors were too susceptible to coil stray fields and thus the light barrier based sensors have been applied to the system.

The development of an amplifier capable of direct current output especially for the actuator system has also made higher voltages and currents possible. For this reason, the ampacity of the coil has been determined. It is too small to achieve the target amplitudes.

To achieve higher amplitudes at the target frequencies with the system, a softer surface material in the form of GRP and different bearings have been applied. Glue type has also been changed in response to the change of surface material. This improvement has led to less failures due to peel off and revealed a mechanical hysteresis effect not considered previously. Evaluating this effect shows that it will not interfere with wave actuation at target frequency, but has to be taken into account for steady state. According to the upgrades the system version number is changed from 2.0 up to 2.1.

In the following chapter the control design is developed using a three bar test system 2.0, which happened hand in hand with the described upgrades.

5 Control Design

Control is the central topic of this thesis. The actuator system 2.0 does not behave as straightforwardly as its predecessor system 1.0. For the older system a few hours of manual calibration with the help of the reference position sensors were needed to find settings for a decent number of parameter sets. For system 2.0 it required a whole workday by an experienced operator to manually adjust the bars to achieve a traveling wave of sufficient quality for one (!) parameter set. When instead using an appropriate control method high quality waves can be established within a few seconds and parameter sets can be changed online. The ability to change the wave parameters online is a prerequisite for flow control under unsteady inflow conditions, which was one essential task of the second funding period of FOR1779. In the following the methods tested for designing such a control are explored, using the hardware described in Chapter 3. First tests are done on a three bar system 2.0, and after a proof of concept stage is reached, the 20 bar system 2.1 is approached.

Almost every control design relies on models. An analytical model based on the basic laws of physics governing the system has been described in the previous chapter. Transformations of this model used for control design are presented in this chapter. Proportional Derivative (PD) control (Section 5.1.2) and various versions of Iterative Learning Control (ILC, Section 5.3) are elaborated along with a transfer function model (Section 5.1.1), a state space (Section 5.2) and a static gain phase matrix model (Section 5.5). For the final concept, Proportional Integral (PI) control with a dead zone (Section 5.4), feed forward decoupling (Section 5.6) and ILC are merged (Section 5.7). This final concept proved to successfully control the 20 actuator system 2.1. The detailed verification of the controlled actuator system 2.1 is presented in Chapter 6.

5.1 Proportional Derivative Control

5.1.1 Transfer Function for One Bar

The transfer function model, derived from the analytical model described in Chapter 4, is well suited for the description of single input single output (SISO) systems. By assuming the neighboring actuators to be fixed the differential equation 4.1 can be Laplace transformed into:

$$\frac{dz}{dU} = \frac{\kappa}{Lms^3 + (\kappa^2 + Rm + Lf)s^2 + (Rf + L\bar{c})s + R\bar{c}} \tag{5.1}$$

with $\kappa = lnB$ and a linear spring stiffness $\bar{c} = c + c_- + c_+$. To identify the parameters of this equation, the middle actuator of the 3-bar test system was driven by a sine signal and its trajectory, including the transient response at the start, was measured. Input and output at 80 Hz and 0.25 mm amplitude were used to fit a third order transfer function. This fit was validated by comparison to other parameter combinations (the same as seen in Table 5.1). The result was the plant model:

$$\tilde{P} = \frac{K_S}{(1 + T_1 s)(1 + T_2 s)(1 + T_3 s)} \tag{5.2}$$

with $K_S = 0.171\,\mathrm{mm/V}$ and $T_1 = 5.6\,\mathrm{ms}$, $T_2 = 5.9\,\mathrm{ms}$, $T_3 = 0.27\,\mathrm{ms}$.

5.1.2 PD Control Design

For the 3 bar test system a Proportional Differential (PD) control was realized. Because the boundaries holding up the surface material were much closer than in the 20 actuator system, integral action for zero level control was not required. For model based tuning of the control, the transfer function model for one bar described in the previous section was used. The time constant of the slowest system dynamic was determined and used as the derivative time $T_V = 5.9\,\mathrm{ms}$ for the PD controller. The stable range for the controller gain was determined using the root-locus method to be any gain $K_R > -5.8\,\mathrm{V/mm}$. With settings of K_R of $110\,\mathrm{V/mm}$ to

Table 5.1: Parameters (Frequency f, Amplitude A and controller gain K_R) and achieved phase shifts $\Delta\phi$ for PD control of one actuator bar in the three bar setup.

f / Hz	A / µm	K_R / V/mm	$\Delta\phi$ / rad
40	250	40	0.544 π
40	500	40	0.685 π
60	250	40	0.679 π
60	500	40	0.691 π
81	250	40	0.817 π

130 V/mm in simulation this controller worked well controlling the transfer function model of the system.

The controller was then implemented using Simulink Real Time and was tested at different amplitudes and frequencies. Results are shown in Table 5.1. The controller gain used in the simulation had to be reduced for stability reasons. This method yielded an increasingly worse reference tracking with increasing frequency, especially regarding the phase.

Nevertheless the method was extended to three bars, each treated independently, as if it was a SISO system. The parameters of the control were tuned independently of the transfer function model and the simulation step was omitted. To reduce high frequency oscillations at aggressive controller settings, a first order low pass filter for the derivative part was added with a filter time constant of $\tau_f = 13\,\text{ms}$. The original reference phase shift between the actuators of 30° was reduced to 15°, for which the control was moderately successful at 40 Hz to 60 Hz, 250 µm to 500 µm.

In conclusion, the tests of PD control showed that a different method is needed for wave control. In the next sections other, more advanced models and control methods as well as essential sensor upgrades will be presented, which paved the way to controlling a system with 20 actuators within target wave parameter ranges.

5.2 Multiple Input Multiple Output State Space Model

For a description of a system with N actuator bars, neglecting non-linear properties, a linear time invariant state space description is used. The basic form is:

$$\dot{\mathbf{x}}(t) = A\mathbf{x}(t) + B\mathbf{u}(t) \tag{5.3}$$
$$\mathbf{y}(t) = C\mathbf{x}(t) + D\mathbf{u}(t) \tag{5.4}$$

For the actuator system the D-matrix is zero, as it is very common in physical systems, which means that inputs do not affect any outputs instantaneously. The $3N$-entry state vector $\mathbf{x}$ consists of time derivatives of the position, to which other important values are proportional:

$$\mathbf{x} = \begin{pmatrix} z_1 & \dot{z}_1 & \ddot{z}_1 & \dots & z_N & \dot{z}_N & \ddot{z}_N \end{pmatrix}^\intercal \tag{5.5}$$

The N-entry input vector $\mathbf{u}$ consists of the input voltages:

$$\mathbf{u} = \begin{pmatrix} U_1 & \dots & U_i & \dots & U_N \end{pmatrix}^\intercal \tag{5.6}$$

Only positions are measured, so the output matrix C is $3N \times N$ and maps the positions in the state vector $\mathbf{x}$ to the output $\mathbf{y}$:

$$C = \begin{pmatrix} 1 & 0 & 0 & 0 & 0 & 0 & \dots & 0 & 0 & 0 \\ 0 & 0 & 0 & 1 & 0 & 0 & \dots & 0 & 0 & 0 \\ \vdots & \vdots & \vdots & \vdots & \vdots & \vdots & \ddots & \vdots & \vdots & \vdots \\ 0 & 0 & 0 & 0 & 0 & 0 & \dots & 1 & 0 & 0 \end{pmatrix} \tag{5.7}$$

The input matrix B is $N \times 3N$ and straightforward to derive:

$$B = \begin{pmatrix} 0 & 0 & \dots & 0 \\ 0 & 0 & \dots & 0 \\ \frac{1}{L_1} & 0 & \dots & 0 \\ 0 & 0 & \dots & 0 \\ 0 & 0 & \dots & 0 \\ 0 & \frac{1}{L_2} & \dots & 0 \\ \vdots & \vdots & \ddots & \vdots \\ 0 & 0 & \dots & 0 \\ 0 & 0 & \dots & 0 \\ 0 & 0 & \dots & \frac{1}{L_N} \end{pmatrix} \tag{5.8}$$

The most important part of this description is the system matrix A, which is $3N \times 3N$. This matrix has to be composed in such a way that it contains internal effects which lead to the dynamics the system shows including the coupling between actuator bars. Keeping the state vector and the differential Equation 4.1 in mind the matrix can be assembled. The following representation is composed of 3×3 block matrices, the center one on the overall main diagonal, showing the coefficients relating to the ith actuator bar and its coupling to its neighbors, with the substitution $\kappa_i = l_i n_i B_i$:

$$A = \begin{pmatrix} & & \dots & 0 & 0 & 0 & \dots & & \\ & & \dots & \frac{c_{i-1,i}}{m_i} & 0 & 0 & \dots & & \\ \vdots & \vdots & \ddots & 0 & 0 & 0 & \ddots & \vdots & \vdots \\ 0 & 0 & 0 & 0 & 1 & 0 & 0 & 0 & 0 \\ \frac{c_{i-1,i}}{m_{i-1}} & 0 & 0 & -\frac{c_i + c_{i-1,i} + c_{i,i+1}}{m_i} & -\frac{f_i}{m_i} & \frac{\kappa_i}{m_i} & \frac{c_{i,i+1}}{m_{i+1}} & 0 & 0 \\ 0 & 0 & 0 & 0 & -\frac{\kappa_i}{L_i} & -\frac{R_i}{L_i} & 0 & 0 & 0 \\ \vdots & \vdots & \ddots & 0 & 0 & 0 & \ddots & \vdots & \vdots \\ & & \dots & \frac{c_{i,i+1}}{m_i} & 0 & 0 & \dots & & \\ & & \dots & 0 & 0 & 0 & \dots & & \end{pmatrix} \tag{5.9}$$

Thus, we have a state space model containing some variables, which are well known (e.g. mass of the actuator bar, ohmic resistance of the coil, the product lnB as a result of force per current measurements). Some variables can be relatively accurately determined by simulations (e.g. B). Other variables are difficult to measure directly or to be determined by simulations (e.g. L, f, c). This fact severely limits the accuracy in case the model is used with a priori information only. The next section will describe a way to improve this situation.

5.2.1 Greybox Model Identification

To improve the state space model presented in the previous section, the parameters, which are difficult to identify, were determined by fitting the model to input-output measurements of the actuator system. Where the parameters measured on their own are very accurate, no fit was necessary. Other parameters were restricted to stay within realistic bounds. In some cases this procedure can avoid that a fit to limited amount of sample data converges into a physically unsound parameter set, which in general gives wrong predictions and would, therefore, be a bad model. The Table 5.2 shows, which of the parameters were restricted, the respective values, and those, which are not restricted. As it is evident there, restrictions were very loose.

Table 5.2: Parameters or parameter ranges and restrictions of these based on direct measurement.

Parameter	**Minimum**	**Maximum**
Mass in kg	0	0.1
Specific force (lnB) in N/A	0	∞
Inverse inductivity in 1/H	0	∞
Ohmic resistance in Ω	10	20
Spring stiffness in N/mm	0	∞
Friction coefficient in 1/s	0	∞

To facilitate the fit and accommodate the restrictions, the Matlab System Identification toolbox is used. For fitting a model with fixed, restricted and open parameters the tool is fed the state space matrices and a list

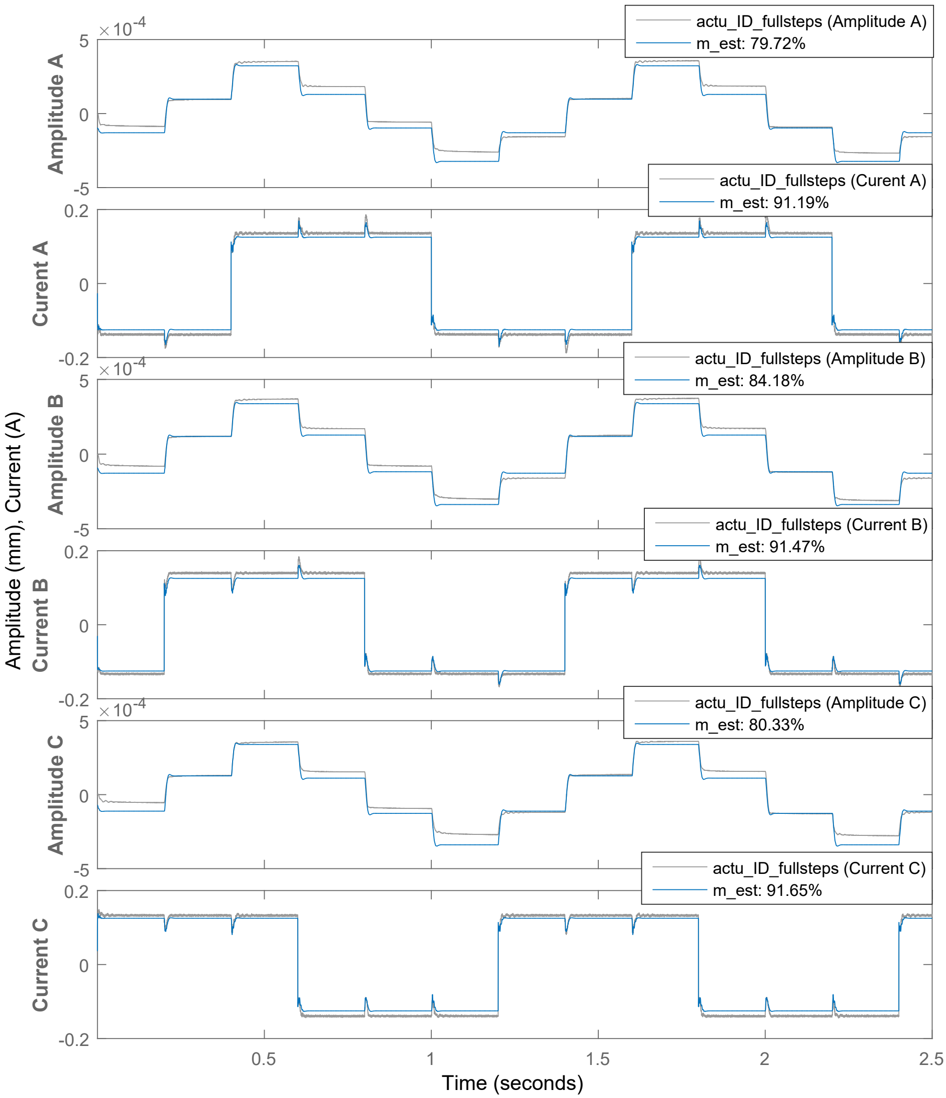

Figure 5.1: Graph of the output of the greybox model, which was fit to this measurement with step excitation and a measurement with chirp excitation (see Figure 5.2).

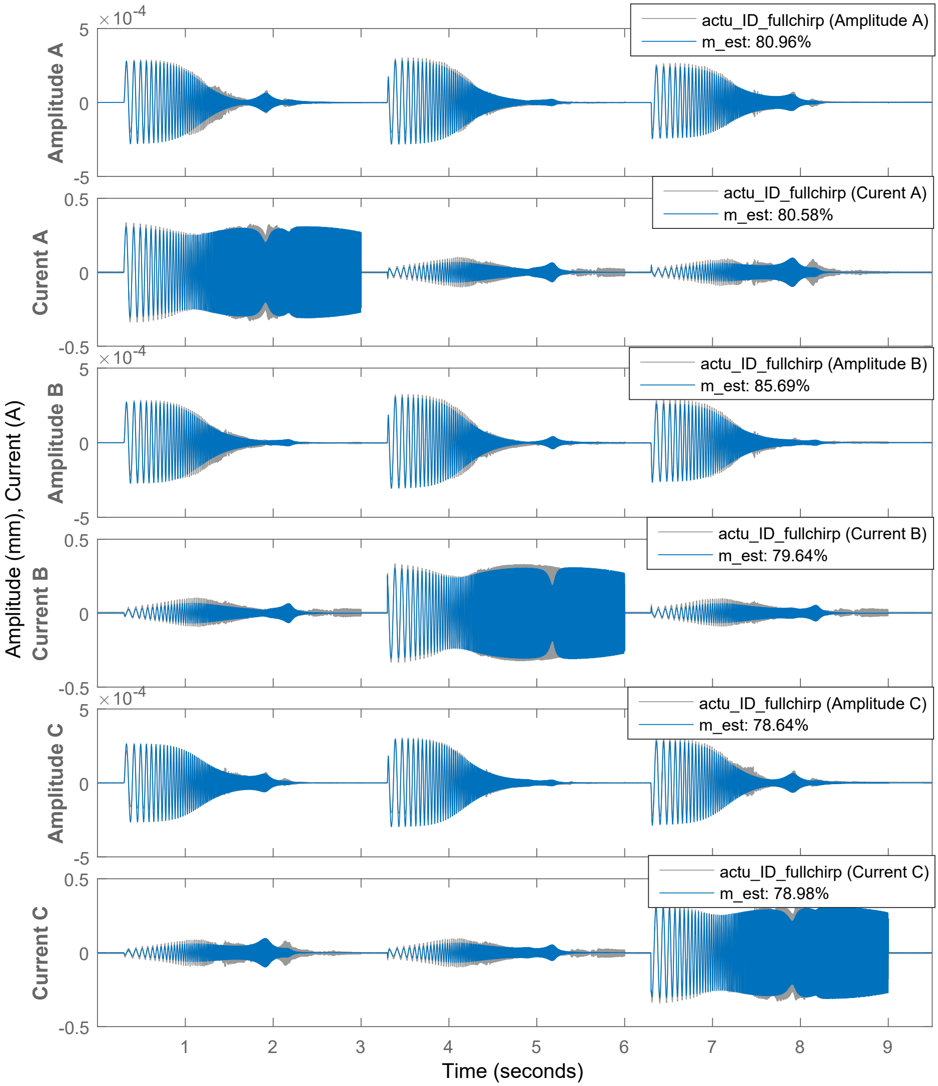

Figure 5.2: Graph of the output of the greybox model, which was fit to this measurement with chirp excitation (10 Hz to 2000 Hz) and a measurement with step excitation (see Figure 5.1).

with the restrictions on the parameters. These are then fit to time series data of input and output variables.

These input/output data were determined in two experiments. They involved exciting the bars with two different predetermined voltage signals. One consisting of steps (see Figure 5.1) and one of frequency sweeps from 10 Hz to 2000 Hz (see Figure 5.2).

The Normalized Root Mean Square Error (NRMSE) of around 80 % reached by the fit is usually assumed to be more than sufficient for the purpose of feedback control. To take advantage of this model, a control design fitting the task of wave actuation in the form of Iterative Learning Control is described in the next section.

5.3 Iterative Learning Control

Iterative Learning Control (ILC) can be applied to stable or stabilized plants to make use of a periodicity in a given reference and corresponding disturbances. It usually deals with a batch process, where the same action (e.g. forming of parts in a production line) is repeated with breaks in between, or a continuous process without breaks (e.g. keeping a read-write head in a hard disk drive on track). These were historically separate concepts, with the latter being called Repetitive Control. However, it was shown that they are mathematically equivalent (see [52]) and the term ILC is now, and will be in the following, used for both.

Wave control for the actuator system requires tracking of a periodic reference, i.e. phase shifted sine signals. Also the main disturbances are periodic. During converged wave actuation these disturbances are: the nonlinearity of the reset force for large displacements, asymmetries due to manufacturing margins, changes in friction due to the actuator being pressed into the bearings over fixed parts of its trajectory. Steady state disturbances like gravity will be fully corrected due to the integrating behavior of standard ILC. These facts show that ILC is a very good fit for controlling the actuator system in steady state. The challenge lies in ensuring convergence and taking care of parameter changes. In the following the very general parametric ILC is discussed, loosely following the remarks in [35] and [34].

The working principle of ILC can be thought of as a mix of steering and feedback control. ILC is typically implemented in digital, discrete time control systems. There each period an integer number of n samples is processed, depending on the sampling rate and period length. The control action u_k and controlled variable y_k during the kth period are vectors:

$$u_k = \begin{pmatrix} u_k(0) & u_k(1) & \dots & u_k(n) \end{pmatrix}^\mathsf{T} \tag{5.10}$$
$$y_k = \begin{pmatrix} y_k(0) & y_k(1) & \dots & y_k(n) \end{pmatrix}^\mathsf{T} \tag{5.11}$$

and the relationship between them is described using the transfer function operator in shape of the $n \times n$ matrix P, the free system response to inital conditions f_k and the disturbances d_k:

$$y_k = Pu_k + f_k + d_k \tag{5.12}$$

For LTI systems P is a Toeplitz-matix made up of the coefficients $p_0 \dots p_n$ of the one period discrete time impulse response of the system:

$$P = \begin{pmatrix} p_0 & 0 & \cdots & 0 \\ p_1 & p_0 & \ddots & \vdots \\ \vdots & \ddots & \ddots & 0 \\ p_n & \cdots & p_1 & p_0 \end{pmatrix} \tag{5.13}$$

All operators described in the following are of the same $n \times n$ matrix structure (though not necessarily Toeplitz), which results in the parametric formulation of the ILC.

For the initial period, the reference r is processed by a feed forward operator F and the resulting n sample long control action vector u_0 is saved to memory signified in the block diagram by a one iteration delay block, z^{-1} (see Figure 5.3). Assuming no offset or disturbance and steady state initial conditions, during this initial period the controlled variable

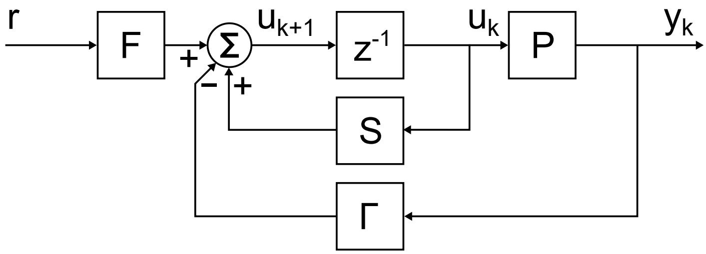

Figure 5.3: Block diagram of a basic ILC.

y_0 remains at zero and the calculated control action is just the same as with pure feed forward steering. During the following periods, e.g. the kth period, the current control action u_k is applied from the memory. At the same time the current trajectory of the control variable is measured as $\tilde{y}_k$ and modified by a learning operator Γ to be subtracted from the sum of fed forward reference and the control action to give the next control action trajectory u_{k+1}. The next control action trajectory is saved, replacing the current one. When the kth period is over, the cycle repeats and u_{k+1} is applied to the system. Thus a successful ILC improves the initial one period feed forward control action by using feedback. Such a concept can be written in terms of the learning law:

$$u_{k+1} = Su_k + Fr - \Gamma M \tilde{y}_k \tag{5.14}$$

In this learning law additional operators S on the previous control action and M on the measured control variable are introduced. The operator M can be applied to suppress measurement noise. In the following we use $M = I$ (I is the identity operator) as sensor noise was not a concern with the actuator system. The steering operator S introduces a mechanism for "forgetting" e.g. high frequency components of the previous control action trading control bandwidth for robustness. Often the learning operator Γ and feed forward operator F are chosen to be the same, which gives a simple set-actual comparison. These simplifications lead to the simplified learning law:

$$u_{k+1} = Su_k + \Gamma\left(r - \tilde{y}_k\right) \tag{5.15}$$

From its structure a system matrix for such an ILC and plant can be derived [35] to be:

$$S - \Gamma P \tag{5.16}$$

The criterion for stability is based on the eigenvalues of this system matrix. Let λ_i be these eigenvalues. The ILC is stable if and only if [35]:

$$|\lambda_i| < 1 \quad \forall i \in \{1, \ldots, n\} \tag{5.17}$$

5.3.1 Gain Switching ILC

In previous work for FOR 1779 an ILC applied to the actuator system was studied in simulation [8, pp. 62 – 69]. The task was to control a model of a coupled 10 bar system using the driven oscillator model with nonlinear reset force and viscous friction (see Section 4.1). Electrical effects were neglected.

For the simulation a PD-type SISO ILC was selected which would control each bar individually, treating the coupling as a disturbance. The PD-ILC is named after the structure of its learning filter:

$$\Gamma = k_p I + k_d D \tag{5.18}$$

where I is the identity matrix and D is a derivative matrix of the form:

$$D = \begin{pmatrix} -1 & 1 & 0 & \cdots & 0 \\ -0.5 & 0 & 0.5 & \ddots & \vdots \\ 0 & \ddots & \ddots & \ddots & 0 \\ \vdots & \ddots & -0.5 & 0 & 0.5 \\ 0 & \cdots & 0 & -1 & 1 \end{pmatrix} \tag{5.19}$$

This form is based on the central difference approximation of the derivative. The steering filter was chosen to be $S = I$, which offers high bandwidth

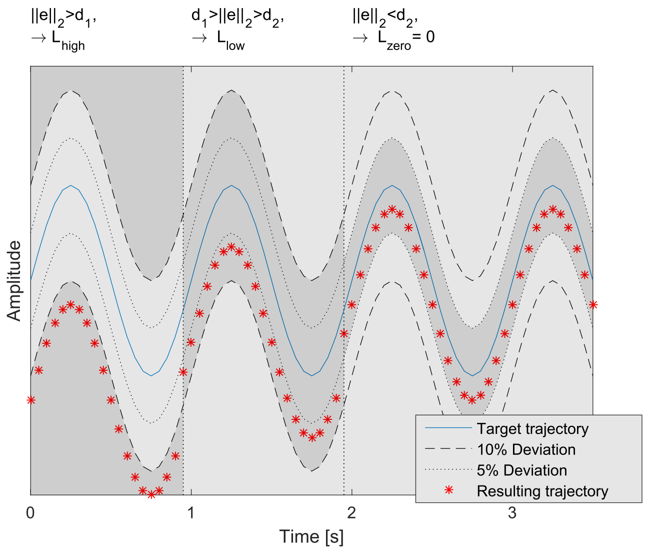

Figure 5.4: An illustration of the gain switching process (not a simulation or experiment result). After correcting below the first threshold $||e||_2$ (a measure closly related to NRMSE), gain is switched to a different value. The convergence continues and gain is switched off as soon as the trajectory is within the target range. Figure taken from [8].

but led to long term stability issues even in simulation. One possible way to deal with this problem and improve performance, both in terms of convergence speed and magnitude of the final control error, is to vary k_p and k_d based on how far convergence has progressed (see Figure 5.4). In the last step both gains are usually set to zero and learning is stopped. This technique is called gain switching.

As a measure for convergence the normalized root mean square error of the previous iteration was used:

$$\text{NRMSE} = \frac{1}{\hat{r}} \sum_{i=1}^{n} r_i - \tilde{y}_i \tag{5.20}$$

with the reference r_i and controlled variable y_i values sampled during one period, and the amplitude of the reference signal $\hat{r}$. For the most successful simulations the parameters are set to $k_p = 1.1$ and $k_d = 50$ initially. After reaching NRMSE $< 10\,\%$ the gain is switched to $k_p = 0.075$ and $k_d = 4$. Finally, when reaching NRMSE $< 5\,\%$ learning is switched off. This approach yields a convergence time of 2.5 s and final NRMSE of 3.8 %.

5.3.2 ILC Implementation on the Three Bar System

Encouraged by the good results of the simulation an implementation of ILC for the three bar system was tested. However, in some regards a different approach was taken compared to the simulation.

For the control of a continuous traveling wave a continuous ILC design is more straightforward than the parametric one used until here. All operators are implemented as digital filters and the memory for keeping the previous iteration control action is a digital delay line. This approach spreads computational load evenly to achieve high sampling rates. Otherwise it does not fundamentally change the control as previously analyzed, since this analysis did not assume a reset at the start of the period or similar conditions unique to batch processes.

Because the overall fit of the greybox model is decent, the first approach tested was inversion based ILC. In inversion based ILC design the learning filter Γ approximates the inverse of the identified model as closely as possible. With such a design convergence could theoretically, in absence of any model mismatch, be reached within one period. However, it is also particularly susceptible to model mismatch [5]. This design failed and uncovered that in some specific frequency ranges the model fails to fit the results. Since these ranges are close to the operating frequency the model does work far worse than suggested by the 80 % overall NRMSE. A convincing reason for this outcome could not be identified. However, sensor inaccuracies were identified as one problem and were later addressed with the 2.1 Upgrade (see Section 4.5).

The fallback solution was a simple P-Type ILC. As in the approach shown in simulation, coupling was treated as disturbance and all three bars were controlled individually by SISO ILCs. A low pass was used as steering filter S. This filter ensures the long term stability whose lack made gain switching mandatory in the simulation studies. Therefore, the focus in this approach is shifted to the design and implementation of the S-filter and adapting ILC for application to the system.

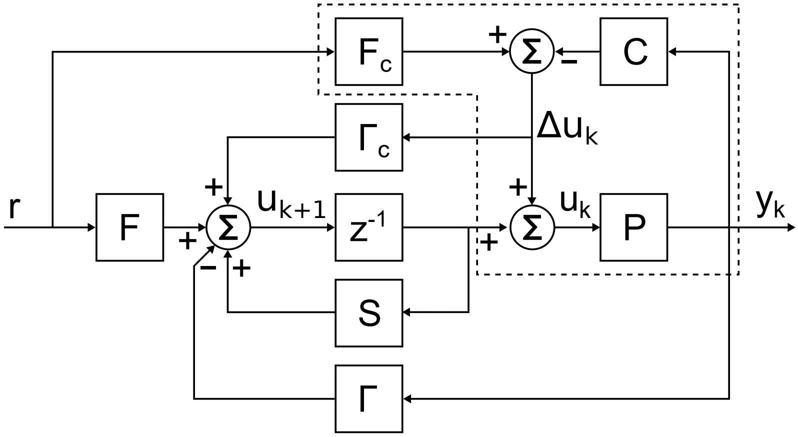

Figure 5.5: Block diagram of a general ILC with underlying classic feedback control.

One such adaptation in practice is that ILC is often combined with classic feedback control, which can be done in series or in parallel. Using it in series, i.e. having ILC control the reference input of a feedback controller, is particularly useful in applications where a system first has to be stabilized by feedback control before applying ILC. Stabilization is not only not necessary here, since the actuator systems are stable, but also a particularly poor option, since PD cannot control the system well (as seen in Section 5.1). Therefore, it is used in parallel, which leads to the ILC with underlying classic feedback control, shown as block diagram in Figure 5.5. A peculiarity of this scheme is the so called current iteration tracking error Δu_k, which is the output of the classic controller fed back into the learning process via the filter Γ_c. The ILC then learns the combined control action, which is applied to the plant as intended, not only what is fed back via S.

Since tests with PID (see Section 5.1) had shown that achieving the proper phase is a major problem when controlling the actuator 2.0 system, a zero phase filtering method was used for the ILC. This method was also

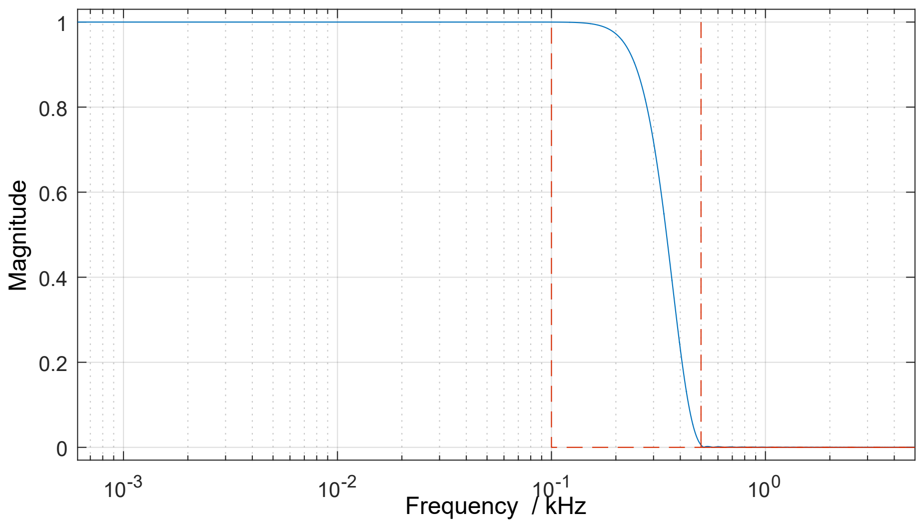

Figure 5.6: Transfer function of the FIR low pass filter used as the steering filter, and as part of the learning filter. Group delay is constant at 50 samples (5 ms).

used in Hard Disk Drive (HDD) head positioning applications, which work with a similar drive mechanism (voice coil) and at similar frequencies (7200 rpm = 180 Hz). It has shown good results for phase tracking in these applications [46]. The method works by using symmetrical Finite Impulse Response (FIR) digital filters which exhibit a constant group delay over their whole transfer function (see Figure 5.6). These filters are used for the learning filter and the steering filter. When this group delay is compensated for by subtracting it from the length of the memory delay line, the filters in the ILC work as if they had zero phase impact. This approach is remarkable as it would normally not be physically realizable (hence they are also called acausal filters).

The design is simplified by choosing $F = \Gamma$ for a set-actual comparison, and analogously $F_c = C$. In addition, $\Gamma_c = \Gamma = \gamma S$ with the real scalar learning gain $\gamma \leq 1$ is used. Since model knowledge is limited, γ is chosen by increasing it to the point where stability is lost over an actuation time of 120 s and then reduced to half that value, inspired by [34]. The condensed block diagram based on these choices is shown in Figure 5.7

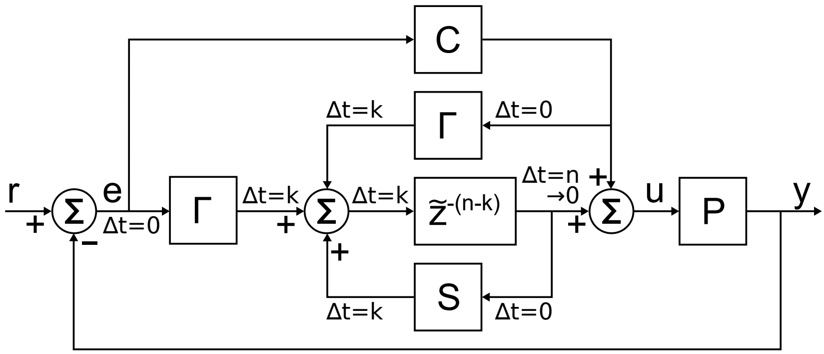

Figure 5.7: Block diagram of a simplified zero phase filtering ILC with underlying classic feedback control. The Symbol $\widetilde{z}^{-(n-k)}$ indicates a delay by $n-k$ sample times as opposed to z^{-1} referring to one full iteration of a length of n samples. The Δt values signify the delay relative to the start of the period and $\Delta t = n \to 0$ marks the point where the period is completed.

with annotations signifying the delay distribution used for zero phase filtering. The group delay of k samples chosen when designing the FIR filters imposes limits on the ILC period length. It cannot be chosen $< k$ since for $n = k$ the delay line would operate at minimum, i.e. zero, delay. For this implementation $k = 50$ was chosen at a sampling rate of $f_s = 10\,\text{kHz}$. Therefore, the minimum period is 5 ms and the maximum frequency 200 Hz, covering the whole target range of 80 Hz to 135 Hz.

The combination of zero-phase ILC with an underlying PD-control resulted in stable wave actuation up to a frequency of 20 Hz on the three bar test system. Very fast convergence in about eight periods (see Figure 5.8) seemed promising. To transition to the larger 20 actuator wind tunnel system, some adjustments had to be made as the larger dimensions of this system pose additional challenges. Furthermore, the large model mismatch preventing inversion based ILC, hindered progress towards the target frequency range, making a different modeling approach and new sensors necessary.

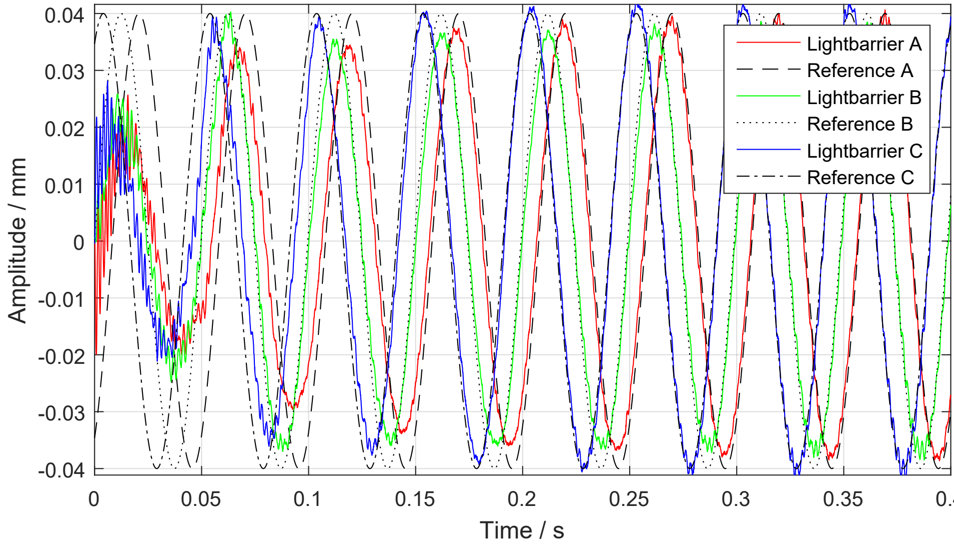

Figure 5.8: Convergence of ILC with underlying PD control at 20.1 Hz. This was measured on the three bar system 2.0 test setup.

5.4 Zero Level Control

Zero level control is designed to overcome two primary disturbances: gravitation and reset force hysteresis. However, when testing individual PI-control, saturation of the control action, i.e. input voltage, on individual bars was often encountered. Possible reasons includes an offset between Lorentz force and reset force which leads to an increase in force not closing the remaining gap between neighboring actuators, but instead producing a torque leading to tilt. To overcome this problem, two approaches were studied: a collective control of the actuators and a control of the individual bars.

5.4.1 Collective Control

The collective control approach uses the fact, that the hysteresis affects all actuators together, as the bars are coupled stronger to each other than to the frame. And since the mass of the bars is very similar, gravitation should be overcome by an evenly distributed force. The problem of saturation is circumvented by averaging and choosing a special controller. The controller is similar to a PI controller but uses a first order low pass filter with high amplification instead of integral action. The corner frequencies are f_{LPI} = 0.1 Hz (low pass) and f_{IP} = 20 Hz (transition to P-control). The error signals of all actuators were summed up, fed to the controller and the output was distributed evenly over all actuators:

$$e = \sum_{i=1}^{N} r_i - z_i \tag{5.21}$$

$$u_{1...N} = u_0 \tag{5.22}$$

This method avoided saturation. As a disadvantage, the actuators did not form a flat surface, but sloped in x-direction. Therefore, a second collective control action was added specifically to overcome this effect. It calculates an average slope from the actuator positions, which is used as error signal and counteracts the slope by applying force increasing linearly from the central (i.e. 10 and 11) to the outermost actuators (i.e. 1 and 20):

$$e = \sum_{i=1}^{N} (r - z_i) \frac{i - N + 1/2}{N} \tag{5.23}$$

$$u_i = u_0 \frac{i - N + 1/2}{N} \tag{5.24}$$

Despite this careful compensation, sloping is still an issue, especially during high amplitude actuation (375 µm amplitude at 108 Hz) as can be seen in Figure 5.9.

5.4.2 Dead Zone PI

The alternative solution is to give the individual actuators some slack by using a normal PI controller with a feedback deadzone. Feedback deadzone

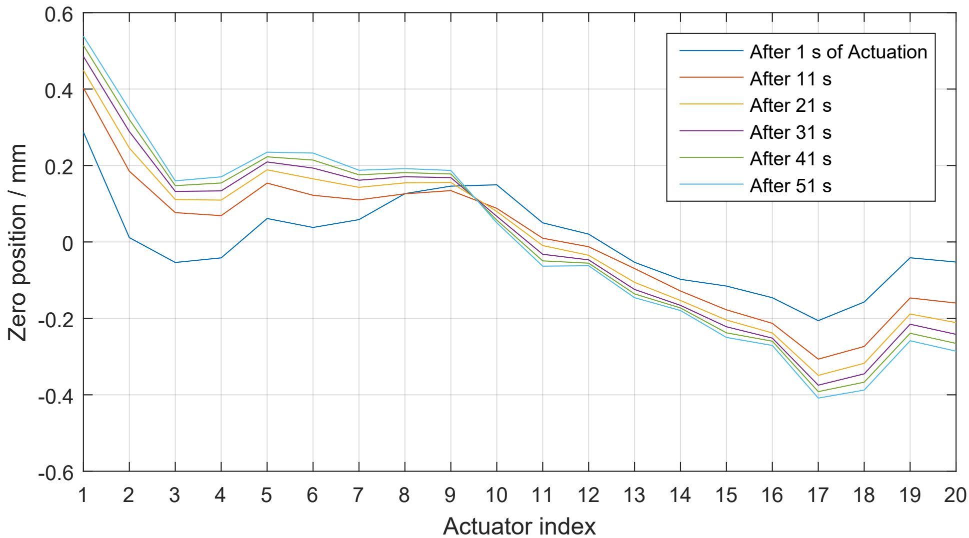

Figure 5.9: Result of zero level control during 375 µm amplitude, 108 Hz wave actuation. The positions plotted in this graph are snapshots of trajectories, which were zero phase filtered with a $f_c = 5\,\text{Hz}$ 6th order low pass filter.

means that if the error is within a certain range ϵ around zero it will be set to zero:

$$e_i = \begin{cases} r_i - y_i & \text{for } |r_i - y_i| > \epsilon \\ 0 & \text{for } |r_i - y_i| \leq \epsilon \end{cases} \tag{5.25}$$

This approach was tested and worked for surprisingly small deadzone values of ±20 µm for all actuators. With this concept, deviations from the zero position of the bars could be reduced to acceptable levels (30 µm typical, 70 µm maximum for 375 µm amplitude wave actuation at 100 Hz in the 2.1 system, see Figure 5.10).

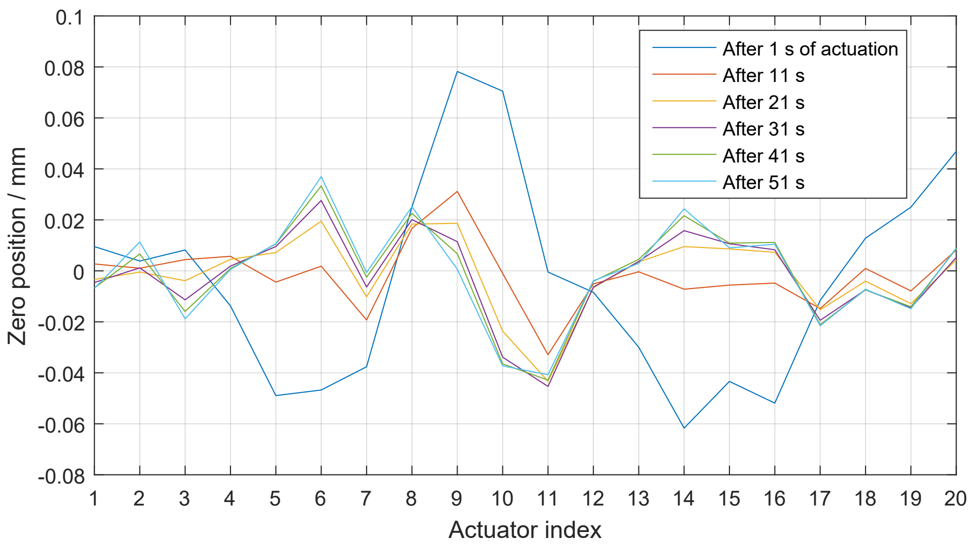

Figure 5.10: The same snapshot technique as used for Figure 5.9 was applied to the deadzone PI zero level control at 375 µm amplitude, 108 Hz wave actuation. The zero level is far more stable and does not tilt to one side. Please note the different scaling compared to Figure 5.9.

5.5 Single Frequency Model

To address the problems revealed by the state space model parameter identification, focus was put on only one specific operating frequency at a time. This approach results in a simpler model consisting only of one matrix with complex coefficients, each of which represents an input-output gain and phase. Besides being simple, this model can also be more accurate compared to the identified state space model for the chosen frequency. This is the case because the state space model fits a certain band of frequencies similarly well, depending on how they might be weighted in the identification process. However, it may then not fit as well for one particular frequency as the static gain-phase matrix where no compromise is made.

The measurements required to find the single frequency model consist of a 2.5 s sine excitation of each individual bar at an amplitude of 15.2 V (approximately 40 % of the maximum amplitude) one after another and separated by a 0.5 s break. This measurement is only possible with some type of zero level offset to move the bars into the calibrated sensor range. The necessary offset can be static or feedback controlled. In the latter case the control should only have weak impact at the target frequency and should be the same as used for zero-level control in the final setup. This approach ensures minimum impact by the zero-level control on the wave control.

The position trajectories of all actuators are measured for the whole excitation process. For the settled portion of the excitation for each actuator the Hilbert transformation $\mathcal{H}$ is used to determine the time average ($\langle\ldots\rangle_t$) instantaneous amplitude $A(z)$ and phase $\phi(z)$ of the plant output:

$$A(z) = \langle |z + i\mathcal{H}(z)| \rangle_t \tag{5.26}$$

$$\phi(z) = \langle \arg\left(z + i\mathcal{H}(z)\right) \rangle_t \tag{5.27}$$

They are referenced to the set and, therefore, known voltage input amplitude and phase to find transfer function gain and phase. They are combined into the complex coefficients of the gain-phase matrix model $\tilde{P}$:

$$\tilde{p}_{j,k} = \frac{A(z_j)}{A(U_k)} \exp\left(i(\phi(U_k) - \phi(z_j))\right) \tag{5.28}$$

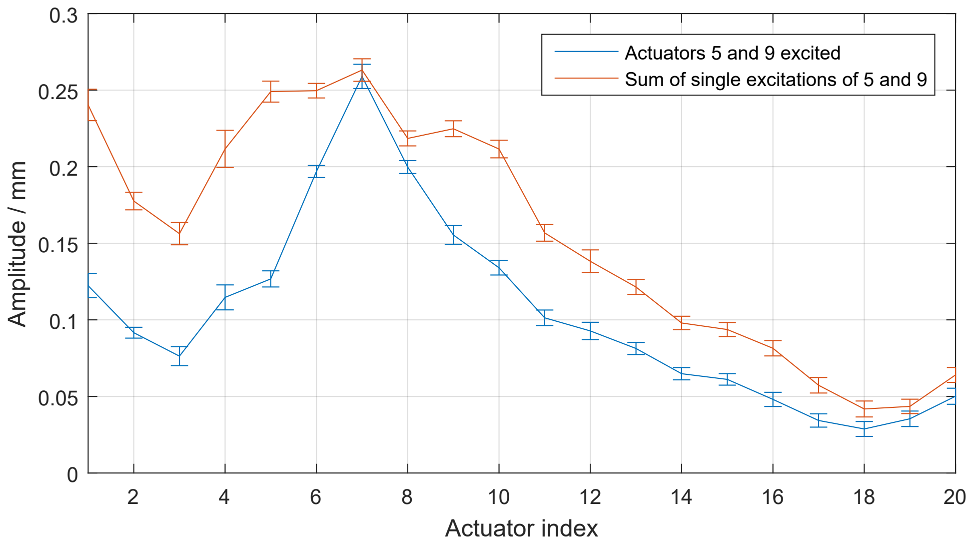

Figure 5.11: Graph comparing one measurement at the same frequency where both were excited in phase with sum of two single bar excitation measurements. The three measurements were taken at 108 Hz. Ideal linearity would mean that the sum is the same as the double excitation.

This technique also allows for a test of linearity of the actuator system using superposition. For this purpose, the sum of two single excitation measurements for two actuator bars within the actuator 2.1 system is compared with the measurement of them being excited at the same time and in phase. The result can be seen in Figure 5.11. The significant difference between the two curves indicates a strong nonlinearity of the system. However, due to the complexity of dealing with the nonlinearity within the control design, the system is treated as linear for the purpose of feedback control.

5.6 Decoupling Steering

Decoupling is of great interest as the bars within the actuator system are strongly mechanically coupled. Complete decoupling is reached, when each actuator bar can be positioned without affecting the other bars. This behavior is achieved by counteracting the movements the coupling would induce in them. There are three common decoupling techniques. Static decoupling by feed forward, dynamic decoupling by feed forward [24, pp. 400 – 405] and state feedback decoupling [12].

Static decoupling is designed for steady state. A gain matrix maps the inputs in such a way that proper counteraction is achieved. This concept still works when the system is not in steady state, but becomes less useful when approaching the slowest system dynamic. The natural extension of this approach is the simplest dynamic decoupling, which uses a complex matrix representing gain and phase at a certain frequency mapping inputs to outputs in much the same way as the static gain matrix. This concept usually has some bandwidth around its target frequency over which it decouples the system sufficiently depending on the requirements of the application and the system, of course.

Augmenting this approach by using low order transfer functions instead of static coefficients in the matrix can extend the bandwidth over which the decoupling works at the cost of increased complexity. These methods typically all rely on computing the inverse of an appropriate system model to find the decoupling matrix. The inverse might not exist or might be unstable or might have other undesirable properties. For most such situations an optimization problem can be formulated and solved to obtain an approximate decoupling, which reduces coupling instead of completely canceling it out [24, pp. 402 – 405]. The third and arguably most computationally costly approach avoids having to invert a system but requires a state space model to implement a state space feedback controller, which is then designed in such a way that it counteracts the coupling.

The simplest approach that could be shown to work was chosen, which is dynamic decoupling for a single frequency with a gain-phase matrix. This matrix was found by inverting the single frequency model described in the previous section. Fortunately it is invertible and the inverse typically

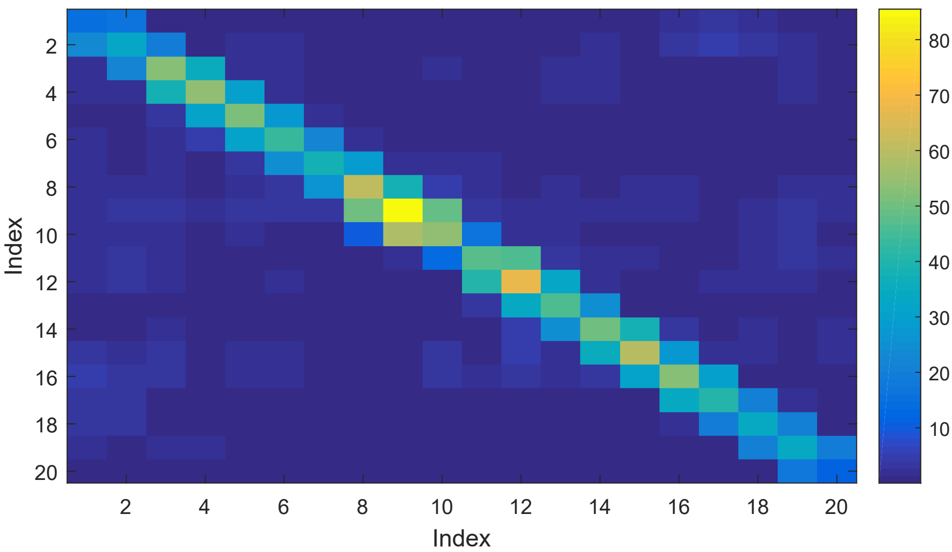

Figure 5.12: A pseudo color representation of the magnitude of the complex matrix coefficients, i.e. the gain.

has its highest gain values on the main diagonal of the matrix and its two neighboring diagonals (see Figure 5.12).

The complex valued matrix has to be implemented in such a way that arbitrary signals can pass through. For this purpose, the complex representation with coefficients $m_{i,j}$ was converted into a combination of gains $\hat{g}_{i,j}$ and delays $\hat{\phi}_{i,j}$:

$$\hat{g}_{i,j} = |m_{i,j}| \tag{5.29}$$

$$\hat{\phi}_{i,j} = \arg(m_{i,j}) \tag{5.30}$$

To each channel N gains are applied and the resulting signals are delayed appropriately. Then the ith signals from each channel are summed up which is functionally the same as a matrix multiplication. The argument function used to determine $\phi_{i,j}$ gives values from $-\pi$ to π. To keep the delays as small as possible and avoid non-realizable negative values, the sign of the gain is used:

$$\hat{\phi}_{i,j} \leq 0 : \phi_{i,j} = \hat{\phi}_{i,j} + \pi \wedge g_{i,j} = -\hat{g}_{i,j} \tag{5.31}$$

$$\hat{\phi}_{i,j} > 0 : \phi_{i,j} = \hat{\phi}_{i,j} \wedge g_{i,j} = \hat{g}_{i,j} \tag{5.32}$$

Then the maximum possible delay is half of one period of the target frequency of the decoupling. The accuracy of this implementation is improved further by using a fractional delay line (Matlab DSP Toolbox) instead of an integer delay line. It uses linear interpolation to realize delays which are not integer multiples of the sampling time.

The sum of row entry magnitudes for the inverse matrix generally does not have the same sign as the main diagonal element. This problem leads to instability at steady state since the sign of the feedback is flipped for the sum of forces, which is the relevant property for steady state, compared to the main diagonal, i.e. the off diagonal elements overpowering the main diagonal one. Note that this observation is just a convenient clue. The phase mismatch could also rise to an unacceptable level at any frequency in between the target frequency and steady state, causing instability. Therefore, using only non-negative gains and larger delays would, in general and in the case of our system, not avoid this problem. Instead the problem is circumvented by separating zero-level and wave control in frequency, with decoupling only being part of the wave control.

An example for the quality of the feed forward decoupling is shown in Figure 5.13. It was measured by exciting one bar and comparing the resulting amplitudes to the ones seen when the other bars are held in place by the feed forward decoupling. The figure of merit defined for this purpose is the total off-diagonal suppression ratio for the kth actuator bar:

$$\alpha_k = \frac{\sum_{i \neq k} \bar{D}_i}{\sum_{i \neq k} \bar{A}_i} \tag{5.33}$$

with the amplitudes of the ith actuator $\bar{A}_i$ before and $\bar{D}_i$ after applying the feed forward decoupling, normalized to the respective amplitudes of the kth actuator before and after. The measurement shown in Figure 5.13

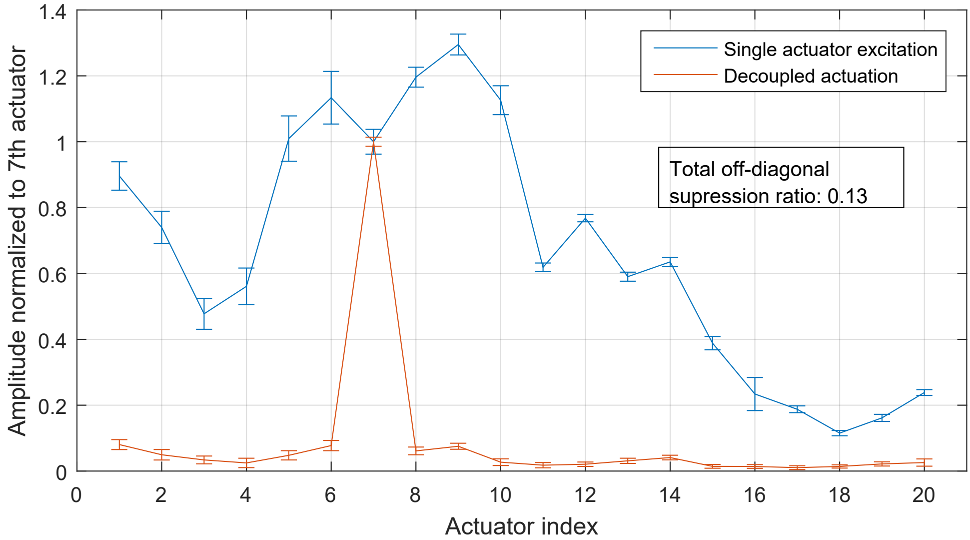

Figure 5.13: Comparison of actuator amplitudes before and after feed forward decoupling. Error bars signify the temporal standard deviation of the instantaneous amplitude. The amplitudes are normalized to the amplitude of the seventh actuator in the respective measurement to make the comparison as clear as possible. The amplitudes with decoupling are much smaller (7th bar at 50 µm) than without it (7th bar at 115 µm).

found $\alpha_7 = 0.13$. Similar measurements determined the average over all actuators for 80 Hz to be $\langle\alpha\rangle_k = 0.21$ and for 108 Hz $\langle\alpha\rangle_k = 0.23$.

5.7 Final Control Design

Based on the realized decoupling scheme, the final control design is split into two different feedback loops acting on different frequency bands: The zero level control on the one hand acting at steady state to keep the zero position, around which each bar oscillates, and the wave control on the other hand acting at the target frequency [40].

The action of the zero level control at the target frequencies of the wave control was tuned to be as small as possible, while still providing stable zero level control. As previously outlined (Section 5.3), wave control is provided by SISO ILCs acting on each bar individually. In contrast to what has been described in Section 5.3, the SISO ILCs now act on the decoupled system. This technique makes it more plausible to assume that the remaining coupling can be treated as disturbance. The final success of the method suggests that decoupling is, indeed, the key improvement.

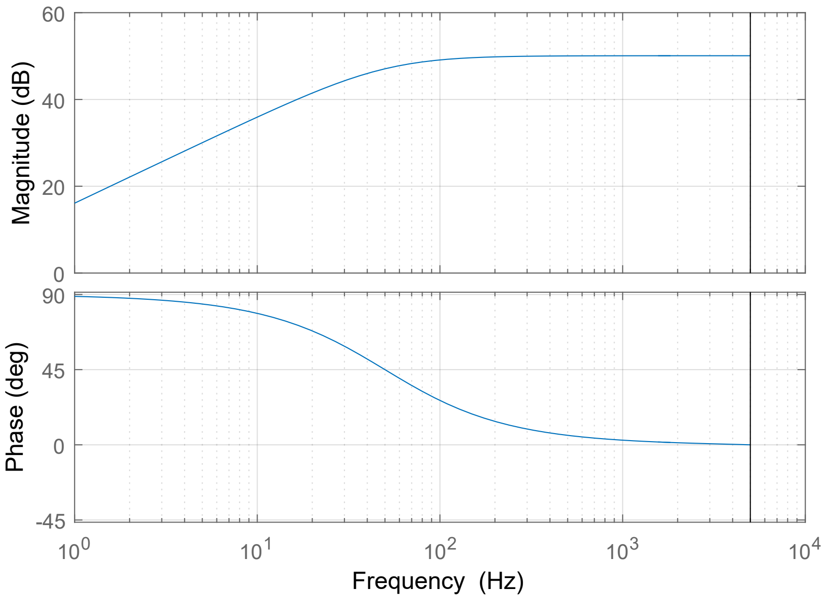

Figure 5.14: Transfer function of the IIR high pass filter used in the learning filter.

To achieve the frequency separation, control action of the ILC on the steady state is suppressed by using a high pass filter as part of the learning filter. The first order high pass filter is implemented as infinite impulse response (IIR) filter with half power frequency $f_c = 50Hz$ (Figure 5.14). Due to this separation of frequencies, the current iteration tracking error feedback is omitted, and the corresponding block diagram is shown in Figure 5.15.

To retain the effect of zero phase filtering after adding the decoupling

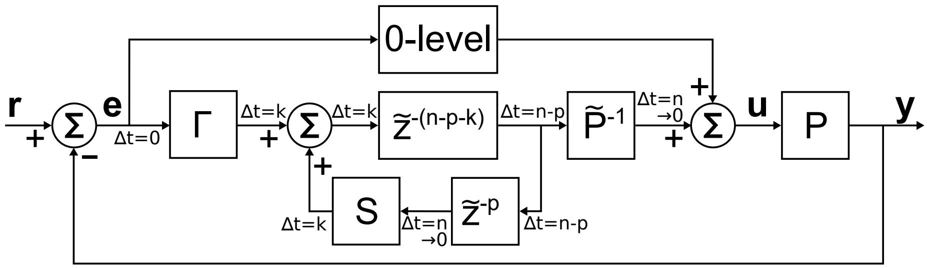

Figure 5.15: Block diagram of the zero phase ILC with decoupling and frequency separated classic feedback control. The Symbol $\tilde{z}^{-(n-p-k)}$ indicates a delay by $n-p-k$ sample times as opposed to z^{-1} referring to one full iteration of a length of n samples. The Δt values signify the delay relative to the start of the period and $\Delta t = n \to 0$ marks the point where the period is completed.

behind the ILCs, its impact on phase has to be compensated. For this purpose, the delay length is further reduced, compensating for the minimum main diagonal delay in the decoupling matrix, while keeping the total delay in the delay line S filter loop at exactly one period. The Δt annotations shown in Figure 5.15 depict how the delays match up.

The learning gain γ used in the learning filter needed to be reduced compared to the ILC implementation for the test system. It depends on the attainable quality of decoupling at the target frequency and typically lies in the range of 0.005 to 0.01. With all of these settings, the final design proves to be successful for fixed wave parameter settings.

Parameter Transitions

Algorithms for smooth phase transitions for steering of the actuator system 1.0 have been developed during the first funding period of FOR 1779. A change in instantaneous frequency is used to shift the phase within less than one period without producing significant kinks in the reference trajectory, avoiding the generation of high frequency components in the reference [51].

However, the very low learning gain of the design described above acts in a similar way and smooths out even step transitions between different amplitudes or different wavelengths (i.e. phase shifts) over multiple periods (see Section 6.1.1). These transitions leave the length of the ILC period intact and, therefore, do not require implementation of additional algorithms.

In contrast, a frequency change would require changing the ILC period. This major difference makes a step change in frequency a difficult challenge. This challenge has not been tackled yet. A straightforward approach would be to compress or stretch the next iteration control action in parallel with the ILC period. Due to the low learning gain this adaptation would have to be executed slowly over multiple periods. Further research on this topic is necessary to prove the applicability of this approach.

5.8 Summary

First tests on the three bar system 2.0 with classic PD control have shown that feedback control in general is viable for the system. To improve over it, a state space model for model based multiple input multiple output control has been identified. In addition, it has been determined from the periodicity of the reference and the expected disturbances and through simulation that Iterative Learning Control (ILC) fits the requirements of wave actuation well. Shortcomings in the state space model and the known issues of the version 2.0 system (see Chapter 4) prevented inversion ILC. However, zero-phase filtering P-Type ILC with an appropriate steering filter and underlying PD control resulted in fast convergence at 20 Hz.

The 20 actuator system 2.1 has been used for the further control design. A model for just one frequency, i.e. the intended actuation frequency, has been determined in shape of a complex valued matrix. Using the inverse of this model for feed forward, decoupling has been combined with SISO ILCs, which have been implemented as developed on the test system. Separating this combination for wave control from zero level control finally yielded a successful overall control. The verification of this control design is described in the next chapter.

6 Verification of System 2.1

The goal when developing the actuator system 2.1 and its control covered in the previous chapter has been to provide new options with regards to parameter sets and flexibility to the researchers applying the system. The achievable parameter sets can be evaluated at the normal system test stand (see Figure 3.1). The dual light barriers (see Section 4.2) are used to determine the tracking quality. After achieving parameter sets within the target ranges on the test stand, including wave quality, system verification was finalized in the wind tunnel at the AIA. Operation under typical conditions there was tested and micro particle tracking velocimetry (micro PTV) measurements were performed to determine drag reduction values at these parameters. They are compared to the values reached for similar parameter sets by the system 1.0. After that issues of implementation of the verification measurements are discussed, concluding the chapter.

6.1 Reference Tracking Tests

The wave control outlined in the previous chapter (Chapter 5) was continually tested on the actuator system during its development. To determine the performance, the in-loop light barrier sensors were used exclusively. Best practice would be the use of out of loop sensors, e.g. the reference sensors. Unfortunately, this best practice was not possible due to the high number of actuators and their tight spacing. However, when testing single bars with light barriers as well as the reference sensors, deviations are reliably so small that they are of no concern. The deviation is typically 3 % of the target amplitude range. All following test stand verification measurements were performed in accordance with ISO 9001:2015.

The first verification issue is to evaluate the maximum amplitude, which can be reached at a given frequency. Actuation needs to comply with the current limit of 1.77 A described in Section 2.2. By observing input voltage, which roughly corresponds to input current, while increasing the reference amplitude from run to run the maximum amplitude to be reached was identified (see Table 6.1).

The second verification issue is wave quality. For a quantitative description the deviation Δ_A of the mean wave amplitude, the unevenness μ_A and the maximum normalized temporal standard deviation $\hat{\sigma}_{t,A}$ are defined as described in Section 1.2. A systematically lower average amplitude than the reference had been observed previously. To alleviate this issue, a pre-calibration was performed by doing a test run at 100 µm to find the ratio of reference amplitude to average amplitude reached with each set of parameters (frequency, decoupling etc.). The desired amplitudes were divided by this ratio to match the target amplitude better than 2 % as indicated by Δ_A in Table 6.1 (note that this pre-calibration was omitted at 108 Hz). Unevenness μ_A is much smaller than the required limit for all measurements, while $\hat{\sigma}_{t,A}$ has values close to the limit (see Table 6.1).

Table 6.1: Wave parameters reached by the controlled 20 actuator system 2.1 and target ranges for frequency f, wavelength λ and maximum Amplitude A_{max}. It also contains the deviation Δ_A of the mean wave amplitude, the unevenness μ_A and the maximum normalized temporal standard deviation $\hat{\sigma}_{t,A}$ as described in Section 1.2. The measurement taken at 108 Hz was not pre-calibrated.

Type	f **/ Hz**	λ **/ mm**	A_{max} **/ µm**	Δ_A	μ_A	$\hat{\sigma}_{t,A}$
Target	80 to 135	80 to 160	260 to 500	<10 %	<10 %	<10 %
Tested	81	160	315	1.6 %	2.0 %	9.3 %
	100	160	375	0.2 %	0.3 %	9.4 %
	108	160	315	7.0 %	0.7 %	7.8 %

6.1.1 Parameter Transition

The final important goal to be illuminated here is the ability to change the wave parameters online (parameter transition). Due to the concept of ILC being focused on a fixed frequency (see Section 5.7) a change of frequency was not attempted. Amplitude and phase parameter (i.e. wavelength) changes were tested as step reference changes. This test was conducted at 100 Hz. The starting parameters were 50 µm amplitude and a wavelength of 200 mm corresponding to a phase shift of −18° between the central actuators.

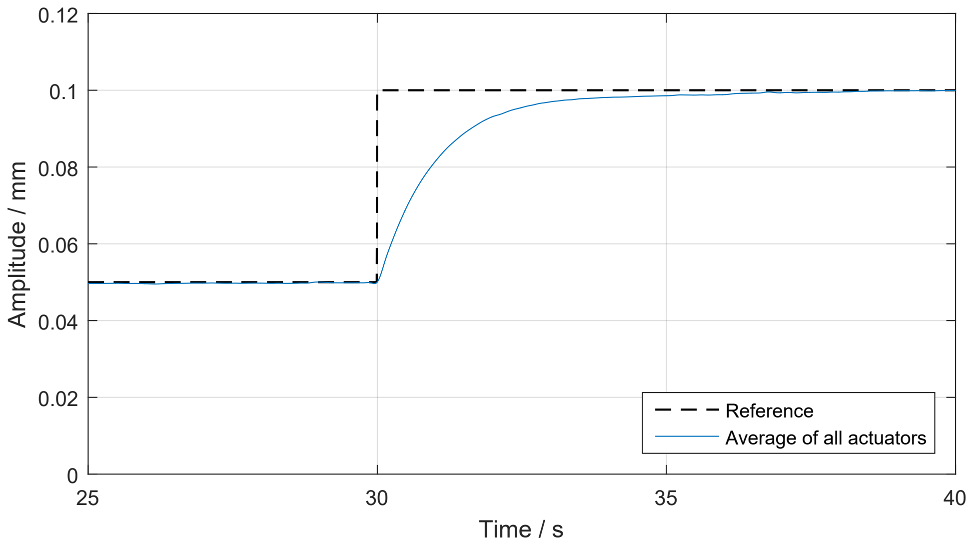

Figure 6.1: Filtered average of the responses to a step in reference amplitude from 50 µm to 100 µm.

For the amplitude test a step of the reference amplitude to 100 µm was performed at the 30 s mark. To remove noise and offsets, the data were first zero-phase filtered (matlab filtfilt) with a 6th order high pass $f_c = 5\,\mathrm{Hz}$, then with a 6th order low pass $f_c = 200\,\mathrm{Hz}$. The result was Hilbert transformed to find the analytic signal from which the instantaneous amplitudes were extracted. These were low pass filtered again with a 6th order low pass $f_c = 5\,\mathrm{Hz}$. The resulting signals were averaged and this average is shown in Figure 6.1. The time from 10 % to 90 % of the step change is approximately 3 s.

For the phase test a step of the reference phase shift from −18° to −22.5° (equivalent to a step in wavelength from 200 mm to 160 mm) was performed at the 30 s mark. Here all bars with ideal traveling wave phase shifts (4

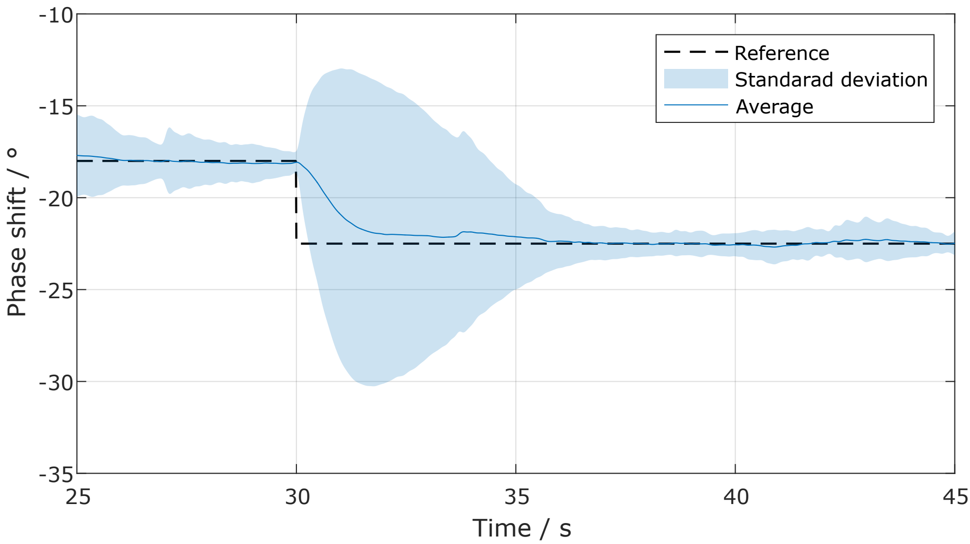

Figure 6.2: Filtered average phase shift between the actuator bars 4 to 17, which are the shifts 4 to 16. Reference phase difference is stepped from −18° to −22.5°.

to 17) were evaluated. The same filtering as for Figure 6.1 was used. In the case of the amplitude step response all amplitudes behaved similarly, making the average instantaneous amplitude a good indicator for the overall step response. In the case of the phase difference step response, the average is not a good indicator. To remedy this problem, the standard deviation of phase differences between the central actuator bars is also shown and used as an indicator of convergence (see Figure 6.2). It takes approximately 7 s for the deviation to reduce to previous levels, indicating that only then the phase shift is converged.

As these tests proved, actuator system 2.1 achieves parameter sets that can be studied in wind tunnel experiments. The results of the verification proved the control design for the actuator system 2.1 fulfills the requirements concerning wavelength (down to 160 mm), wave quality (deviations below 10 %), and wave frequency (up to 108 Hz). The maximum amplitude to be reached is restricted to 375 µm, which is below the specification of 1000 µm. A design of a new actuator system overcoming this restriction is discussed in Chapter 7. The aim of the actuator system 2.1 is to study the effect of traveling waves on the turbulent boundary layer with special focus on drag reduction in wind tunnel experiments. The following section will describe the verification testing of the system in the wind tunnel.

6.2 Wind Tunnel Performance Test

After studying the tracking performance at the test stand, the actuator system needs to be examined at the location and under the conditions of its final application: the wind tunnel. In addition, these tests will be used to compare measurements taken with systems 1.0 and 2.1 at similar parameter sets and at sets which only one of the two has reached. But first, the setup for this experiment will be described.

6.2.1 Wind Tunnel Setup

For the experiments at the AIA a low-speed Göttingen-type wind tunnel is used. The test section of the wind tunnel is open, 1.8 m long and has a 1.2 m $\times$ 1.2 m cross section. With a 100 kW electric motor driving a single stage axial blower, wind speeds of up to 60 m/s can be reached while the test section is empty. The streamwise turbulence level is less than 0.3 % of the freestream velocity. A feedback flow control system is used to keep the freestream velocity steady such that variations are within $\pm$0.05 %.

An overview of the test section is given by Figure 6.3. The carefully flattened and smoothed white plate (1) frames the actuator system. It is 20 mm thick, 1750 mm long and 1200 mm wide. Its inclination is adjustable to within $\pm$0.15°. The leading edge has a 3:1 half elliptical shape. This construction makes sure the airflow (in arrow direction) over the actuator is well defined. Optical elements (2) guide the Laser light to the measurement location and modify the beam geometry into a vertical light sheet. At the measurement location a camera with a long working distance microscope as objective (3) takes 10 double pictures per second. On these pictures droplets injected upstream (4) are visible illuminated by the laser light. The laser is pulsed so the position of the droplets between the first and second frame in the double pictures shifts according to its velocity. The time difference between the pulses is only so long (on the order of 10 µs)

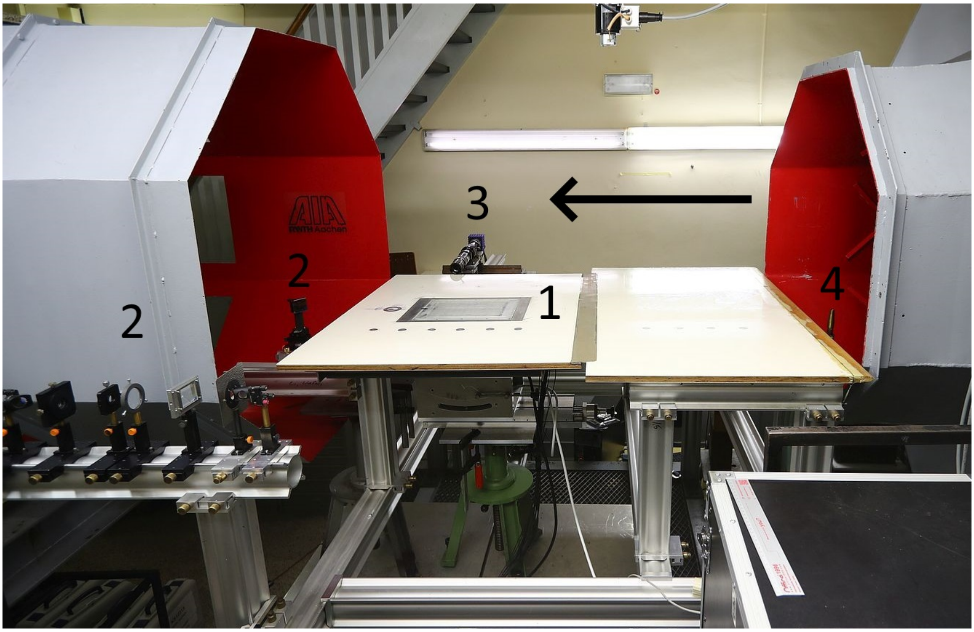

Figure 6.3: Overview of the wind tunnel setup with the flat plate and the actuator (1), laser light sheet optics (2), long working distance microscope and camera (3), and seeding inlet nozzle (4).

that a computer algorithm can calculate the velocities of individual droplets from the shifts and, thus, the velocity of the air they are suspended in. This technique is a called Micro Particle Tracking Velocimetry (μ-PTV, for further details see [23]).

Figure 6.4 gives a closer look at the top of the actuator system 2.1 in the wind tunnel. From the left laser light irradiates the injected particles in and is captured by the camera (1). The location of the measurement is directly above the encircled black (for reduced reflection) surface (2). The direction of wave propagation is indicated by the black arrow (3) while the direction of incoming airflow is indicated by the blue arrow (4). The small gap between the actuator surface and the surrounding aluminum frame is covered with thin transparent sticky tape to avoid disturbing the airflow. The gap is necessary to prevent vibrations from being transferred from the actuator to the large plate disturbing the measurement.

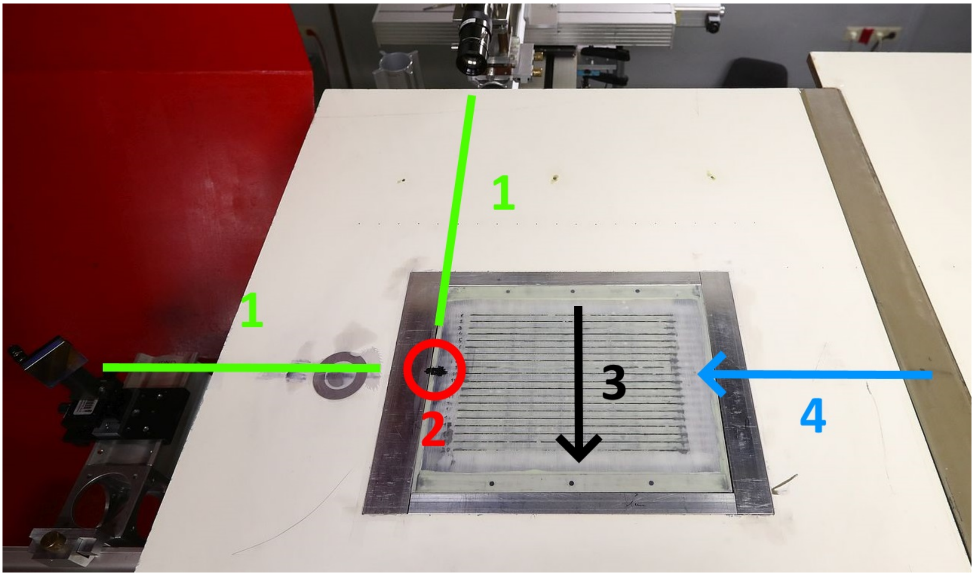

Figure 6.4: The surface of actuator 2.1 integrated into a larger plate over which air flows during the experiments.

The actuator mounting has to ensure the frame onto which the surface is glued is well aligned with the surrounding plate. In Figure 6.5 this mounting is depicted. A tripod for coarse hight adjustment (1) is the base of the construction. On top are a rocker (2) to adjust angle of attack, while the up- or downstream position is adjusted using a translation stage (4) under the rocker. The actuator bars are screwed to the top of the rocker and fine adjustments in relative height for the four legs are made using washers (3). The cables connecting the actuator are also visible. There are 20 Lemo cables transferring power to the actuator bars (5), a 68 pin SCSI (Small Computer System Interface) cable (6) carrying the sensor measurements and a custom cable with molex-plug supplying power to the sensors (7).

With this setup measurements of the drag reduction due to transversal surface waves generated by the actuator system 2.1 were taken under the lead of Wenfeng Li, collaborating scientist within FOR 1779.

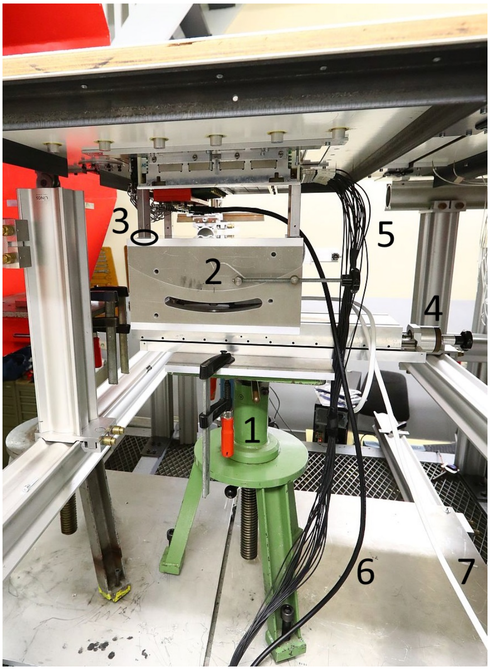

Figure 6.5: Mounting of actuator system 2.1.

6.2.2 Results of the Measurements

The micro PTV measurements were taken in two sets: one at a free stream velocity of 8 m/s and 81 Hz, the other at 6 m/s and 100 Hz (see Table 6.2). The constant velocity gradient ($\frac{du}{dz}$) in the viscous sublayer close to the wall is measured. Friction drag indicated by the wall shear stress τ_w, is directly related to this gradient via the dynamic viscosity μ:

$$\tau_w = \mu \left.\frac{\partial u}{\partial z}\right|_{z=0} \approx \mu \left.\frac{du}{dz}\right|_{z=0} \tag{6.1}$$

From the wall shear stress and the density of air ρ in the wind tunnel the skin friction coefficient is calculated:

$$c_f = 2\rho u_\infty^2 \tau_w \tag{6.2}$$

The drag reduction DR is given by the actuated $c_{f,a}$ and non-actuated $c_{f,na}$ friction coefficient as (see [36]):

$$\mathrm{DR} = \left(1 - \frac{c_{f,a}}{c_{f,na}}\right) \cdot 100\,\% \tag{6.3}$$

The goal of the first set of measurements was to provide a basis for a comparison with the older actuator system 1.0. The second set was taken to demonstrate the effect of the increased wave frequency made possible by the actuator system 2.1.

Table 6.2: Results of the measurements conducted with the actuator system 2.1 and some measurements with system 1.0 at similar conditions (freestream velocity u_∞, frequency f and amplitude A). It also shows velocity gradient $\frac{du}{dz}$ and drag reduction (DR). Data and results kindly provided by W. Li, see also [23].

Version	u_∞ / m/s	Re_θ	f / Hz	A / µm	$\frac{du}{dz}$ / s^{-1}	DR / %
1.0	8	1200	81	0	7629	-
				260	7519	1.4
				315	7421	2.7
				375	7429	2.6
				500	7253	4.9
2.1	8	1830	81	0	10199	-
				200	9993	2.0
				315	9943	2.5
	6	1450	100	0	5911	-
				315	5745	2.8
				375	5700	3.6

For the sake of comparability, measurements with the same surface plate were taken. However, when the measurements with the actuator system 1.0 were taken additional experiment devices were placed in the airstream (e.g. a bypass with a flap for changing inflow conditions). Therefore, the conditions were not exactly the same as with the system 2.1, which leads to the higher velocity gradient in the viscous sublayer. The Reynolds number based on momentum thickness Re_θ can be estimated for the experiments with system 2.1 from the freestream velocity u_∞, the distance from the upstream edge of the plate L and the kinematic viscosity ν of air [39]:

$$Re_\theta = 0.036 \cdot \left(\frac{u_\infty L}{\nu}\right)^{0.8} \tag{6.4}$$

The kinematic viscosity $\nu = 1.5 \times 10^{-5}\,\mathrm{m^2/s}$ at 20 °C and normal pressure was used. Although the Reynolds numbers differ significantly, the similarity of other parameters like the friction velocity at the location of measurement suggest that the measurements of both systems at 8 m/s should be comparable [internal communication].

Due to the thermal limitations discussed before (see Section 4.4), amplitudes were limited to a maximum of 375 µm with actuator system 2.1. At the same time, the control allows for the use of significantly higher frequencies than with actuator system 1.0. Control also makes sure that the zero level is held with high accuracy during the reference measurement (no actuation) as described above.

The estimated error for this drag reduction measurement is usually below ±1 % (see [23]). The measurements of the first set agree with the measurements taken with the actuator system 1.0 at the respective parameter sets within the estimated error. This confirms that the actuator system 2.1 is an adequate replacement for the system 1.0. However, system 2.1 can not only replace the previous system. Though the measurements are not yet exceeding error margins, higher frequency actuation made possible with system 2.1 seems to provide more drag reduction at the same amplitudes.

6.3 Implementation Requirement Fulfillment

In the following, additional details on the methods for reaching the parameter sets given in the verification measurements are described. For this purpose special wave snapshots are shown (Figures 6.6, 6.7 and 6.8). These snapshots cover five periods and show the spatial and temporal properties of the wave at a glance. The oscillation in time direction is depicted by the changing pseudocolor in each horizontal stripe. The spatial progression of the wave, i.e. how it travels from one end of the system to the other, can be observed by following a point of constant phase. For example the crest may move to the right with increasing index number (from top to bottom of the plot). This corresponds to the crest moving to higher indices with increasing time (left to right) and, thus, moving from bar 1 towards bar 20. This line being straight indicates constant phase velocity and, in conjunction with sine shape in temporal and spatial direction, indicates an ideal traveling wave (see Figure 6.7).

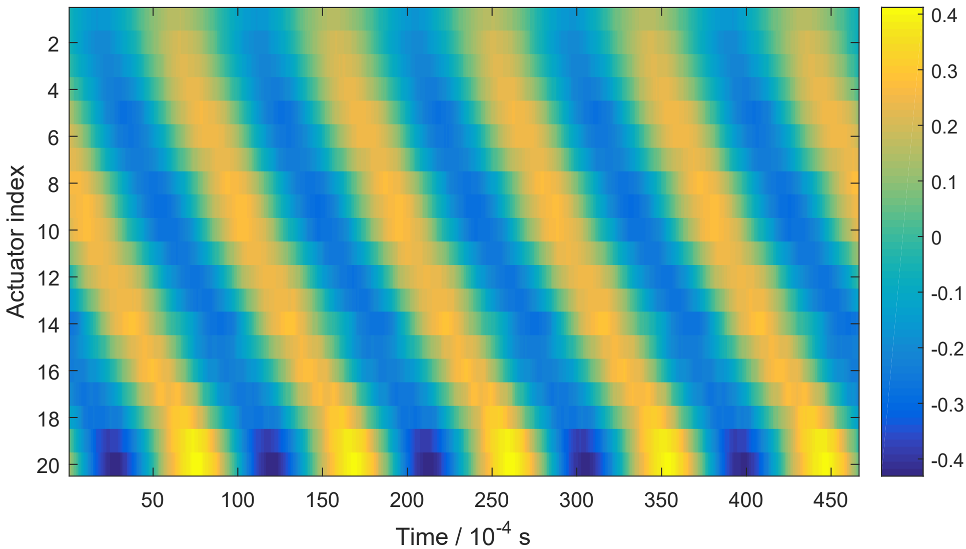

Figure 6.6: Pseudocolor wave image. The offsets of the zero position have been removed by averaging and subtracting them. This graph shows the wave propagation after one workday of manual tuning of actuator system 2.1. The goals of the tuning were 108 Hz frequency, 160 mm wavelength and 260 µm Amplitude.

An ideal traveling wave as reference was not well suited for high amplitudes. Some actuators were placed under higher than average loads, which limited the maximum amplitude. However, the different behavior of the outer boundary actuator bars already became obvious, when the system was manually calibrated without control. It was observed that phase shifts

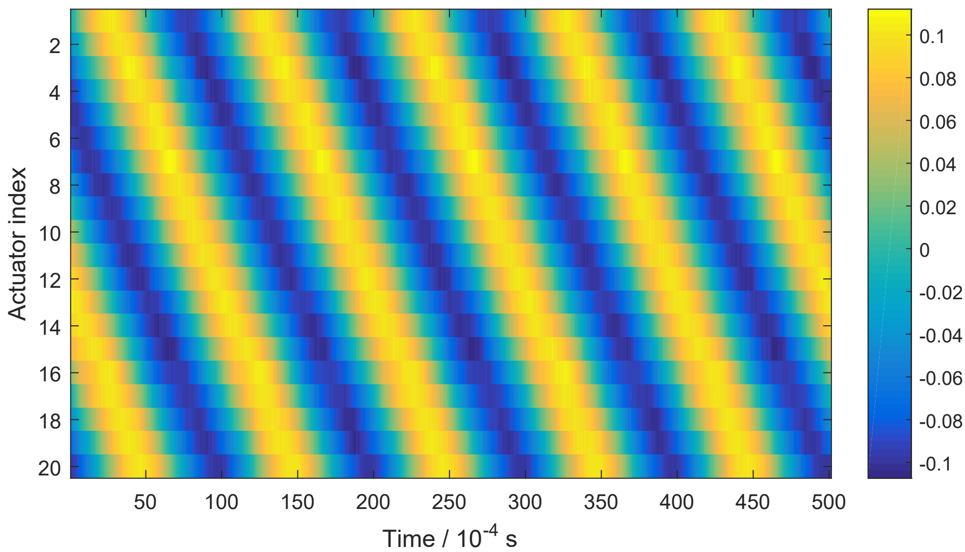

Figure 6.7: Pseudocolor representation of an ideal traveling wave produced with linear phase shift reference by the ILC-controlled actuator system 2.1. The wave parameters are: 100 Hz frequency, 160 mm wavelength, 100 µm amplitude. Zero level offsets have been removed by subtracting averages to improve clarity.

between actuator bars close to the boundaries (e.g. bars 1 to 5) become smaller than the ideal traveling wave would prescribe, despite the input voltages having a constant phase shift between the neighboring actuators (see Figure 6.6). According to the collaborating researchers using the device for wind tunnel experiments, a concentration on the 10 inner actuators 6 to 15 is sufficient to analyze the effect of the traveling waves on the turbulent boundary layer. In line with this idea, the reference trajectories were adapted, for the actuators 1 to 5 and 16 to 20 to follow similar trajectories as they had followed in the manually adjusted case. This change indeed lowered the required input voltage on the bars which were previously reaching thermal limitations. Then voltage could be increased overall, and amplitudes within the desired parameter range were achieved. The comparison between Figures 6.7 and 6.8 shows the result of this approach.

In some cases, it was also beneficial for voltage requirements and stability

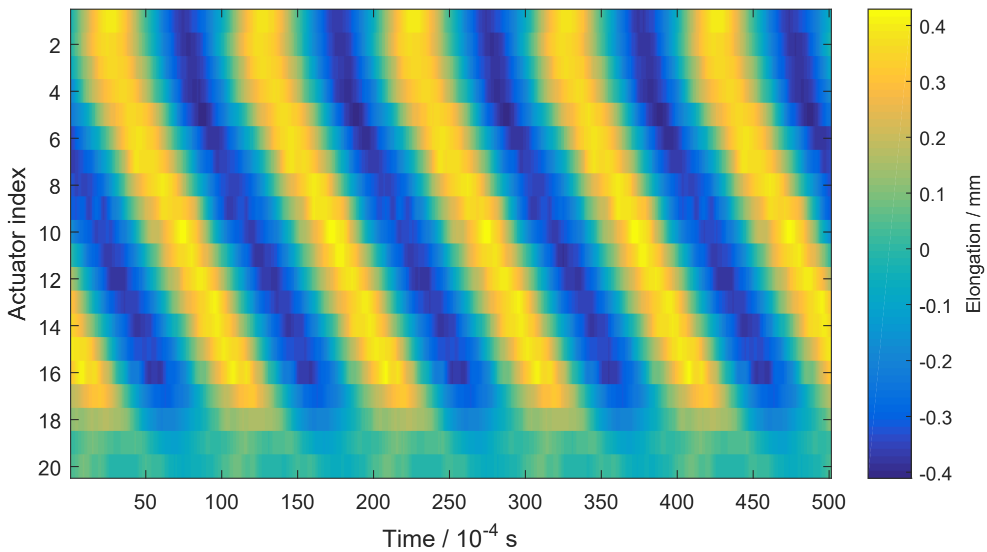

Figure 6.8: Pseudocolor representation of an adjusted traveling wave on actuator system 2.1. The phase shift towards the edges was reduced and the amplitude of the end-actuators decreased. The wave parameters are: 100 Hz frequency, 160 mm wavelength, 375 µm amplitude thus reaching a parameter set well within the target ranges (see Table 6.1). Zero level offsets have been removed by subtracting averages to improve clarity.

to reduce the reference amplitude of the actuators which are situated at the boundary towards which the wave travels. They have to dissipate the mechanical energy of the traveling wave. Otherwise it would be reflected at the almost open end of the actuator boundary, where the last actuator is only loosely coupled to the frame ($\frac{1}{16}$ of the next neighbor spring constant). This reflection would lead to a standing instead of a traveling wave. By reducing the reference amplitude the power available for this task can be increased, but the advantage gained by this adaptation is highly dependent on the circumstances and by far not as reliable a method to improve amplitude as adapting the phase shift.

For a more detailed look and graphical representation of unevenness and temporal deviation in the measurement also shown in Figure 6.8 see Figure 6.9.

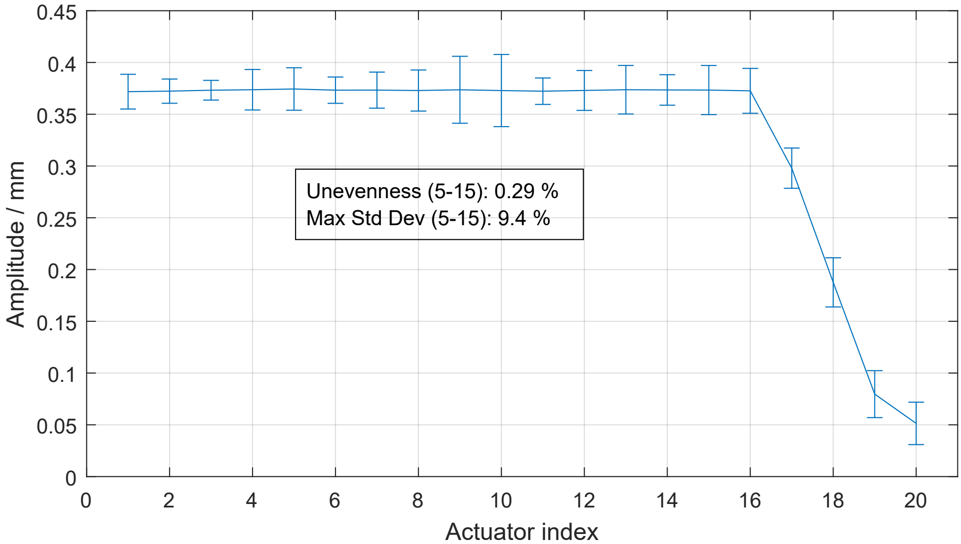

Figure 6.9: Plot of average instantaneous amplitudes and temporal standard deviation of instantaneous amplitudes from the same data as shown in Figure 6.8.

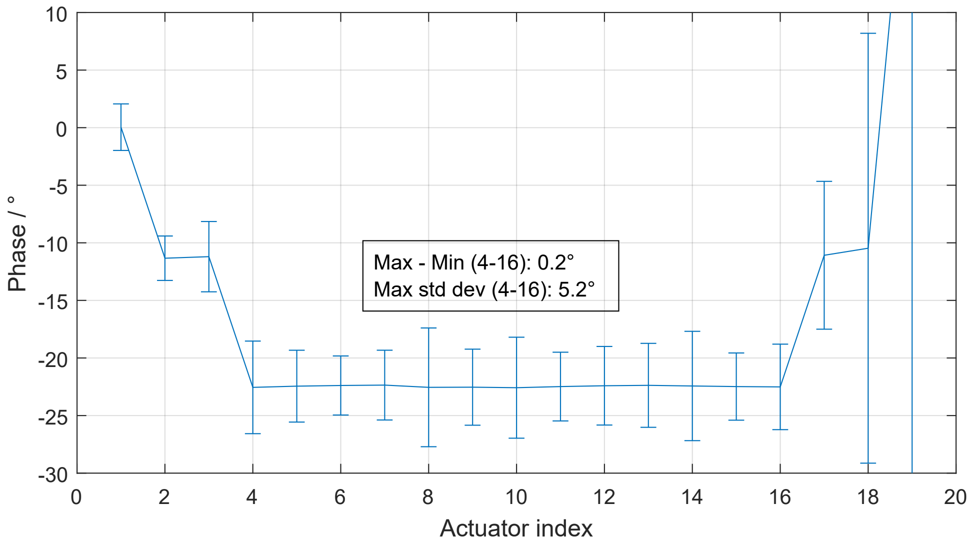

Figure 6.10: Plot of average instantaneous phase differences and temporal standard deviation of instantaneous phase differences from the same data as shown in Figure 6.8.

Phase quality was also evaluated. Figure 6.10 depicts the same measurement as Figure 6.9, processed to show how accurately phase was matched. The phase shift unevenness μ_ϕ is 0.2° and the temporal deviation $\hat{\sigma}_{t,\phi}$ lies at 5.2°.

6.4 Summary

The test stand verification of the reference tracking achieved by the control design proved the system to achieve amplitudes of 315 µm for a frequency range of 81 Hz to 108 Hz. These sets are within the target parameter range. The quality goals are fulfilled, reaching excellent values for unevenness of amplitude and phase, while especially the deviation of the instantaneous amplitude over time is uncomfortably close to the minimum goal of $<$10 %.

The capability to change amplitude and wave length was also demonstrated. Steps in amplitude and phase were realized with convergence times of 3 s and 7 s respectively. Frequency changes were not realized due to the unique challenges they present.

The system was integrated into a wind tunnel setup capable of μ-PTV and PIV (Particle Image Velocimetry) measurements. For the purposes of the studies shown here only μ-PTV measurements were conducted. Though conditions for measurements with the system 1.0 were not exactly reproduced, the results regarding drag reduction show very similar values and behaviors within the given error margins. Additionally, the capability of the system 2.1 to provide wave frequencies up to 100 Hz could be demonstrated in the wind tunnel to further increase drag reduction, although these first results are within the error margins of the drag reduction measurement.

All measurements shown here and also the ones published previously (in [36] [23]) suggest that the effect of the drag reduction will be more pronounced at higher amplitudes, all other parameters being the same. This observation underlines how important it is to overcome the thermal limitations. To solve this issue, a completely new Lorentz force based actuator system has been developed, which will be described in the next chapter.

7 Actuator System 3.x Development

The actuator system 2.1 reaches only parts of the target parameter space. Particularly, the amplitude is much below and the maximum frequency is below the requirements. The reason for this weakness is the limitation of the maximum Lorentz force due to the thermal restriction of the actuator coils. Therefore, a new actuator system 3.x is developed with focus on a significant increase of this force. This chapter describes the development started by first drafting an improved system using some rough estimates, refining this draft by numerical finite element simulations and finally building prototypes to verify the envisioned capabilities. These capabilities not only include increased amplitude, but also two ways to handle the y-tilting, which was a drawback of system 2.1. The chapter concludes with an outlook on further developments leading from the prototypes described here towards a full-scale system for wind tunnel applications.

7.1 Actuator 3.x Concept

Table 7.1: This table contains some examples of necessary accelerations for sine oscillations at the given conditions.

Frequency / Hz	Amplitude / µm	Acceleration / m/s^2
80	1000	253
135	1000	719
200	1000	1580

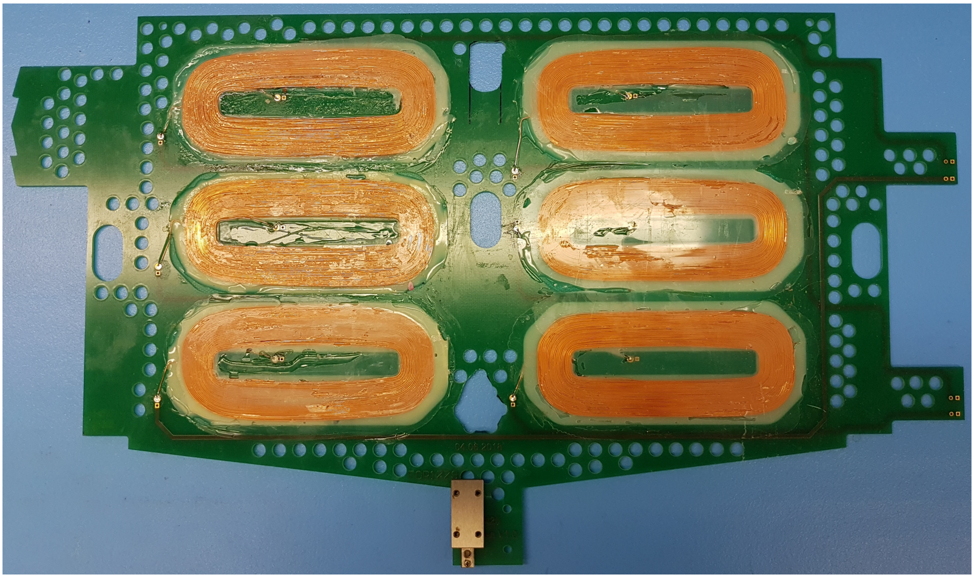

Figure 7.1: Actuator bar for system 3.x. The bearing at the bottom was estimated in simulation to shift the eigenfrequency of the tilting oscillation up, out of the target operating range.

The main drawback of the actuator 2.1 system is the small amplitude. The system which was planed to solve this problem is called actuator 3.x. It also contains enhancements to overcome the unwanted tilting oscillations described in Section 4.1.4.

The amplitude to be reached depends on four forces, the Lorentz force on the actuator coil and, counteracting this force, the inertia of the actuator bars, the reset force from the displaced surface material and the friction. Inductive forces do not play a significant role, which will be discussed later (Section 7.2.2). Friction is difficult to estimate. However, various design decisions have been made to ensure low friction, so its influence will be ignored for the time being. Reset force from the surface will stay the same regardless of the size and mass of the actuator bars moving it, while inertia scales proportional with mass. Therefore, actuator system 3.x was designed with more massive actuator bars which produce higher total force. This means that reset force will play a reduced role relative to inertia compared to system 2.1. The impact of inertia can be estimated by calculating the maximum acceleration a_{max} necessary for achieving a sine trajectory at a given angular frequency ω and amplitude A:

$$a_{max} = \max(\ddot{z}) = \max(A\omega^2 \sin(\omega t + \phi)) = A\omega^2 \tag{7.1}$$

This equation gives the lower bound of force necessary to reach a given amplitude and frequency via $F = ma$ (for examples of a_{max} see Table 7.1) for which the actuator system 3.0 is optimized. The major steps of this optimization were to: maximize Lorentz force, keep the mass of the actuator bars as low as possible and use the minimum amount of bearings necessary for robust mechanical guidance to keep friction low. More details on this optimization follow in Section 7.2.

In addition, system 3.0 brings utility advantages. The slopes, previously available through 3D printed extensions, are part of the new bar design. The same dual light barrier sensors as in system 2.1 are used with the slopes, measuring center of mass trajectory and tilting. The important improvement for System 3.0 is that it also provides two methods to counteract unwanted tilting. One method is a linear bearing at the bottom of the actuator bar (Misumi BSGM6-25 [28], see Figure 7.1), as was simulated before (see Section 4.1.4). To verify that this solution works as intended, tilting amplitude is measured relative to the amplitude of the center of mass trajectory:

$$\delta_{tilt} = 2 \cdot \frac{A(z_{left} - z_{right})}{A(z_{left} + z_{right})} \tag{7.2}$$

with the amplitudes determined by averaging the instantaneous amplitude obtained by Hilbert transform and averaging, which is shortened as $A(\ldots)$ here. The position trajectories z_{left} and z_{right} are measured at the opposite ends of the bar, left and right from the point of view of the operator. The average of z_{left} and z_{right} at any given point in time is a measure for the trajectory of the center of mass, because it is by design in the middle between the ends of the bar.

Tests on a prototype system have shown that the tilting is reduced from typically 20 % for the actuator System 2.1, to less than 5 % in the worst case and typically 2 % for the system 3.0 prototype. This method of reducing the tilting is limited by the amount of slack in the linear bearing, which is approx. 17 µm (see [28]).

The second method to deal with tilting oscillations lies in the dual coil stack approach (see Figure 7.1), which makes it possible to balance forces such that tilting is prevented. However, this technique was not tested in practice and remains as an option for further optimization of the system. For further friction reduction this approach may allow for removing the linear bearing and solely relying on feedback control for balancing.

7.2 FEM Aided Performance Improvement

As of Equation 2.1, there are three options to increase Lorentz force: increase the length of wire immersed in the magnetic flux, increase the current and increase the flux density. The first two are usually a compromise between choosing a thin wire for more length and choosing a thick wire for higher ampacity. The product of both usually stays roughly constant for a given coil geometry. Increasing the cross sectional area perpendicular to the wires will allow for an increase of this product at the cost of adding wire and thus mass. By contrast, increasing the flux density is possible without any increase in the mass of the actuator, increasing maximum acceleration.

7.2.1 Static Magnetic Flux

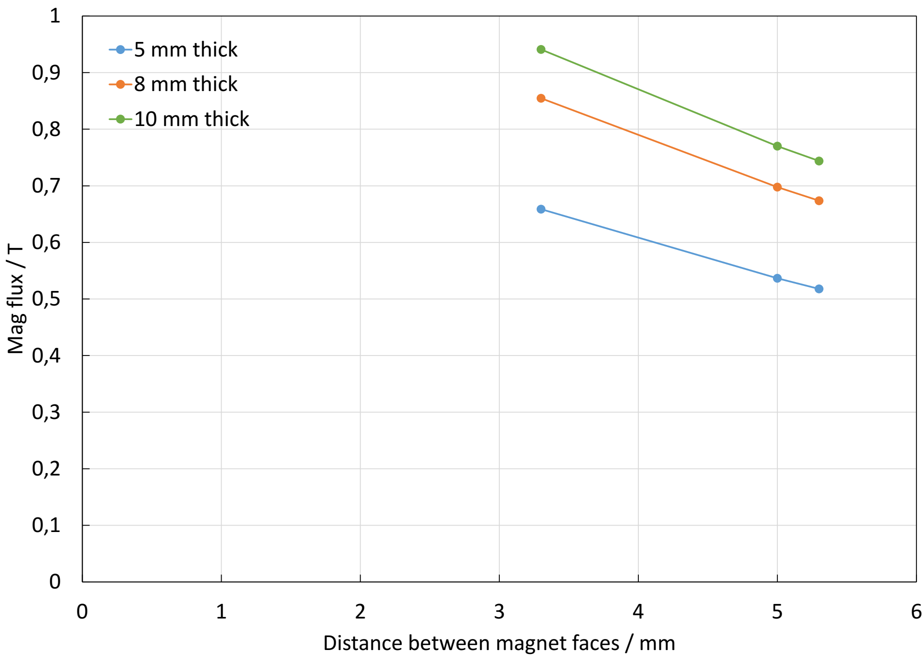

Figure 7.2: This graph describes the progression of flux density as found by simulation with regards to gap width and magnet thickness.

The setup was simulated using FEM to quantify the expected flux densities [10]. To reach higher flux density at the location of the coil, the distance between magnet faces was reduced (from 5 mm to 3.3 mm) and thicker magnets were chosen (from 5 mm to 10 mm). Figure 7.2 indicates how these changes affect flux density. The results of the simulation were checked in a prototype using the hall sensor described previously (see Section 3.8), which gave readings of 0.9 T to 1.0 T confirming the simulation result. The significant increase from 0.54 T to 0.94 T, however, also led to much higher attractive forces between the holders.

The system 2.0 design is mechanically more conservative than system 3.0. It possesses less magnets at larger separation. By closing gaps between the magnets almost the whole coil could be immersed in magnetic flux. This change improved the current-turn product without adding mass. The sideways forces generated because of the immersion of curved coil parts at both ends cancel out and almost all wire that can generates z-direction Lorentz force.

In addition, the magnets are stacked on top of each other with alternating poles. This way they attract each other at the upper and lower edges, which makes these stacks relatively easy to build. The main reason for this choice, however, is that coils can be placed as close as possible to each other to avoid dead mass in the actuator bar. Also, they can be spread as thin as the manufacturing process allows while keeping a given current-turn product. This geometry leads to a high surface area to volume ratio, which improves cooling.

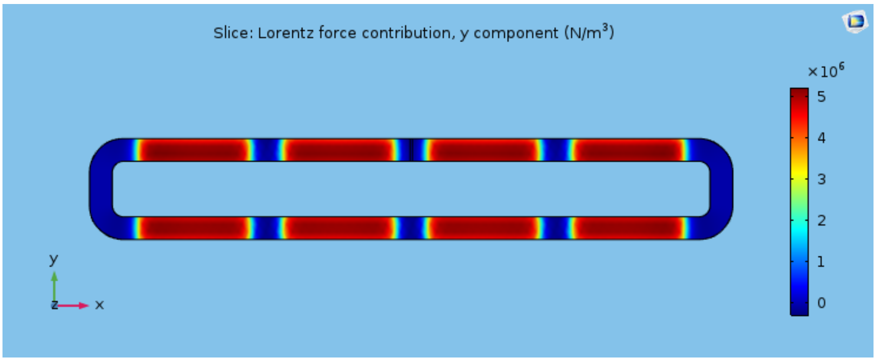

Figure 7.3: This graphic shows a simulation result of the Lorentz force per volume on the coil of the actuator 2.0 system.

For this setup a force-current ratio of 96.7 N/A was predicted by simulation and (95 ± 2) N/A was measured for the 3.0 prototype (see Section 7.3.1) while for the actuator 2.1 system 17.5 N/A was calculated (for central actuators) and (18 ± 3) N/A was measured (see Figures 7.3 and 7.4 for a comparison). Unfortunately, the holder stacking process became too unreliable due to the decreased mechanical robustness of the holder.

In an effort to reduce the forces between holders and to provide additional

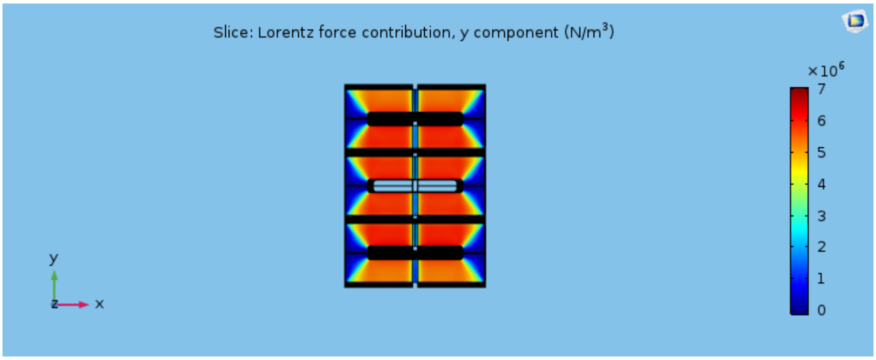

Figure 7.4: This graphic shows a simulation result of the Lorentz force per volume on the coil of the actuator 3.0 system.

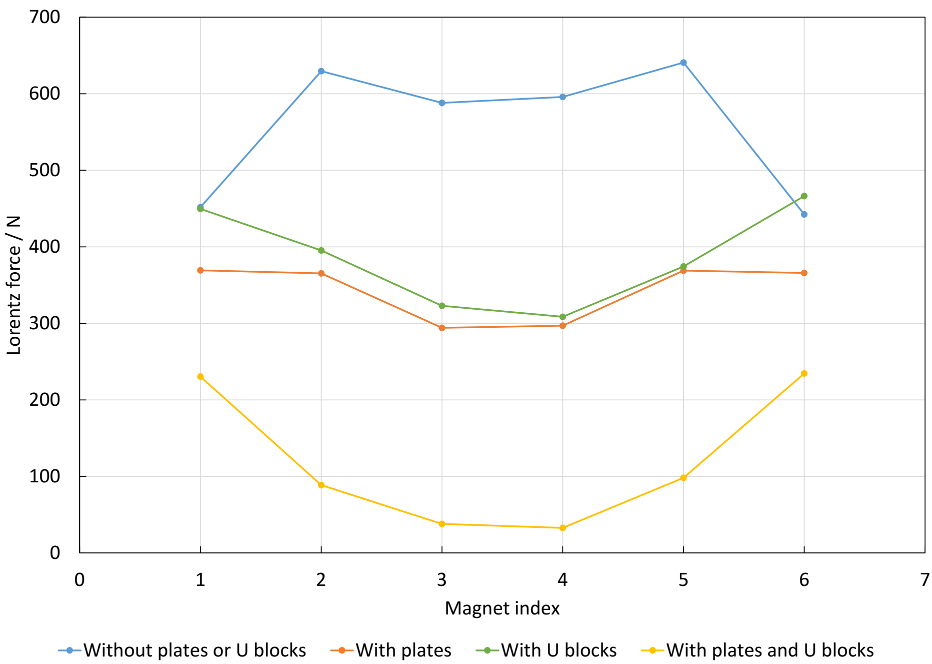

Figure 7.5: This graph plots attractive forces between magnet stacks.

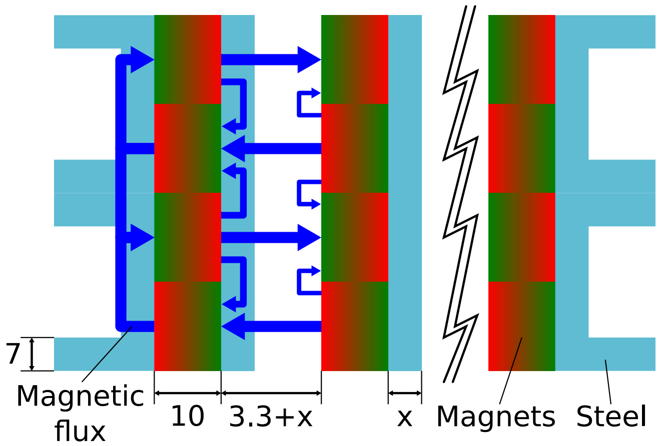

Figure 7.6: This graphic shows placement shape and measures of the steel parts added for increased stability and flux density.

gluing surface to fix magnets, the addition of ferromagnetic steel sheets and U-profiles on the outside was evaluated (see Figure 7.6). The simulations predicted a decrease in forces on the magnet holders (see 7.5). These forces were not verified through direct measurement. Still, the reduction of forces probably contributed to less holders failing in the 5 bar system 3.1 prototype (1 out of 6, instead of 2 out of 4 in the 3 bar system 3.0 prototype).

7.2.2 Losses and Heat removal

In parallel with the optimization of the static properties, which are mass, flux density and immersed wire length, dynamic properties were also studied [32]. At first glance, it seems troublesome to have magnet holders of solid aluminum next to coils driven with alternating current, as the induced eddy currents in the holders could be a major loss factor. No obvious analytic or empirical solutions can be applied and a measurement separating this power loss from ohmic power loss in the coil is difficult. The COMSOL FEM simulation makes a prediction available. It was found that only a minor fraction of power, below 3 % at frequencies up to 135 Hz, is lost due to eddy currents.

In addition, one more side effect of completely surrounding the coil with magnets in system 3.0 and magnets and steel sheets in system 3.1 is that those materials (NdFeB [9], EN 10130 steel [33]) have much lower conductivity than aluminum, reducing the amount of power loss through eddy currents [43].

Maximum acceptable temperature is an important factor for the ampacity of the wire and, accordingly, for the performance of the actuators bars. It is difficult to measure because of limited access and limited space in the relevant area (where the coil is attached to the PCB bar). For this reason, a simulation was used to predict heating behavior and compared to measurements of temperature in a coil glued to PCB a in the open. The simulation predicted different dynamic behavior and an unrealistic saturation behavior. It seems to be relatively limited. Although the actuator is enclosed inside the system, it can be assumed that the neighboring aluminum will conduct away most heat as soon as it is transferred via the air gap resulting in similar cooling as in the open, where it can be measured more easily.

7.3 The 3.x Prototypes

The first prototype built on the basis of the FEM simulations was a 3 bar prototype (Figure 7.7) following the ideas outlined in Section 7.1. For comparison, the important properties of system 2.1 and system 3.0 and the later iteration 3.1 (summarized as 3.x) are shown in Table 7.2. The new actuator has almost triple the maximum acceleration, while having more mass at the same time, so reset force and, to a lesser degree, friction play a less important role for the maximum amplitude. Therefore, system 3.x should be able to triple the maximum amplitude reached with system 2.1 to around 1000 µm.

As discussed in Section 7.2.1 the outer actuators of the system 3.0 experience much higher attractive forces than the internal holders. In combination with small problems during the gluing process the higher forces led to both outer holders failing (similar to a previous attempt seen in Figure 7.8). The magnets clamped down on the actuator bars 1 and 3 and stick friction became so high that it was not possible to move

Figure 7.7: The actuator system 3.0 prototype.

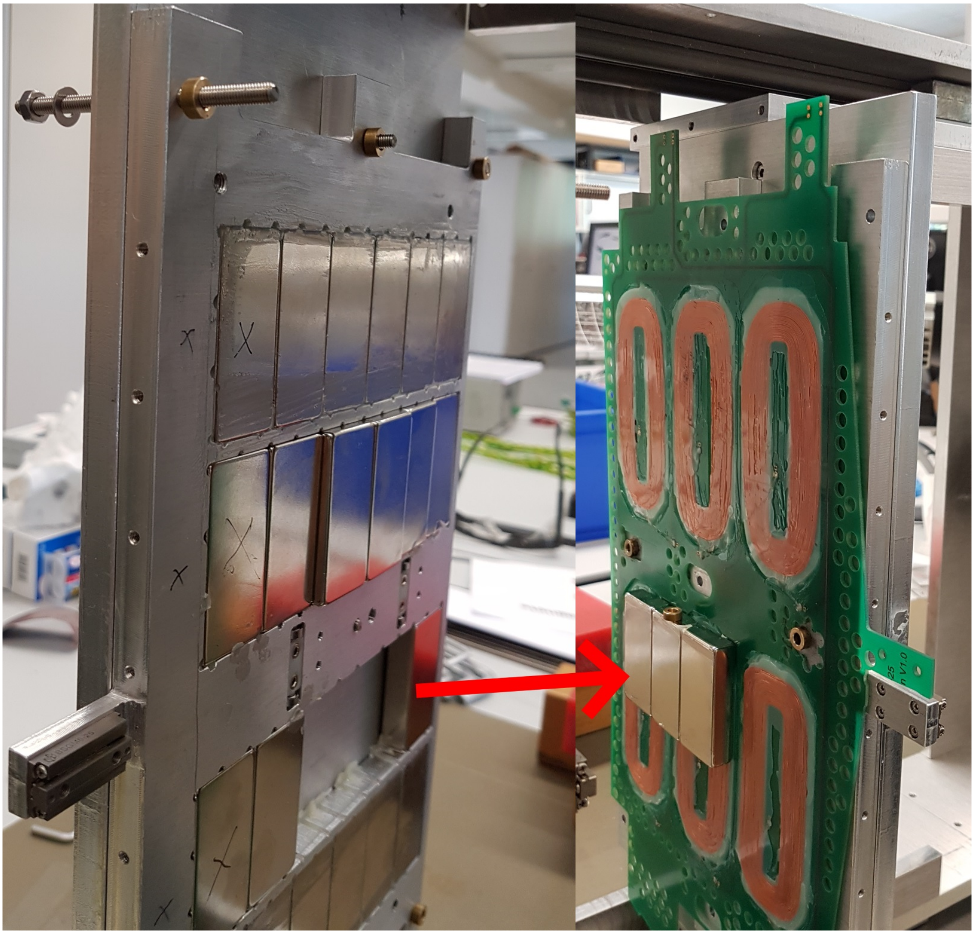

Figure 7.8: Due to high attractive forces between permanent magnets, the outermost holders of the three bar system 3.0 prototype broke down.

Table 7.2: General mechanical, electrical, magnetic and performance properties of the actuator versions 2.x to 3.x.

Parameters for system version	2.x	3.x
Spacing in mm	10	13.3 to 13.9
GRP thickness in mm	0.2	0.2
Dimensions of magnets in mm	$50 \times 15 \times 5$	$50 \times 25 \times 10$
Magnetic energy product in MGoe	48	52
Coil dimensions in mm	$285 \times 44 \times 1.0$	$105 \times 40 \times 1.2$
Coil Cu-wire diameter in mm	0.28	0.355
Number of turns	80	140
Coil resistance in Ω	14	4
Coil ampacity in A	1.25	1.75
PCB mass in g	38	96
Coil mass in g	27	110
Bar total mass in g	90	230
Magnetic flux density in T	0.54	0.94
Maximum acceleration in m/s^2	320	1060

them anymore with reasonable force. However, the middle actuator was free of such problems, which at least gave the opportunity to check some predictions.

7.3.1 Performance of System 3.0

A force measurement on the free bar was conducted with the force sensor and test stand described in Section 3.8. The same was done previously with actuator 2.0. The Force sensor was fitted with a 3D printed adapter. This adapter has a flat bottom that allowed it to be set down on the center of the top of the actuator bar and to balance it when it was actuated upwards. The current was set to predetermined values and the corresponding forces were measured. For actuator system 2.0 this measurement gave $(18 \pm 3)\,\mathrm{N/A}$.

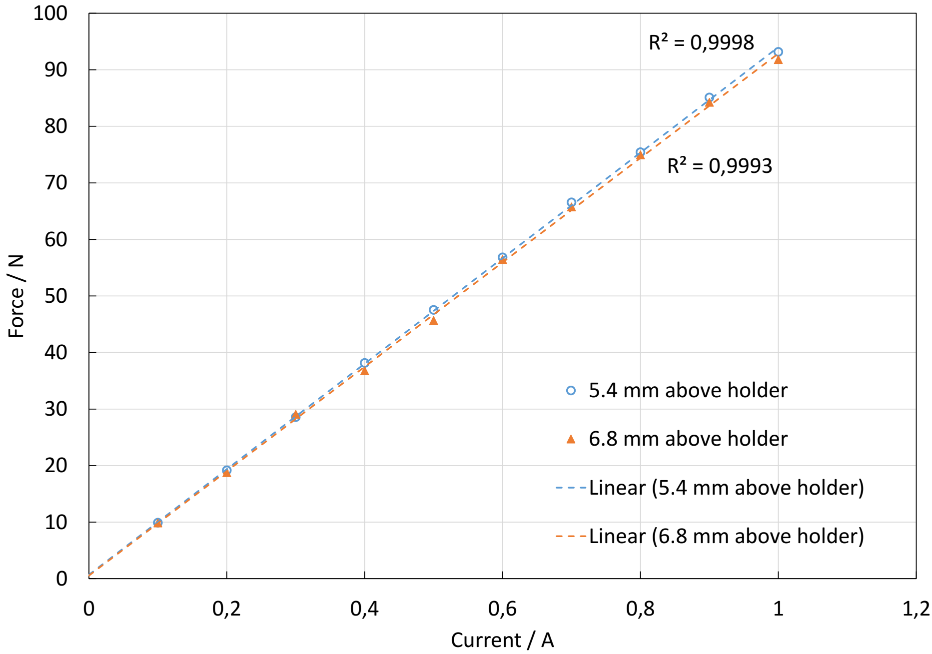

Figure 7.9: Force-current diagram. The effect of gravity has been compensated for. The R^2 measure of linear fits is very close to unity indicating highly linear behavior.

The results for the actuator system 3.0 are shown in Figure 7.9. Measurements at two z-axis positions at a distance of 1.4 mm were taken. The differences are minor (i.e. $<2\,\mathrm{N}$) and do not follow any trend. Therefore, the design can be deemed successful in this regard, making sure that adjusting the surface position within the design limits will not lead to issues with current to force nonlinearity. In addition, current to force relation is highly linear as expected. To determine the force per current, all forces were corrected by adding $0.23\,\mathrm{kg} \cdot 9.81\,\mathrm{m/s^2}$ to compensate for the weight of the actuator itself. By averaging all measurements we find a ratio of $(95 \pm 2)\,\mathrm{N/A}$, using the standard deviation of the ratios of average force to set current as estimate for the error. Therefore, the prediction from simulation of $96.7\,\mathrm{N/A}$ is within the error margins (see Section 7.2.1).

To determine the maximum force for a system 3.0 bar, the ampacity has to be determined (similar to system 2.0, see Section 4.4). Using the less sophisticated setup of having the bar placed on a laboratory table with the coil facing up, ampacity was measured. Steady state was assumed to be reached after 180 s instead of 900 s. The air cooled measurement for 1.75 A yielded 106 °C as final temperature, which was deemed acceptable and, thus, set as ampacity of system 3.0. Though this ampacity is not fully comparable with the one of system 2.1 since the safety margin in temperature is smaller, it is the one used in practice.

The prototype was completed as far as possible by attaching a frame and gluing a surface to it. The center actuator, which was not affected by holders breaking, and the surface were positioned so they would not get into contact with the other, stuck bars during actuation. The inner width of the frame is 80 mm, which means that the actuator bar in the prototype was driving a standing wave with the commonly used 160 mm wavelength. This setup provides a rough impression of the amplitude that could be reached with the final setup when only half of the actuators contribute. The amplitude and y-tilting motion were measured by the dual light barrier sensors and two laser triangulation reference sensors (see also Section 3.8) on both ends of the bar.

The measurements of amplitudes by light barrier and reference sensors agree well within the typical 3 % error margin for the light barrier sensors, while the reference sensors were estimated to give a the same error 3 % due to the whole actuator system vibrating relative to the mounting frame of the reference sensors. Therefore, it is confirmed that the dual light barrier sensor also works well on this version of the actuator. The gains (amplitude per current) found are higher than the ones reached by actuator system 2.1 (see Figure 7.10), which compounds with the higher ampacity. This way, System 3.0 reaches the original goal of 1000 µm amplitude at 81 Hz. It also covers most of the target parameter range with regards to frequency and amplitude (wavelength cannot be tested in this setup).

In addition, the test shows reduced y-tilting compared to the typical 20 % for actuator system 2.1 (see Figure 7.11). Error margins are larger for the light barrier sensor based on deviations between repeated measurements. For the reference sensors the estimated typical deviation of 1 µm is used as basis of the error margin. All test results were obtained without feedback

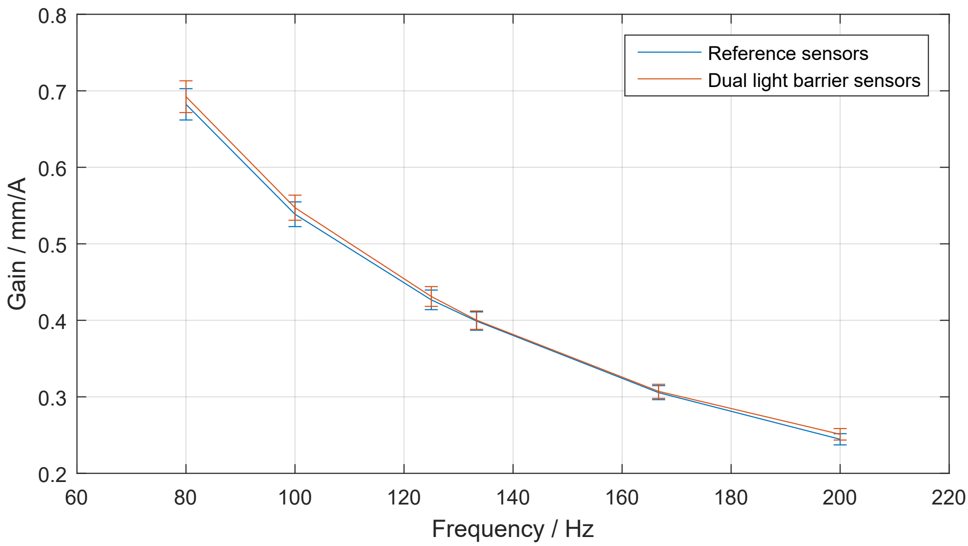

Figure 7.10: Gain of the actuator system 3.0 measured with Laser reference sensors and light barriers.

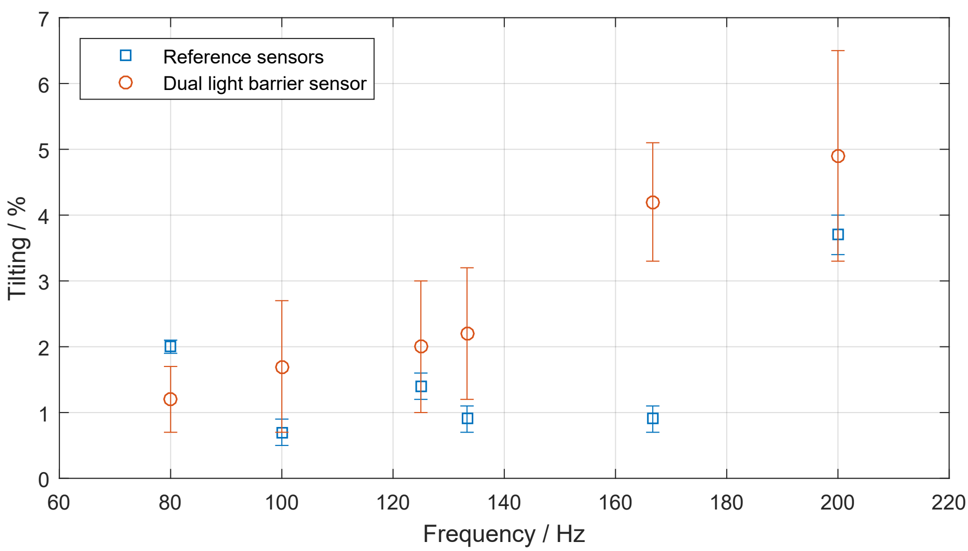

Figure 7.11: Tilt of the actuator system 3.0 measured with Laser reference sensors and light barriers.

control of the tilting via the two independent coil stacks. The reduction is only due to the added linear bearing at the bottom of the bar. Since this improvement reduces tilting to below 5 % in all cases, and even less in many, an additional feedback control seems unnecessary. Nevertheless, it was tested using PID, which ran into problems due to misalignment of sensed zero-tilting position and the position enforced by the linear bearing, resulting in the PID unnecessarily pressing against the bearing, degrading performance and increasing wear on the bearing. To avoid this effect, a deadzone as used with zero level control could be employed. Also, an ILC might be a better fit than PID since, though the reference would not be periodic (always zero), the disturbances would be (see also Section 5.3).

Although the construction of the magnet holders had to be improved, the 3.0 prototype underlines the expectation that the design is capable of reaching the goals we set to achieve with it.

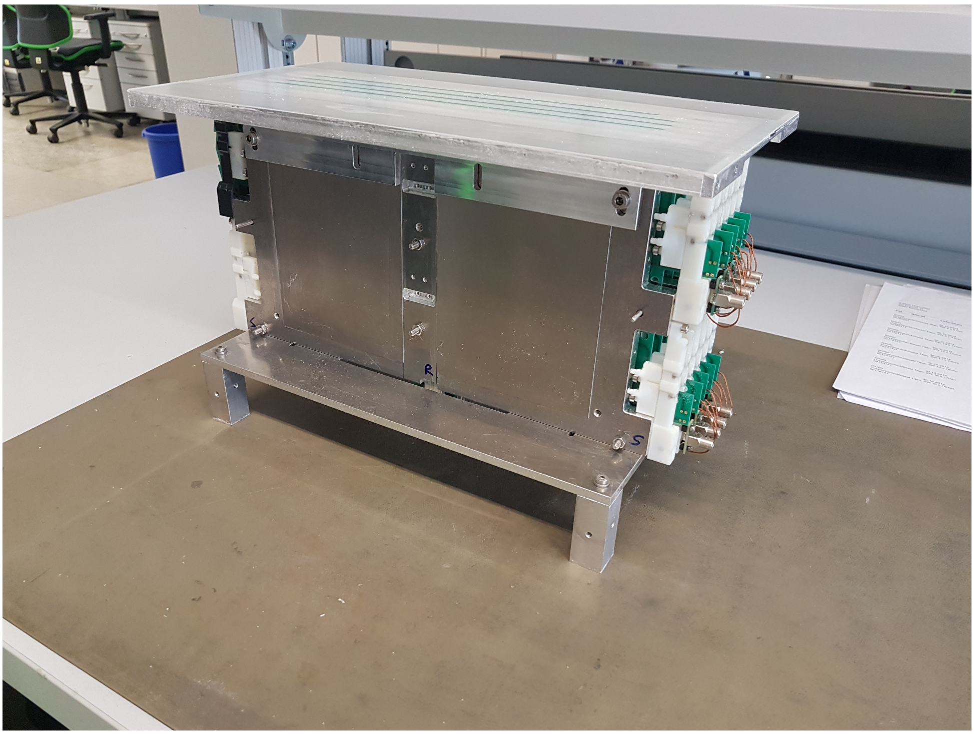

Figure 7.12: The actuator system 3.1 prototype.

The express goal of the 5 bar prototype of the actuator system 3.1 (see Figure 7.12) was then to test, how much reliability of the magnet holders had been increased by the addition of the steel sheets previously simulated (see Section 7.2.1). The main goal here was to add as little steel as possible not to decrease the spatial resolution too much. The spacing was increased from 13.3 mm to 13.9 mm as 0.5 mm thick steel sheets were inserted on one side covering two magnet stacks each (as seen in Figure 7.12). Still one of the outer holders broke down, which amounts to a failure rate of one out of six. Further developments are in progress to increase the reliability of the manufacturing process.

7.3.2 Full-Scale System 3.1

Based on the experience from our work on the 5 bar prototype a full scale 15 bar system has been built (see Figure 7.13). It reaches a mass of roughly 30 kg, about 3 times more than system 2.1. This is more weight than can be safely handled by one person, which is why two bars with grips can be attached at the bottom on either of the longer sides of the Actuator. It also required one additional amplifier rack with 10 channels, for a total of 30 channels, as each actuator now posses two channels to feed, one for each coil stack.

The control algorithms have been proven to work despite the severe flaw of strong y-tilting in the actuator system 2.1. The drastic reduction of this effect in system 3.1 makes it easier to control. Higher learning gains are possible, leading to quicker convergence.

The final performance of the System was tested in a similar manner to System 2.1. The results are shown in Table 7.3. The full System 3.1 reaches 1000 µm amplitude at 80 Hz as we had hoped based on testing system 3.0.

Experiments presented in Section 6.2 and previous research [36] [23] show that there seems to be a tendency towards increased drag reduction with increased frequency for the tested parameter ranges. The full-scale actuator system 3.1 extends the parameter range in this direction up to 200 Hz. Furthermore, ILC makes higher phase shifts between actuators up to 60° available (see also Section 5.3.2), which allows for reaching

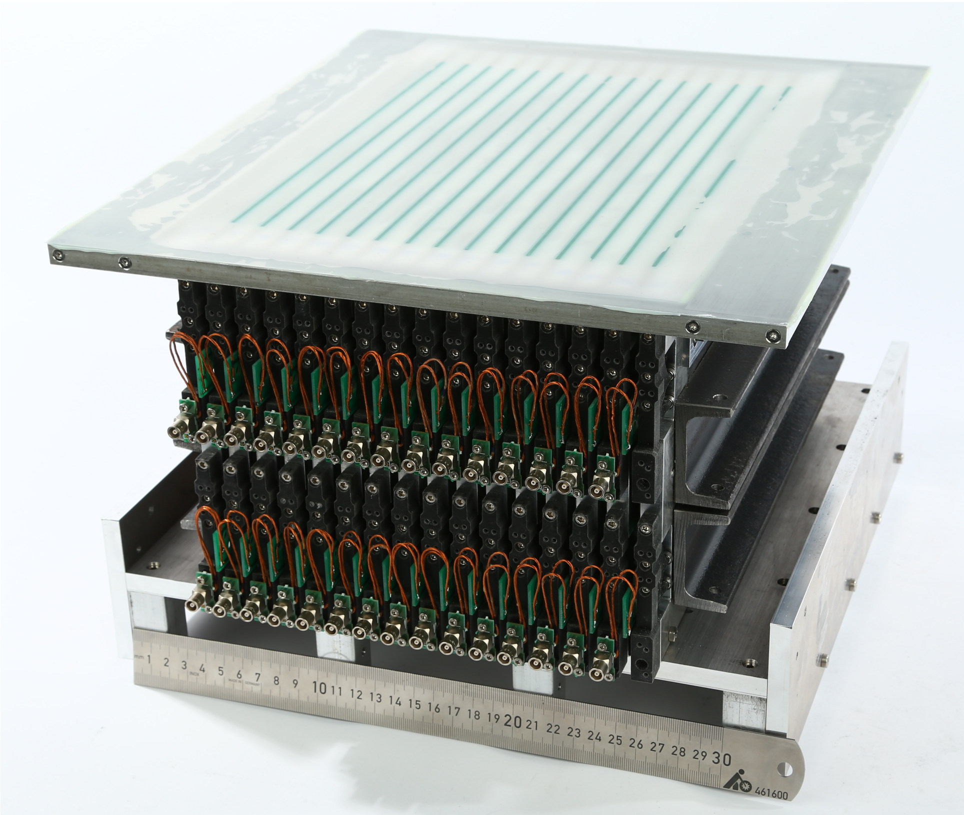

Figure 7.13: The full scale actuator system 3.1 with 15 bars. There are also 30 Lemo connectors, one for each coil stack. The sides are reinforced with steel U-profiles. Rectangular bars (not shown) can be attached at the bottom using screws. This makes handling the heavy system easier.

Table 7.3: Performance reached by the full scale actuator system 3.1.

Frequency / Hz	Amplitude / µm
80	1000
100	800
120	700
140	600
160	500
180	450
200	350

80 mm wavelength on system 3.1, the original goal of system 2.1. With six actuators per spatial period it is still far away from the Nyquist limit to ensure a decent approximation of a sine shaped wave.

7.4 Summary

The goal of increasing the actuation amplitude at target frequencies has been approached by various design choices for actuator 3.0. The dead mass of the bar is kept low by placing the permanent magnets and, therefore, also the coils as close as possible together. The coils are almost fully inside the magnetic field. As is shown by FEM, the reduction in gap width between magnets and increase in their thickness almost doubles magnetic flux. The FEM simulations also find that eddy currents are not a significant power sink and can be safely ignored in the design considerations. As measurements on the prototype built based on these ideas show, the amplitude can be indeed significantly increased (i.e. to 1000 µm at 81 Hz).

Tilting in y-direction is the other major issue addressed in the design of actuator 3.0. A bearing can be added at the bottom without decreasing mechanical stability since it is part of the bar design from the beginning. Also, severe performance loss is not expected due to the relatively smaller mass of the bearing. In addition, the coils are placed in two columns, so a counter torque can be applied if necessary. Indeed, measurements show that the bearing alone is sufficient to suppress tilting to a satisfactory degree.

Unfortunately, the mechanical stability of the magnet holders proved insufficient. The two outer holders of the 3.0 prototype broke down under the attractive force of the permanent magnets. Therefore, including steel sheets on one side of the magnets and U-profiles on the first and last holder for reinforcement has been studied with FEM. It has been found to reduce attractive forces while not significantly impacting the desired high flux density. Implementing this measure leads to design 3.1. The full scale system based on this design achieves the original goal of an amplitude of 1000 µm at 80 Hz. In addition, it also provides higher frequencies up to 200 Hz at lower amplitudes, of course. The following chapter puts this result into the broader perspective of the results shown in the other chapters and concludes this thesis.

8 Conclusion and Outlook

The two main objectives of this thesis have been: to develop feedback control for actuator system 2.0 and to optimize the design to fully cover the desired parameter range. The first has been achieved by modeling and, in parallel, upgrading the actuator system 2.0. For the actuator system 2.1, which has been the result of the upgrade, a feedback control has been designed that has enabled wave actuation and wind tunnel experiments. Based on studies of system 2.1 with the help of FEM a new actuator system has been developed, actuator system 3.x. The prototype has thrice the maximum acceleration of actuator 2.1 and reaches amplitudes of up to 1000 µm and frequencies of up to 200 Hz, achieving the second objective.

The first step on the way towards these results has been to model the actuator system in terms of a differential equation (see Chapter 4). Rotational oscillations have been neglected in this model. FEM has been applied to study the problem and propose an additional bearing as solution. This solution has not been applied to this system due to potentially degrading performance. Also, position sensors have been redesigned to accurately measure center of mass movement and rotational oscillations. During this upgrade aluminum was replaced by GRP as surface material offering decreased reset force for higher amplitudes and easier glue inspection due to it being transparent. The system has been referred to as actuator system 2.1 from this upgrade onward.

Building on the models, control design was prototyped on a three actuator test system (see Chapter 5). Initially a classical PD controller has been used to prove that feedback control can be applied to the system. It has also shown not to be capable of tracking required phase shifts at target parameter sets. ILC, a different control method, is better suited for the task of controlling this system, since the given reference trajectories and the expected disturbances are periodic. Previous work on gain switching ILC in simulation has been successful and motivated the implementation of ILC for the test system. This implementation was successful in producing a traveling wave at 20 Hz. The larger, upgraded system 2.1 posed some additional challenges, such as mechanical hysteresis. The control design to overcome these challenges features three important components, separated in two groups via their bandwidth: a deadzone PI control for steady state and low frequencies on the one hand, and a decoupling for a single frequency enabling zero phase filtering SISO ILCs for the target wave frequencies on the other hand.

In verification testing, adhering to ISO 9001:2015, this approach has been proven capable of producing traveling waves at a frequency up to 108 Hz, at an amplitude of up to 375 µm and a wavelength of 160 mm (see Chapter 6). The wave quality indicators for these waves have been within the required ranges. Online parameter changes in form of step response tests for amplitude (response time 3 s) and wavelength (response time 7 s) have also been conducted successfully. In subsequent wind tunnel experiments similar results as with system 1.0 have been obtained at similar conditions. At increased frequencies, which were not accessible with actuator system 1.0, promising results of increased drag reduction have been obtained. However, they still lie within the margins of error of results with the previous system. With the possibility of online parameter changes the actuator system can respond to unsteady inflow conditions in future wind tunnel experiments, which has been a major goal of the developments during the second funding period of FOR 1779.

The maximum frequency of 108 Hz and amplitude of 375 µm are smaller than the desired maxima of 135 Hz and 1000 µm (see Chapter 7). To overcome this problem, a completely new actuator system has been designed. For the optimization of this design, FEM has been employed. Static simulations have helped improve magnetic flux density from 0.54 T to 0.94 T. These simulations have also supported planning of magnet placement and coil design. By doing so, dead mass has been decreased and almost full immersion in magnetic flux has been reached. Therefore, maximum force per bar has increased from 23 N to 163 N and maximum acceleration has increased from 320 m/s^2 to 1060 m/s^2. Dynamic simulations have found that power loss through eddy currents to be acceptable at <3 %. Measurements on first prototypes reached amplitudes of 1000 µm at 80 Hz.

Based on the results of this thesis the advanced actuator system 3.1 with 15 bars at a 13.9 mm spacing has been built. It reaches, among other working points, the predicted amplitude of 1000 µm at 80 Hz and at a wavelength of 160 mm. From there it makes higher frequencies available to the aerodynamics researchers reaching up to 200 Hz where it still provides an amplitude of 350 µm. It also maintains the high quality of actuation discussed earlier based on the control method developed during this thesis. After an unfortunate failure, the power amplifiers have been repaired and reinforced. The system is now standing by for further research.

Of course certain limitations apply to the results of this thesis that point the way to topics for future research. One such limitation is revealed by the single frequency model. The fact that this model, without any a priori physical knowledge of the system, is more successful than the state space model suggests that some of the assumptions made for the physical model might not hold at the target frequencies. One is the assumption that the system is linear, which is, indeed, not the case at target frequencies (see Section 5.5). To further improve control, instead of the static model employed in the successful control approach described in this work, a dynamic model for the system is necessary which can also handle nonlinearity, e.g. a recurrent neural network [4]. The main concern with neural networks as models lies with training data, which are readily available with the actuator system. It is built to withstand long term use, so that more than sufficient data could be gathered. Such a nonlinear dynamic model may not only capture the fast target frequency behavior, but also the slow hysteresis present in the system. Such a unified, more accurate model would pave the way to higher control performance, i.e. shorter convergence times, and more elegant control designs, i.e. no need for a separation of loops into different frequency bands.

Another limitation is, that with the approach shown here only parameter transitions in amplitude and wavelength have been realized. There are ideas of how to address parameter transitions in frequency. The next iteration control action could be modified by compressing or stretching it in time together with the ILC period. Depending on the learning gain this technique can be applied in more or less small steps every period to ensure a smooth and fast transition during wave actuation. Though intuitive, this idea needs to be researched further to determine its merits.

With regards to the physical and technical limits of the actuator system, consider the following plausible set of outcomes: no dead mass through advanced construction similar to voice coils ($\times 2$) and aluminum as conductor for a better mass to current-turns ratio ($\times 2$), a higher temperature limit of 220 °C and, thus, ampacity, as in some audio applications [19], and improved cooling ($\times 2$), a high performance iron core electromagnet with a static flux density of 1.8 T [38] ($\times 1.8$). Despite the very roughly estimated $\times 14$ improvement in maximum acceleration, the technical challenges are just as, if not far more, significant.

Future research and engineering decisions will depend on the predictions of highly anticipated numerical parameter studies. Given a fixed maximum acceleration, which determines the maximum product $A \cdot f^2$ of amplitude and frequency, an optimum parameter set with regards to achievable drag reduction may be found.

The methods and tools described in Chapter 3 have proven themselves invaluable for the task of rapid prototyping and offer, in conjunction with the results of this thesis, excellent conditions for further development of the Lorentz force actuator system.

Curriculum Vitae

Martin Florian Seidler
Propst-Bechte-Platz 16
52428 Jülich

Tel.: 01578 / 4585043
E-Mail: florian.m.seidler@gmail.com

Born on the 21st of August 1990 in Cologne

Education

Feb. 2020	Defense of this PhD thesis at the Institute for Automated Control, RWTH Aachen University, Aachen
2016–2020	Graduate studies in engineering at the RWTH Aachen University in cooperation with Forschungszentrum Jülich GmbH
May 2015	Master of science in physics with a thesis on high bandwidth digital control for quantum optics experiments supervised by Univ.-Prof. Dr. Dieter Meschede, Institute for Applied Physics, Bonn
Sep. 2012	Bachelor of science in physics with a thesis on the machining of glass fiber end facets supervised by Univ.-Prof. Dr. Meschede, Institute for Applied Physics, Bonn
2009–2015	Physics studies at the University of Bonn
2000–2009	St. Ursula Gymnasium, Brühl
1996–2000	Montessori elementary school Gilbachstr., Cologne

Languages

German	Native speaker
English	Fluent
Latin	Intermediate (writing)

Publications and Conferences

2019	IEEE CoDIT (April) in Paris, seminar talk and proceedings (peer reviewed) in press, F. Seidler, M. Schiek, W. Silex, R. Heil, S. van Waasen, D. Abel, “Iterative Learning Wave Control of a 20 Actuator System for External Flow Research”
2018	IEEE CCTA in Copenhagen, seminar talk and proceedings (peer reviewed), F. Seidler, M. Schiek, W. Silex, R. Heil, S. van Waasen, D. Abel, “Iterative Learning Control and Decoupling of Lorentz Force Based Actuator Systems for Turbulence Research”
2017	IEEE Sensors Conference in Glasgow, poster and proceedings (peer reviewed), F. Seidler, M. Schiek, W. Silex, R. Heil, S. van Waasen, D. Abel, “Sensors for waveform control in a Lorentz force based actuator system for turbulence research”
2016	VDI Automation Conference in Baden-Baden, Poster, F. Seidler, J. Trabert, M. Dück, S. van Waasen, M. Schiek, D. Abel, E. B. Castelan, “Control of Nonlinear Coupled Electromagnetic Actuators for Active Drag Reduction in Turbulent Flow”
2015	DPG spring meeting in Heidelberg, Poster, F. Seidler, W. Alt, A. Alberti, D. Meschede, “Digital intensity control for optical lattice experiments”

October 22, 2020

Bibliography

[1] Ahlborn Mess- und Regelungstechnik GmbH. *Infra-red transmitter for measuring surface temperature AMiR 7843*. 2018. URL: https://www.ahlborn.com/download/pdfs/kap07/eng/infrarot/amir7843e.pdf.

[2] Alluris GmbH. *FMI-B50Digital Force Gauge for Force vs. Displacement Measuring*. 2019. URL: https://alluris.de/media/fmi-b50_EN.pdf.

[3] Analog Devices, Inc. *Small, Low Power, 3-Axis ±200 g Accelerometer*. 2012. URL: https://www.analog.com/media/en/technical-documentation/data-sheets/ADXL377.pdf.

[4] Coryn A. L. Bailer-Jones, David J. C. MacKay, and Philip J. Withers. "A recurrent neural network for modelling dynamical systems". In: *network: computation in neural systems* 9.4 (1998), pp. 531–547. URL: http://citeseerx.ist.psu.edu/viewdoc/download?doi=10.1.1.15.5707&rep=rep1&type=pdf.

[5] D. A. Bristow, M. Tharayil, and A. G. Alleyne. "A survey of iterative learning control". In: *IEEE control systems magazine* 26.3 (2006), pp. 96–114. DOI: 10.1109/MCS.2006.1636313.

[6] Louis N. Cattafesta and Mark Sheplak. "Actuators for Active Flow Control". In: *Annual Review of Fluid Mechanics* 43.1 (Jan. 2011), pp. 247–272. DOI: 10.1146/annurev-fluid-122109-160634.

[7] DFG. *FOR 1779: Aktive Widerstandsreduktion durch wellenförmige Oberflächenoszillation*. GEPRIS. 2011. URL: http://gepris.dfg.de/gepris/projekt/202175528.

[8] Marcel Dück. *Model-based driving of spatially distributed actuator and sensor networks in flow control*. de. Vol. Diss. RWTH Aachen University, 2016. DOI: 10.18154/rwth-2017-01453.

[9] Eclipse Magnetics Ltd. *NdFeB Magnets / Neodymium Iron Boron Magnets Datasheet*. Apr. 28, 2019. URL: https://www.eclipsemagnetics.com/media/wysiwyg/datasheets/magnet_materials_and_assemblies/ndfeb_neodymium_iron_boron-standard_ndfeb_range_datasheet_rev1.pdf.

[10] Courtney Ford. "Time-Independent Finite Element Simulations of Magnetic Behavior in an Actuator System Used for Research Concerned with Active Drag Reduction". MA thesis. Physics department, University of Bonn, 2019.

[11] James M. Gere. *Mechanics of materials*. eng. 6th ed. Brooks/Cole-Thomas Learning, 2004. ISBN: 0534417930. URL: http://www.loc.gov/catdir/toc/fy0611/2003113085.html.

[12] E. G. Gilbert. "The decoupling of multivariable systems by state feedback". In: *SIAM Journal on Control* 7.1 (1969), pp. 50–63. URL: https://www.researchgate.net/profile/Mohamed_Mourad_Lafifi/post/What_is_Coupling_and_Decoupling_in_Control_system_engineering/attachment/59d633ac79197b8077991581/AS%3A375740286685185%401466594873400/download/Decoupling+of+Multivariable+sys+by+State+Feedback.pdf.

[13] David J. Griffiths. *Introduction to Electrodynamics*. Cambridge University Press, 2017. ISBN: 978-1108420419. URL: http://kestrel.nmt.edu/~mce/Electromagnetics_by_Griffiths-1.pdf.

[14] Henkel AG. *LOCTITE EA 9466*. Post Office Box 655303, Dallas, Texas 75265, 2014. URL: http://www.farnell.com/datasheets/2600445.pdf?_ga=2.79138452.104634221.1556379531-3243083.1556379531.

[15] Henkel AG. *LOCTITE HY 4090*. Post Office Box 655303, Dallas, Texas 75265, 2017. URL: http://www.farnell.com/datasheets/2600438.pdf?_ga=2.250397702.104634221.1556379531-3243083.1556379531.

[16] Hirst Magnetic Instruments Ltd. *GM07 & GM08 Gaussmeter*. 2019. URL: https://docs-emea.rs-online.com/webdocs/08dc/0900766b808dcae2.pdf.

[17] G. E. Karniadakis and Kwing-So Choi. “Mechanisms on Transverse Motions in Turbulent Wall Flows”. In: *Annual Review of Fluid Mechanics* 35.1 (Jan. 2003), pp. 45–62. DOI: `10.1146/annurev.fluid.35.101101.161213`.

[18] Keyence Corporation. *LK-H022 Sensor Head Spot Type, Laser Class 2*. Apr. 27, 2019. URL: `https://www.keyence.com/products/measure/laser-1d/lk-g5000/models/lk-h022/index.jsp`.

[19] Mike Klasco and Steve Tatarunis. “The Voice Coil (Part 1)”. In: *audioXpress magazine* (03/12 2012). URL: `https://circuitcellar.com/wp-content/uploads/2012/02/AX-march-Klasco.pdf`.

[20] S. Klumpp, M. Meinke, and W. Schröder. “Drag reduction by spanwise transversal surface waves”. In: *Journal of Turbulence* 11 (Jan. 2010), N22. DOI: `10.1080/14685248.2010.494606`.

[21] A. Latham and W. Bussing. *Slide-by sensing for long-stroke applications using allegro angle sensors*. Tech. rep. Allegro MicroSystems LLC, 2016. URL: `https://www.allegromicro.com/en/Design-Center/Technical-Documents/Hall-Effect-Sensor-IC-Publications/Slide-By-Sensing-for-Long-Stroke-applications-using-Allegro-Angle-Sensors.aspx`.

[22] W. Li et al. “Turbulent drag reduction by spanwise traveling ribbed surface waves”. In: *European Journal of Mechanics - B/Fluids* 53 (Sept. 2015), pp. 101–112. DOI: `10.1016/j.euromechflu.2015.03.009`.

[23] Wenfeng Li et al. “Parametric investigation of friction drag reduction in turbulent flow over a flexible wall undergoing spanwise transversal traveling waves”. In: *Experiments in Fluids* 59.6 (May 2018). DOI: `10.1007/s00348-018-2559-3`.

[24] Jan Lunze. *Regelungstechnik 2*. Springer Berlin Heidelberg, 2016. DOI: `10.1007/978-3-662-52676-7`.

[25] Muhammad bin Mansoor et al. “Coupled piezoelectric nonlinear transduction array for turbulence manipulation”. In: *2017 19th International Conference on Solid-State Sensors, Actuators and Microsystems (TRANSDUCERS)*. IEEE, June 2017. DOI: `10.1109/transducers.2017.7994473`.

[26] Marian Albers and Pascal S. Meysonnat and W. Schröder. “Drag reduction via transversal wave motions of structured surfaces”. In: *Int. Symp. Turbulence & Shear Flow Phenomena (TSFP-10)*. 2017. URL: http://www.tsfp-conference.org/proceedings/2017/2/244.pdf.

[27] Pascal S. Meysonnat, Marian Albers, and Wolfgang Schröder. “Drag reduction of spanwise transversal traveling surface waves with stepwise amplitude increase”. In: *PAMM* 17.1 (Dec. 2017), pp. 127–128. DOI: 10.1002/pamm.201710036.

[28] MISUMI Europa GmbH. *Ball Slide Guides*. 2019. URL: https://uk.misumi-ec.com/pdf/fa/2014/P1_0619-0620_F08_EN_001.pdf.

[29] Musikhaus Thomann e.K. *TSA 4-700, TSA 1400, TSA 2200, TSA 4000, TSA 4-300, TSA 4-1300 Endstufe Bedienungsanleitung*. 2014. URL: https://www.x-vision-dj.de/app/download/5816323195/The.tAmp+TSA4-700%3A1300.pdf.

[30] National Instruments Corporation. *Device Specifications NI 6251*. 2016. URL: http://www.ni.com/pdf/manuals/375213c.pdf.

[31] National Instruments Corporation. *NI 6070E/6071E Family Specifications*. 2005. URL: http://www.ni.com/pdf/manuals/370725c.pdf.

[32] Christoph Rausch. “Time-dependent electromagnetic and thermal finite element simulation of an actuator system for turbulence research”. MA thesis. Institute for Applied Physics, Heinrich-Heine University Düsseldorf, 2018.

[33] Friedhelm Richter. *The Physical Properties of Steels „The 100 Steels Programme“ Part I: Tables and Figures*. 2010. URL: https://www.tugraz.at/fileadmin/user_upload/Institute/IEP/Thermophysics_Group/Files/Staehle-Richter.pdf.

[34] Hellmar Rockel and Ulrich Konigorski. “Iterativ Lernende Regelungen (II): Robuste Regelung von Schwingungsprüfständen im Frequenzbereich (Robust Iterative Learning Control in the Frequency Domain for Test Stands)”. In: *at – Automatisierungstechnik* 55.4 (Jan. 2007). DOI: 10.1524/auto.2007.55.4.180.

[35] Hellmar Rockel and Ulrich Konigorski. "Iterativ Lernende Regelungen, Teil I: Ein parametrischer Rahmen (A General Framework for Parametric Iterative Learning Control)". In: *at – Automatisierungstechnik* 55.3 (Jan. 2007). DOI: `10.1524/auto.2007.55.3.119`.

[36] Dorothee Roggenkamp et al. "Experimental investigation of turbulent boundary layers over transversal moving surfaces". In: *CEAS Aeronautical Journal* 6.3 (Apr. 2015), pp. 471–484. DOI: `10.1007/s13272-015-0155-2`.

[37] Rohde & Schwarz GmbH. *R&S HMP Series Power Supplies User Manual*. 2018. URL: `https://scdn.rohde-schwarz.com/ur/pws/dl_downloads/dl_common_library/dl_manuals/gb_1/h/hmp_serie/HMPSeries_UserManual_en_02.pdf`.

[38] Stephan Russenschuck. *Field Computation for Accelerator Magnets*. Wiley VCH Verlag GmbH, Mar. 10, 2010. ISBN: 3527407693. URL: `https://www.ebook.de/de/product/9218745/stephan_russenschuck_field_computation_for_accelerator_magnets.html`.

[39] Wolfgang Schröder. *Fluidmechanik*. Verlagsgruppe Mainz, Apr. 6, 2018. 354 pp. ISBN: 3958862217. URL: `https://www.ebook.de/de/product/32924354/wolfgang_schroeder_fluidmechanik.html`.

[40] F. Seidler et al. "Iterative Learning Wave Control of a 20 Actuator System for External Flow Research". 2019 IEEE Conference on Control, Decision and Information Technologies (CoDIT). Aug. 2019. to be published.

[41] F. Seidler et al. "Sensors for waveform control in a Lorentz force based actuator system for turbulence research". In: *2017 IEEE SENSORS*. IEEE, Oct. 2017. DOI: `10.1109/icsens.2017.8234197`.

[42] P. Seshu. *Textbook of finite element analysis*. PHI Learning Pvt. Ltd., 2003. ISBN: 978-8120323155. URL: `http://soaneemrana.com/onewebmedia/TEXT%20BOOKOF%20FINITE%20ELEMENT%20ANALYSIS%20BY%20P.%20SESHU%20(1).pdf`.

[43] Gautam Sinha and S. S. Prabhu. "Analytical model for estimation of eddy current and power loss in conducting plate and its application". In: *Physical Review Special Topics - Accelerators and Beams* 14.6 (June 2011). DOI: `10.1103/physrevstab.14.062401`.

[44] Speedgoat GmbH. *Made for Simulink*. May 12, 2019. URL: https://www.speedgoat.com/speedgoat-solutions#MadeforSimulink.

[45] Stratasys Ltd. *Objet350 and Objet500 Connex3*. 2016. URL: https://www.stratasys.com/~/media/Main/Files/Machine_Spec_Sheets/PSS_PJ_Connex3.ashx.

[46] Yik R. Teo and Andrew J. Fleming. "A new repetitive control scheme based on non-causal FIR filters". In: *2014 American Control Conference*. IEEE, June 2014. DOI: 10.1109/acc.2014.6858916.

[47] Texas Instruments, Inc. *OPA2541 Datasheet*. One Technology Way, P.O. Box 9106, Norwood, MA 02062-9106, U.S.A., 2017. URL: http://www.ti.com/lit/ds/sbos157/sbos157.pdf.

[48] The MathWorks, Inc. *MATLAB and Simulink Real-Time Release 2015b*. Natick, Massachusetts, United States. 2015.

[49] Masanam Balakrishnan Bharat Vikas. "COMSOL Finite Element Simulation of an Electromechanical Actuator System for Turbulence Research". MA thesis. Department of Computational Mechanics, University of Duisburg-Essen, 2018.

[50] Vishay Semiconductor GmbH. *Transmissive Optical Sensor with Phototransistor Output*. 1999. URL: https://www.vishay.com/docs/83764/tcst1103.pdf.

[51] S. Volkel et al. "Smooth wavelength transition in a Lorentz force based actuator system for turbulence research". In: *2017 IEEE SENSORS*. IEEE, Oct. 2017. DOI: 10.1109/icsens.2017.8234195.

[52] Youqing Wang, Furong Gao, and Francis J. Doyle. "Survey on iterative learning control, repetitive control, and run-to-run control". In: *Journal of Process Control* 19.10 (Dec. 2009), pp. 1589–1600. DOI: 10.1016/j.jprocont.2009.09.006.

[53] Würth Elektronik GmbH. *Standard FR4 TG135 Datasheet*. 2019. URL: http://www.wedirekt.com/web/mandators/media/16_wedirekt/spezifikationen/leiterplatten_daten_downloads/FR4TG135_UK.pdf.

Band / Volume 510
Effect of electric field on the sintering of ceria
C. Cao (2020), xix, 143 pp
ISBN: 978-3-95806-497-3

Band / Volume 511
Techno-ökonomische Bewertung von Verfahren zur Herstellung von Kraftstoffen aus H_2 und CO_2
S. Schemme (2020), 360 pp
ISBN: 978-3-95806-499-7

Band / Volume 512
Enhanced crosshole GPR full-waveform inversion to improve aquifer characterization
Z. Zhou (2020), VIII, 136 pp
ISBN: 978-3-95806-500-0

Band / Volume 513
Time-Resolved Photoluminescence on Perovskite Absorber Materials for Photovoltaic Applications
F. Staub (2020), viii, 198 pp
ISBN: 978-3-95806-503-1

Band / Volume 514
Crystallisation of Oxidic Gasifier Slags
J. P. Schupsky (2020), III, 127, XXII pp
ISBN: 978-3-95806-506-2

Band / Volume 515
Modeling and validation of chemical vapor deposition for tungsten fiber reinforced tungsten
L. Raumann (2020), X, 98, XXXVIII pp
ISBN: 978-3-95806-507-9

Band / Volume 516
Zinc Oxide / Nanocrystalline Silicon Contacts for Silicon Heterojunction Solar Cells
H. Li (2020), VIII, 135 pp
ISBN: 978-3-95806-508-6

Band / Volume 517
Iron isotope fractionation in arable soil and graminaceous crops
Y. Xing (2020), X, 111 pp
ISBN: 978-3-95806-509-3

Schriften des Forschungszentrums Jülich
Reihe Energie & Umwelt / Energy & Environment

Band / Volume 518
Geophysics-based soil mapping for improved modelling of spatial variability in crop growth and yield
C. Brogi (2020), xxi, 127 pp
ISBN: 978-3-95806-510-9

Band / Volume 519
Measuring and modelling spatiotemporal changes in hydrological response after partial deforestation
I. Wiekenkamp (2020), xxxvii, 276 pp
ISBN: 978-3-95806-512-3

Band / Volume 520
Characterization of Root System Architectures from Field Root Sampling Methods
S. Morandage (2020), xxii, 157 pp
ISBN: 978-3-95806-511-6

Band / Volume 521
Generation Lulls from the Future Potential of Wind and Solar Energy in Europe
D. S. Ryberg (2020), xxvii, 398 pp
ISBN: 978-3-95806-513-0

Band / Volume 522
Towards a Generalized Framework for the Analysis of Solar Cell Performance based on the Principle of Detailed Balance
B. J. Blank (2020), iv, 142 pp
ISBN: 978-3-95806-514-7

Band / Volume 523
A Robust Design of a Renewable European Energy System Encompassing a Hydrogen Infrastructure
D. G. Çağlayan (2020), xxii, 312 pp
ISBN: 978-3-95806-516-1

Band / Volume 524
Control and Optimization of a Lorentz Force Based Actuator System for External Flow
M. F. Seidler (2020), xii, 136 pp
ISBN: 978-3-95806-518-5

Weitere ***Schriften des Verlags im Forschungszentrum Jülich*** unter
http://wwwzb1.fz-juelich.de/verlagextern1/index.asp

Energie & Umwelt / Energy & Environment
Band / Volume 524
ISBN 978-3-95806-518-5

Mitglied der Helmholtz-Gemeinschaft

JÜLICH
Forschungszentrum